# A *HERSCHEL*[*] AND APEX CENSUS OF THE REDDEST SOURCES IN ORION: SEARCHING FOR THE YOUNGEST PROTOSTARS[†]

Amelia M. Stutz[1], John J. Tobin[2,13], Thomas Stanke[3], S. Thomas Megeath[4], William J. Fischer[4], Thomas Robitaille[1], Thomas Henning[1], Babar Ali[5], James di Francesco[6,7], Elise Furlan[5,8], Lee Hartmann[9], Mayra Osorio[10], Thomas L. Wilson[11], Lori Allen[8], Oliver Krause[1], and P. Manoj[12]

[1] Max Planck Institute for Astronomy, Königstuhl 17, D-69117 Heidelberg, Germany; stutz@mpia.de
[2] National Radio Astronomy Observatory, Charlottesville, VA 22903, USA
[3] ESO, Karl-Schwarzschild-Strasse 2, D-85748 Garching bei München, Germany
[4] Department of Physics and Astronomy, University of Toledo, 2801 W. Bancroft Street, Toledo, OH 43606, USA
[5] NHSC/IPAC/Caltech, 770 S. Wilson Avenue, Pasadena, CA 91125, USA
[6] National Research Council of Canada, Herzberg Institute of Astrophysics, 5071 West Saanich Road, Victoria, BC V9E 2E7, Canada
[7] Department of Physics and Astronomy, University of Victoria, P.O. Box 3055, STN CSC, Victoria, BC V8W 3P6, Canada
[8] National Optical Astronomy Observatory, 950 North Cherry Avenue, Tucson, AZ 85719, USA
[9] Department of Astronomy, University of Michigan, 830 Dennison Building, 500 Church Street, Ann Arbor, MI 48109, USA
[10] Instituto de Astrofísica de Andalucía, CSIC, Camino Bajo de Huétor 50, E-18008 Granada, Spain
[11] Naval Research Laboratory, 4555 Overlook Avenue SW, Washington, DC 20375, USA
[12] Department of Physics and Astronomy, 500 Wilson Boulevard, University of Rochester, Rochester, NY 14627, USA

## ABSTRACT

We perform a census of the reddest, and potentially youngest, protostars in the Orion molecular clouds using data obtained with the PACS instrument on board the *Herschel Space Observatory* and the LABOCA and SABOCA instruments on APEX as part of the *Herschel* Orion Protostar Survey (HOPS). A total of 55 new protostar candidates are detected at 70 $\mu$m and 160 $\mu$m that are either too faint ($m_{24} > 7$ mag) to be reliably classified as protostars or undetected in the *Spitzer*/MIPS 24 $\mu$m band. We find that the 11 reddest protostar candidates with log $\lambda F_\lambda 70/\lambda F_\lambda 24 > 1.65$ are free of contamination and can thus be reliably explained as protostars. The remaining 44 sources have less extreme 70/24 colors, fainter 70 $\mu$m fluxes, and higher levels of contamination. Taking the previously known sample of *Spitzer* protostars and the new sample together, we find 18 sources that have log $\lambda F_\lambda 70/\lambda F_\lambda 24 > 1.65$; we name these sources "PACS Bright Red sources," or PBRs. Our analysis reveals that the PBR sample is composed of Class 0 like sources characterized by very red spectral energy distributions (SEDs; $T_{\rm bol} < 45$ K) and large values of sub-millimeter fluxes ($L_{\rm smm}/L_{\rm bol} > 0.6\%$). Modified blackbody fits to the SEDs provide lower limits to the envelope masses of 0.2–2 $M_\odot$ and luminosities of 0.7–10 $L_\odot$. Based on these properties, and a comparison of the SEDs with radiative transfer models of protostars, we conclude that the PBRs are most likely extreme Class 0 objects distinguished by higher than typical envelope densities and hence, high mass infall rates.

*Key words:* ISM: clouds – stars: formation – stars: low-mass – stars: protostars

*Online-only material:* color figures

## 1. INTRODUCTION

The onset of the star formation process is broadly characterized by a dense collapsing cloud envelope surrounding the nascent protostar. The dense cloud or protostellar envelope is opaque to radiation shortward of about ~10 $\mu$m and most of the radiation from these sources is reprocessed and emitted in the far-infrared (FIR). Furthermore, bipolar outflows from the protostar and disk carve out envelope cavities that enable a fraction of the protostellar luminosity to escape in the form of scattered light emission, predominantly at wavelengths shortward of ~10 $\mu$m.

The earliest phase of protostellar evolution, the Class 0 phase (André et al. 1993), is thought to be short compared to the Class I phase (Lada 1987), with combined Class 0 and Class I lifetimes of ~0.5 Myr (Evans et al. 2009); these estimates assume a constant star formation rate and a typical age for Class II objects (pre-main-sequence stars with disks) of 2 Myr. At the onset of collapse and immediately before the Class 0 phase, protostars may go through a brief first hydrostatic core (FHSC) phase where the forming protostellar object becomes opaque to its own radiation for the first time (Larson 1969). The FHSC is expected to be very low luminosity and deeply embedded. A population of very low luminosity protostars (VeLLOs) was also recently identified by *Spitzer* (e.g., Dunham et al. 2008; Bourke et al. 2006), defined to have model-estimated internal source luminosities of less than 0.1 $L_\odot$. VeLLOs, however, appear more evolved than FHSCs with features consistent with Class 0 and I protostars. Furthermore, while several FHSC candidates have been identified recently (e.g., see Enoch et al. 2010; Chen et al. 2010; Pineda et al. 2011; Pezzuto et al. 2012), it has proven observationally difficult to distinguish such sources from the young Class 0 protostellar phase. It is therefore currently difficult to identify the very earliest phases of the formation of a protostar.

[13] Hubble Fellow.

Before the launch of *Spitzer* and the advent of extremely sensitive mid-infrared surveys, conventional wisdom held that a Class 0 protostar should not be detectable at wavelengths shortward of 10 $\mu$m due to the envelope opacity (Williams & Cieza 2011). Outflows, however, can carve out cavities in the protostellar envelopes at a very early age and are expected to widen with evolution (Arce & Sargent 2006). Indeed, recent simulations have shown that even the extremely young FHSC sources may be capable of driving outflows (Commerçon et al. 2012; Price et al. 2012). Regardless of evolutionary state, the outflow cavities enable near- to mid-infrared light from the protostar and disk to escape and scatter off dust grains in the cavity or on the cavity walls. This phenomenon has been well known for Class I sources (Kenyon et al. 1993; Padgett et al. 1999), but Class 0 protostars were only well detected in the mid-infrared with *Spitzer* (Noriega-Crespo et al. 2004; Jørgensen et al. 2007; Stutz et al. 2008). The scattered light from Class 0 protostars is often brightest at wavelengths ∼3.6 $\mu$m or 4.5 $\mu$m due to the dense envelope obscuration at shorter wavelengths (e.g., Whitney et al. 2003b; Tobin et al. 2007).

The combination of results from recent space- and ground-based surveys have resulted in well-sampled spectral energy distributions (SEDs) from the near-infrared to the (sub-)millimeter for large samples of protostellar objects (e.g., Hatchell et al. 2007; Enoch et al. 2009; Launhardt et al. 2010, 2013; Fischer et al. 2010). These SEDs are dominated by scattered light between ∼1 $\mu$m and 10 $\mu$m, optically thick thermal dust emission from ∼10 to ∼160 $\mu$m, and optically thin dust emission at wavelengths longward of ∼160 $\mu$m. Radiative transfer models of protostellar collapse have become increasingly important to interpret these data since these can account for the varying temperature and density profiles in the envelopes surrounding the protostar (e.g., Whitney et al. 2003a, 2003b).

The large number of free model parameters—such as the combination of outflow cavities, rotationally flattened envelopes, (Ulrich 1976; Cassen & Moosman 1981; Terebey et al. 1984), and varying viewing angles—can however make the best-fit SED model parameters highly degenerate (e.g., Whitney et al. 2003b). For example, sources viewed at nearly edge-on orientations can be substantially more obscured than sources at the same evolutionary state viewed from a less extreme vantage point. Thus, standard diagnostics such as bolometric temperature or mid-infrared spectral index can yield vastly different results depending on the source inclination (e.g., Dunham et al. 2010). Radiative transfer models can help break some of these degeneracies but ambiguities can remain as to whether a source has a very dense envelope or if it is simply viewed edge-on.

While much has been learned about the Class 0 phase from observations and modeling, there are relatively few Class 0 objects present in nearby star-forming clouds and globules (Evans et al. 2009) compared to the numbers of Class I and Class II sources. One of the principal goals of recent star formation surveys has been to understand the evolution of protostellar sources. Young & Evans (2005) generated models for the smooth luminosity evolution of protostellar objects that will become 0.3 $M_\odot$, 1 $M_\odot$, and 3 $M_\odot$ stars. These models, however, overpredict the luminosities of most protostars located in nearby star-forming regions, a fact that is taken as evidence for episodic accretion (Kenyon & Hartmann 1990; Evans et al. 2009; Dunham et al. 2010). However, Offner & McKee (2011) show that the observed luminosity functions of protostars can be explained through a dependence of the mass accretion rate on the instantaneous and final mass of the protostar. The low

resolutions and sensitivities of previous FIR instrumentation have made the detection of protostars in more distant and richer star-forming regions difficult and subject to substantial confusion. Thus, studies of protostellar evolution have been limited to combining all known Class 0 protostars from the nearby regions into a single analysis (e.g., Myers et al. 1998; Evans et al. 2009) to achieve a more robust sample size.

The advent of the *Herschel Space Observatory* (Pilbratt et al. 2010) has tremendously improved resolution and sensitivity to FIR radiation, where protostars emit the bulk of their energy. These improvements enable the study of protostellar populations to be extended to more distant, richer regions of star formation that have more statistically significant samples of protostars in the Class 0 and I phases (e.g., Ragan et al. 2012). The *Herschel* Orion Protostar Survey (HOPS) is a *Herschel* Open Time Key Programme (OTKP; e.g., Stanke et al. 2010; Fischer et al. 2010; Ali et al. 2010; Manoj et al. 2013) targeting ∼300 of the *Spitzer*-identified Orion protostars with PACS (Poglitsch et al. 2010) 70 $\mu$m and 160 $\mu$m photometry and PACS spectroscopy (53–200 $\mu$m; Manoj et al. 2013) for a subset of 30 protostars. Orion is the richest star-forming region within 500 pc of the Sun (Megeath et al. 2012), at a distance of ∼420 pc (average value; Menten et al. 2007; Hirota et al. 2007; Sandstrom et al. 2007). The large sample of protostars in Orion enables studies of protostellar evolution to be carried out for a single star-forming complex where all protostars lie at nearly the same distance with a statistically significant sample, comparable to or larger than all the nearby regions combined. The large sample may also enable short timescale phenomena (e.g., Fischer et al. 2012) to be detected, such as brief periods of high envelope infall rate in the earliest phases of star formation. Even with the increased numbers of protostars in Orion, however, it is unclear if we would expect to detect FHSCs given the faintness of these sources and short lifetimes of less than 10 kyr (Commerçon et al. 2012).

The PACS imaging of the HOPS program has the potential to identify protostars that were not detected by *Spitzer* due to a combination of opacity of the envelope and/or confusion with nearby sources. Indeed, the PACS 70 $\mu$m band of *Herschel* is ideal for detecting such protostars, with the highest angular resolution, limiting the blending of sources. Also, the lower opacity relative to MIPS 24 $\mu$m allows the reprocessed warm inner envelope radiation to escape. Finally, and most importantly, a 70 $\mu$m point source is strong evidence for an embedded protostar because external heating cannot raise temperatures high enough to emit at this wavelength. Thus, some cores in sub-millimeter surveys that were previously identified as starless may in reality be protostellar.

Using *Herschel*, we have serendipitously identified a sample of 70 $\mu$m point sources that were not identified at shorter wavelengths in the previous *Spitzer* protostar sample (Megeath et al. 2012). Furthermore, we have identified a subset of these that have the reddest 70 $\mu$m to 24 $\mu$m colors of all protostars in the combined Orion sample. These sources may have the densest envelopes and are possibly the youngest detected Orion protostars and we name them "PACS Bright Red sources" or PBRs.

We will describe the methodology of identifying these sources and classify them as either being protostellar, extragalactic contamination, or spurious detections coincident with extended emission. We will discuss the observations and data reduction in Section 2, the source finding and classification methods in Section 3, the observed properties of the new sources in

Section 4, the PBRs in Section 5, the comparison of the cold PBRs to models in Section 6, some relevant model degeneracies in Section 7, and, finally, our results in Section 8. Throughout this work, all positions are given in the J2000 system.

## 2. OBSERVATIONS, DATA REDUCTION, AND PHOTOMETRY

In this work, we present *Herschel* scan-map observations of a subset of the HOPS fields containing candidate protostars. In addition, we present a subset of our APEX LABOCA and SABOCA observations of these fields. A summary of the HOPS *Herschel* PACS survey observations is presented in Tables 1 and 2. Here we discuss the observations, data processing, and photometry extraction.

### 2.1. Herschel PACS

The PACS data were acquired simultaneously at 70 $\mu$m and 160 $\mu$m over $5' \times 5'$ or $8' \times 8'$ field sizes. The field sizes and centers were chosen to maximize observing efficiency by allowing each field to include as many of the target *Spitzer*-selected protostars (Megeath et al. 2012) as possible while minimizing redundant coverage. The observations were acquired at medium scan speed ($20'' \ s^{-1}$), and are composed of two orthogonal scans with homogeneous coverage.

The PACS data were reduced using the Herschel Interactive Processing Environment (HIPE) version 8.0 build 248 and version 9.0 build 215. We used a custom-built pipeline to process data from their raw form (the so-called Level 0 data) to fully calibrated time lines (Level 1) just prior to the map-making step. Our pipeline uses the same processing steps as described by Poglitsch et al. (2010) but also include the following additions and modifications. First, we used a spatial redundancy-based algorithm to identify and mask cosmic-ray hits. Second, we mitigated instrument cross-talk artifacts by masking (flagging as unusable) detector array columns affected by cross-talk noise. This technique is effective but at the expense of loss of signal from the affected detector array columns. Third, we used the "FM6" version of the instrument responsivity, which has a direct bearing on the absolute calibration of the final mosaics.

The Level 1 data were processed with "Scanamorphos" (Roussel 2012) version 14.0. The final maps were produced using the *galactic* option and included the turnaround (non-zero acceleration) data. The final map pixel scales used in this work are $1''.0 \ pixel^{-1}$ at 70 $\mu$m and $2''.0 \ pixel^{-1}$ at 160 $\mu$m.

The photometry was performed in the following fashion. We first derived customized aperture corrections to the 70 $\mu$m and 160 $\mu$m data using the Herschel Science Center (HSC) provided observations of Vesta (to be discussed in more detail in W. J. Fischer et al., in preparation). At 70 $\mu$m, we used radii of sizes $9''.6$, $9''.6$, and $19''.2$, for the aperture and sky annuli, respectively. For these parameters we derived an aperture correction of 0.7331, where the measured flux in the aperture is divided by this correction to obtain a total point-source flux. At 160 $\mu$m, we used aperture radii of $12''.8$, $12''.8$, and $25''.6$, for the aperture and sky annuli, respectively. Similarly, we derived an aperture correction of 0.6602. The encircled energy fractions provided by the `photApertureCorrectionPointSource` task in HIPE do not account for the effect of applying an inner sky annulus that is close to the size of the source aperture and small compare to the point-spread function (PSF). Our corrections therefore account for 3%–4% of the source flux that is removed. Furthermore, our adopted aperture sizes are smaller than the

PACS instrument team recommendation but were chosen to minimize contribution from nebulosity (extended, non-point-like emission) often surrounding the protostars in Orion. Given the complex structure in the images and at times crowded fields, our aperture photometry may suffer from blending and contamination. The photometric errors include a 10% systematic error floor added in quadrature to the standard photometric uncertainties. These errors represent systematic uncertainties in our photometry and aperture correction, as well as the overall calibration uncertainty of PACS. We note that the reported HSC point-source calibration uncertainties for PACS are $\sim$3% at 70 $\mu$m and $\sim$5% at 160 $\mu$m, and were derived from isolated photometric standards. Therefore, our final uncertainties are conservative.

We include the 100 $\mu$m Gould Belt Survey (GBS; e.g., André et al. 2010; Könyves et al. 2010; Men'shchikov et al. 2010, see also N. Schneider et al., in preparation, for Orion B, and A. Roy et al., in preparation, and D. Polychroni et al., in preparation, for Orion A) data of Orion in this work for the PBRs analysis. Given the sparsely covered SEDs of our sources, these data provide important information regarding the shape of the thermal SED of cold envelope sources. These data were acquired using medium scan speed ($20'' \ s^{-1}$) and cover an area much larger than the HOPS fields. These data were processed in a similar way to the HOPS processing described above. Following the above 70 $\mu$m and 160 $\mu$m analysis, we used aperture radii of sizes $9''.6$, $9''.6$, and $19''.2$ for the aperture and sky annuli, respectively. For these parameters, we derived an aperture correction of 0.6944. As with the 70 $\mu$m and 160 $\mu$m data, we also assume a conservative 10% systematic error floor.

### 2.2. APEX SABOCA and LABOCA

We obtained sub-millimeter (smm) continuum maps using the LABOCA and SABOCA bolometer arrays on the APEX telescope. LABOCA (Siringo et al. 2009) is a $\sim$250 bolometer array operating at 870 $\mu$m, with a spatial resolution of $\sim$19″ at FWHM. We used a combination of spiral and straight on-the-fly scans to recover extended emission. Data reduction was done with the BOA software (P. Schuller et al., in preparation) following standard procedures, including iterative source modeling. SABOCA (Siringo et al. 2010) is a 37 bolometer array operating at 350 $\mu$m, with a resolution of $\sim$7″.3 FWHM. The observing and data reduction procedures were similar to those used for LABOCA. For both cameras, observations were carried out between 2009 November and 2012 June, and are still ongoing to complete our Submillimeter Orion Survey. Conditions were generally fair over the course of our observing campaign. The observations will be summarized in more detail by T. Stanke et al. (2013, in preparation).

The beam sizes of the final reduced maps are $7''.34$ and $19''.0$ FWHM for the SABOCA and LABOCA observations, respectively. The photometry was extracted in the same way for both wavelengths. When possible, if there was a strong source detection, we re-centered using the 70 $\mu$m catalog source coordinates. Given the contributions of flux due to surrounding cold material, such as filaments and other extended envelope structure, it is likely that a single photometric measure can suffer from large systematic effects. We have measured source fluxes in three ways.

1. We measured the source peak flux per beam.
2. We measured source flux over an aperture with radius equal to the FWHM at the corresponding wavelength

**Table 1**
Summary of HOPS *Herschel* PACS L1641 Observations

| HOPS Group Name | R.A.[a] (h:m:s) | Decl.[a] (°:′;″) | Field | AOR ID | OD | Map Size (′ × ′) |
|---|---|---|---|---|---|---|
| 54 | 5:42:38.570 | −8:50:18.67 | L1641 | 1342218796(7) | 704 | 8 × 8 |
| 53 | 5:43:06.770 | −8:46:09.56 | L1641 | 1342218735(6) | 703 | 8 × 8 |
| 60 | 5:41:29.690 | −8:41:28.59 | L1641 | 1342215359(60) | 662 | 8 × 8 |
| 55 | 5:42:50.490 | −8:40:54.73 | L1641 | 1342218798(9) | 704 | 8 × 8 |
| 56 | 5:42:52.750 | −8:37:20.98 | L1641 | 1342205256(7) | 502 | 8 × 8 |
| 117 | 5:41:33.250 | −8:36:41.62 | L1641 | 1342218790(1) | 704 | 8 × 8 |
| 59 | 5:42:55.540 | −8:32:48.26 | L1641 | 1342218794(5) | 704 | 8 × 8 |
| 58 | 5:43:09.580 | −8:29:27.13 | L1641 | 1342218788(9) | 704 | 8 × 8 |
| 61 | 5:42:47.760 | −8:16:50.72 | L1641 | 1342205254(5) | 502 | 8 × 8 |
| 67 | 5:40:20.130 | −8:14:05.78 | L1641 | 1342227078(9) | 831 | 8 × 8 |
| 119 | 5:40:47.820 | −8:10:28.38 | L1641 | 1342206322(3) | 516 | 8 × 8 |
| 62 | 5:42:47.370 | −8:10:08.76 | L1641 | 1342218792(3) | 704 | 8 × 8 |
| 63 | 5:41:35.440 | −8:08:22.49 | L1641 | 1342218800(1) | 704 | 8 × 8 |
| 66 | 5:40:54.500 | −8:06:08.98 | L1641 | 1342215361(2) | 662 | 8 × 8 |
| 118 | 5:41:27.790 | −8:04:03.70 | L1641 | 1342205250(1) | 502 | 8 × 8 |
| 78 | 5:38:51.480 | −8:01:27.44 | L1641 | 1342228169(70) | 844 | 5 × 5 |
| 64 | 5:41:49.950 | −8:01:26.51 | L1641 | 1342205252(3) | 502 | 5 × 5 |
| 69 | 5:40:38.330 | −8:00:36.00 | L1641 | 1342227080(1) | 831 | 5 × 5 |
| 65 | 5:41:24.880 | −8:00:02.34 | L1641 | 1342215591(2) | 663 | 8 × 8 |
| 72 | 5:40:20.710 | −7:56:01.36 | L1641 | 1342218733(4) | 703 | 8 × 8 |
| 70 | 5:40:40.530 | −7:54:39.82 | L1641 | 1342228167(8) | 844 | 5 × 5 |
| 121 | 5:41:23.440 | −7:54:39.26 | L1641 | 1342205248(9) | 502 | 8 × 8 |
| 68 | 5:41:19.660 | −7:50:41.03 | L1641 | 1342227848(9) | 842 | 5 × 5 |
| 74 | 5:40:17.690 | −7:49:29.88 | L1641 | 1342218731(2) | 703 | 8 × 8 |
| 71 | 5:40:40.150 | −7:49:18.71 | L1641 | 1342228163(4) | 844 | 8 × 8 |
| 320 | 5:40:58.890 | −7:48:02.05 | L1641 | 1342228165(6) | 844 | 5 × 5 |
| 73 | 5:40:42.910 | −7:45:01.91 | L1641 | 1342228425(6) | 847 | 5 × 5 |
| 75 | 5:40:24.620 | −7:43:08.26 | L1641 | 1342227082(3) | 831 | 5 × 5 |
| 76 | 5:40:26.090 | −7:37:32.02 | L1641 | 1342205246(7) | 502 | 5 × 5 |
| 79 | 5:39:57.200 | −7:30:19.89 | L1641 | 1342205244(5) | 502 | 8 × 8 |
| 77 | 5:40:44.670 | −7:29:54.46 | L1641 | 1342228427(8) | 847 | 5 × 5 |
| 123 | 5:40:08.780 | −7:27:27.68 | L1641 | 1342228161(2) | 844 | 5 × 5 |
| 26 | 5:39:24.640 | −7:26:13.81 | L1641 | 1342218729(30) | 703 | 8 × 8 |
| 25 | 5:39:56.200 | −7:24:53.71 | L1641 | 1342215589(90) | 663 | 8 × 8 |
| 313 | 5:39:33.300 | −7:22:57.36 | L1641 | 1342227084(5) | 831 | 5 × 5 |
| 28 | 5:38:56.470 | −7:20:44.32 | L1641 | 1342227086(7) | 831 | 8 × 8 |
| 30 | 5:38:44.050 | −7:11:49.89 | L1641 | 1342204254(5) | 484 | 8 × 8 |
| 29 | 5:39:06.710 | −7:11:12.80 | L1641 | 1342204252(3) | 484 | 8 × 8 |
| 32 | 5:38:01.100 | −7:07:37.01 | L1641 | 1342227045(6) | 830 | 8 × 8 |
| 312 | 5:38:46.540 | −7:05:37.46 | L1641 | 1342205242(3) | 502 | 5 × 5 |
| 31 | 5:38:44.870 | −7:00:37.03 | L1641 | 1342204256(7) | 484 | 8 × 8 |
| 33 | 5:38:20.090 | −6:59:04.85 | L1641 | 1342228171(2) | 844 | 5 × 5 |
| 35 | 5:37:24.460 | −6:58:32.77 | L1641 | 1342227314(5) | 833 | 5 × 5 |
| 34 | 5:37:59.990 | −6:57:27.50 | L1641 | 1342205240(1) | 502 | 8 × 8 |
| 101 | 5:37:17.090 | −6:49:49.33 | L1641 | 1342227312(3) | 833 | 5 × 5 |
| 36 | 5:37:52.390 | −6:47:18.67 | L1641 | 1342227088(9) | 831 | 8 × 8 |
| 38 | 5:36:22.050 | −6:45:41.23 | L1641 | 1342205238(9) | 502 | 8 × 8 |
| 40 | 5:36:26.650 | −6:38:27.74 | L1641 | 1342227094(5) | 831 | 8 × 8 |
| 37 | 5:37:17.280 | −6:36:18.18 | L1641 | 1342227090(1) | 831 | 8 × 8 |
| 43 | 5:35:50.020 | −6:34:53.40 | L1641 | 1342227310(1) | 833 | 5 × 5 |
| 50 | 5:34:15.880 | −6:34:32.70 | L1641 | 1342217748(9) | 686 | 8 × 8 |
| 39 | 5:36:41.330 | −6:34:00.08 | L1641 | 1342227092(3) | 831 | 5 × 5 |
| 41 | 5:36:19.440 | −6:29:06.79 | L1641 | 1342227316(7) | 833 | 5 × 5 |
| 45 | 5:35:34.120 | −6:26:41.70 | L1641 | 1342215593(4) | 663 | 8 × 8 |
| 311 | 5:34:39.860 | −6:25:14.16 | L1641 | 1342203649(50) | 470 | 5 × 5 |
| 42 | 5:36:22.460 | −6:23:39.14 | L1641 | 1342205236(7) | 502 | 8 × 8 |
| 44 | 5:36:36.980 | −6:14:57.98 | L1641 | 1342204258(9) | 484 | 5 × 5 |
| 51 | 5:35:22.180 | −6:13:06.24 | L1641 | 1342227318(9) | 833 | 5 × 5 |
| 47 | 5:36:17.260 | −6:11:11.00 | L1641 | 1342227324(5) | 833 | 5 × 5 |
| 49 | 5:35:52.000 | −6:10:01.85 | L1641 | 1342227322(3) | 833 | 5 × 5 |
| 52 | 5:35:33.210 | −6:06:09.65 | L1641 | 1342227320(1) | 833 | 5 × 5 |
| 48 | 5:36:31.360 | −6:01:16.81 | L1641 | 1342217444(5) | 685 | 8 × 8 |
| 5 | 5:35:07.960 | −5:56:56.40 | L1641 | 1342204248(9) | 484 | 8 × 8 |
| 6 | 5:35:24.560 | −5:55:33.42 | L1641 | 1342227328(9) | 833 | 5 × 5 |

**Table 1**
(Continued)

| HOPS Group Name | R.A.[a] (h:m:s) | Decl.[a] (°:′:″) | Field | AOR ID | OD | Map Size (′ × ′) |
|---|---|---|---|---|---|---|
| 7 | 5:36:19.020 | −5:55:25.46 | L1641 | 1342227326(7) | 833 | 5 × 5 |
| 8 | 5:35:04.400 | −5:51:00.76 | L1641 | 1342217446(7) | 685 | 8 × 8 |
| 9 | 5:33:30.710 | −5:50:41.03 | L1641 | 1342217750(1) | 686 | 8 × 8 |
| 10 | 5:36:10.100 | −5:50:08.34 | L1641 | 1342227096(7) | 831 | 5 × 5 |
| 12 | 5:34:46.830 | −5:42:28.72 | L1641 | 1342204246(7) | 484 | 8 × 8 |
| 13 | 5:35:17.340 | −5:42:14.51 | L1641 | 1342227098(9) | 831 | 5 × 5 |
| 14 | 5:34:30.440 | −5:37:47.44 | L1641 | 1342204244(5) | 484 | 8 × 8 |

**Note.** [a] Field center coordinates.

**Table 2**
Summary of HOPS *Herschel* PACS ONC, NGC 2024, NGC 2068, and L1622 Observations

| HOPS Group Name | R.A.[a] (h:m:s) | Decl.[a] (°:′:″) | Region | AOR ID | OD | Map Size (′ × ′) |
|---|---|---|---|---|---|---|
| 15 | 5:35:06.620 | −5:35:05.68 | ONC | 1342205234(5) | 502 | 8 × 8 |
| 308 | 5:33:45.870 | −5:32:58.09 | ONC | 1342204433(4) | 487 | 5 × 5 |
| 16 | 5:34:43.990 | −5:32:11.21 | ONC | 1342217448(9) | 685 | 8 × 8 |
| 17 | 5:35:16.320 | −5:29:32.60 | ONC | 1342217450(1) | 685 | 8 × 8 |
| 18 | 5:33:55.730 | −5:22:39.97 | ONC | 1342217752(3) | 686 | 8 × 8 |
| 200 | 5:35:19.270 | −5:14:46.49 | ONC | 1342205232(3) | 502 | 8 × 8 |
| 130 | 5:35:24.710 | −5:09:06.02 | ONC | 1342205228(9) | 502 | 8 × 8 |
| 135 | 5:35:26.280 | −5:06:35.24 | ONC | 1342205226(7) | 502 | 8 × 8 |
| 19 | 5:35:23.300 | −5:00:35.73 | ONC | 1342204250(1) | 484 | 8 × 8 |
| 20 | 5:35:13.770 | −4:54:57.33 | ONC | 1342217758(9) | 686 | 8 × 8 |
| 21 | 5:34:32.340 | −4:53:54.26 | ONC | 1342217754(5) | 686 | 8 × 8 |
| 306 | 5:35:32.280 | −4:46:48.47 | ONC | 1342191970(1) | 300 | 5 × 5 |
| 24 | 5:35:23.340 | −4:40:10.45 | ONC | 1342217756(7) | 686 | 8 × 8 |
| 80 | 5:40:51.710 | −2:26:48.62 | NGC 2024 | 1342226729(30) | 826 | 5 × 5 |
| 81 | 5:41:28.940 | −2:23:19.36 | NGC 2024 | 1342226733(4) | 826 | 5 × 5 |
| 82 | 5:41:23.740 | −2:16:51.10 | NGC 2024 | 1342228913(4) | 858 | 8 × 8 |
| 83 | 5:41:42.180 | −2:16:26.20 | NGC 2024 | 1342227049(50) | 830 | 8 × 8 |
| 85 | 5:42:02.620 | −2:07:45.70 | NGC 2024 | 1342226735(6) | 826 | 5 × 5 |
| 86 | 5:41:43.560 | −1:53:28.42 | NGC 2024 | 1342227047(8) | 830 | 8 × 8 |
| 89 | 5:42:27.680 | −1:20:01.00 | NGC 2024 | 1342205220(1) | 502 | 5 × 5 |
| 90 | 5:43:04.370 | −1:16:11.60 | NGC 2024 | 1342228376(7) | 849 | 8 × 8 |
| 91 | 5:46:06.690 | −0:13:05.15 | NGC 2068 | 1342205218(9) | 502 | 8 × 8 |
| 92 | 5:46:14.210 | −0:05:26.84 | NGC 2068 | 1342205216(7) | 502 | 5 × 5 |
| 93 | 5:46:40.830 | +0:00:30.52 | NGC 2068 | 1342215363(4) | 662 | 8 × 8 |
| 94 | 5:46:39.580 | +0:04:16.61 | NGC 2068 | 1342228365(6) | 848 | 5 × 5 |
| 302 | 5:46:28.320 | +0:19:49.40 | NGC 2068 | 1342228374(5) | 849 | 5 × 5 |
| 303 | 5:47:24.810 | +0:20:59.68 | NGC 2068 | 1342227966(7) | 843 | 8 × 8 |
| 96 | 5:47:08.970 | +0:21:52.86 | NGC 2068 | 1342215587(8) | 663 | 8 × 8 |
| 128 | 5:46:56.220 | +0:23:42.41 | NGC 2068 | 1342218727(8) | 703 | 8 × 8 |
| 301 | 5:45:53.590 | +0:25:27.30 | NGC 2068 | 1342216450(1) | 675 | 5 × 5 |
| 97 | 5:47:58.060 | +0:35:30.12 | NGC 2068 | 1342227969(70) | 843 | 8 × 8 |
| 98 | 5:47:31.850 | +0:38:05.77 | NGC 2068 | 1342227971(2) | 843 | 8 × 8 |
| 300 | 5:47:42.990 | +0:40:57.50 | NGC 2068 | 1342205214(5) | 502 | 5 × 5 |
| 0 | 5:54:15.240 | +1:43:15.59 | L1622 | 1342215365(6) | 662 | 8 × 8 |
| 1 | 5:54:55.370 | +1:45:03.08 | L1622 | 1342218780(1) | 704 | 8 × 8 |
| 3 | 5:54:23.540 | +1:49:17.78 | L1622 | 1342218703(4) | 702 | 8 × 8 |
| 4 | 5:54:36.260 | +1:53:54.00 | L1622 | 1342218778(9) | 704 | 8 × 8 |

**Notes.** The ONC field contains the extended Orion Nebula region, the NGC 1977 region, and OMC2/3; the NGC 2024 field contains the NGC 2024 H II region and the NGC 2023 reflection nebula. The NGC 2068 field includes the NGC 2068 and NGC 2071 reflection nebulae as well as LBS23 region.
[a] Field center coordinates.

($r = 7.''34$ and $19.''0$ at 350 and 870 $\mu$m, respectively), using a sky annulus with inner and outer radii equal to $[1.5, 2.0] \times$ FWHM, corresponding to $11.''0$ and $14.''7$ at 350 $\mu$m, and $28.''5$ and $38.''0$ at 870 $\mu$m.

3. We measured the flux over the same aperture size as the previous method without any sky subtraction. In the case where a source was not strongly detected and we were not able to re-center, the 70 $\mu$m catalog source

coordinates were used, along with method 3, and the photometric point was flagged as an upper limit. By re-centering whenever possible, we accounted for possible pointing offsets between data sets, which can be significant. The calibration error dominated the error budget for well-detected sources; we therefore adopted a flux error equal to 20% and 40% of the measured flux for LABOCA and SABOCA, respectively. The photometric fluxes are presented in Table 5.

### 2.3. Spitzer IRAC and MIPS

The IRAC and MIPS imaging and photometry presented here are taken from the 9 deg$^2$ survey of the Orion A and B cloud obtained during the cryogenic Spitzer mission. The data analysis, extraction of the IRAC 3.6 $\mu$m, 4.5 $\mu$m, 5.8 $\mu$m, and 8 $\mu$m and MIPS 24 $\mu$m photometry, and the compilation of a point-source catalog containing the combined Two Micron All Sky Survey (2MASS), IRAC, and MIPS photometry are described in Megeath et al. (2012); see also Kryukova et al. (2012) for a detailed description of the MIPS 24 $\mu$m photometry. In total, 298,405 point sources were detected in at least one of the Spitzer bands, and 8021 sources were detected at 24 $\mu$m with uncertainties $\leqslant 0.25$ mag. The Spitzer images used in this work are taken from the mosaics generated from the Orion Survey data using Cluster Grinder for the IRAC data (Gutermuth et al. 2009) and the MIPS instrument team's Data Analysis Tool for the 24 $\mu$m data (Gordon et al. 2005). The MIPS data are saturated toward the Orion Nebula and parts of the NGC 2024 region; we exclude these saturated regions from our analysis.

The identification of protostars with the Spitzer data was based primarily on the presence of a flat or rising SED between 4.5 $\mu$m and 24 $\mu$m (Kryukova et al. 2012; Megeath et al. 2012). In addition, Megeath et al. identified objects which have point-source detections only at 24 $\mu$m but which also showed other indicators of protostellar nature such as the presence of jets in the IRAC bands. To minimize contamination from galaxies, the Spitzer-identified protostars were required to have 24 $\mu$m magnitudes brighter than 7th magnitude; fainter than 7 mag, the number of background galaxies begins to dominate over the number of embedded sources (Kryukova et al. 2012). Given the imposed 24 $\mu$m magnitude threshold, the faintest and reddest protostars may not be included in the Spitzer sample. In total, the Megeath et al. (2012) catalog contains 488 protostars. Of these, 428 are classified as bona fide protostars, 50 are faint candidate protostars, and 10 are red candidate protostars. The faint candidate protostars are sources with 24 $\mu$m magnitudes higher than 7.0. The red protostars are sources that are only detected as a point source at 24 $\mu$m and are thus not classifiable. Due to their location within high extinction regions and/or association with jets or compact scattered light nebulae in the IRAC bands, they have been included in the catalog. (Indeed, this last category was added to the Megeath et al. catalog after the Herschel data revealed that a relatively large number of such sources would likely be confirmed as protostars.) In addition, the Megeath et al. catalog identified 2992 objects as pre-main-sequence stars with disks. In what follows, we use the protostar catalog of 488 Spitzer sources to catalog previously identified sources in the HOPS images.

In contrast to the full Megeath et al. catalog, the HOPS protostar sample is composed of protostars specifically targeted by the HOPS program. The majority of the HOPS sample consists of Spitzer-identified protostars with 24 $\mu$m detections; hence, protostars in regions that are saturated in the 24 $\mu$m

images of Orion, namely the brightest regions of the Orion Nebula and NGC 2024, are not included. These protostars were also required to have a predicted 70 $\mu$m flux >20 mJy as extrapolated from their 3 $\mu$m to 24 $\mu$m SEDs. In addition, protostar candidates with only 24 $\mu$m detections were included if there was independent information of their protostellar nature. The HOPS sample represents the best pre-Herschel catalog of protostars that were expected to be detected with Herschel/PACS and were not found in bright nebulous regions. There are ∼300 protostars in the HOPS catalog which have been detected at 70 $\mu$m and ∼250 protostars detected at 160 $\mu$m. The uncertainty in the absolute number of protostars is due to the ongoing process of eliminating contamination from the sample.

### 3. IDENTIFICATION OF NEW CANDIDATE HERSCHEL PROTOSTARS

To find protostars which were not reliably identified with Spitzer, we must first isolate a sample of sources that are detected in the PACS 70 $\mu$m band but are either fainter than 7.0 mag or undetected in MIPS 24 $\mu$m waveband. To identify such sources in each HOPS field, we first generate a 70 $\mu$m source catalog using the PhotVis tool (Gutermuth et al. 2008). The PhotVis tool uses a sunken Gaussian filtering to extract sources that are of order the size of the Gaussian FWHM, an input parameter. We choose this parameter to be the size of the 70 $\mu$m PSF FWHM, or 5″. PhotVis also requires a signal-to-noise ratio threshold as input; we adopt a low value of 7 to balance the recovery of as many candidate sources as possible while still rejecting noise spikes.

Furthermore, we must reject unreliable sources near the edges of maps where the lower coverage causes elevated noise levels. The Scanamorphos scan-map image cubes include a weight map for each field. Within Scanamorphos, the weight map is computed over the same projection as the sky map, and is defined as 1 over the variance in the white noise (Roussel 2012). Each weight map is then normalized by the average map value (Roussel 2012). We find that for the HOPS data set, weight map values of ∼20 are confined to the outer higher noise edges of our scan maps. We therefore use the weight maps to reject edge sources from the catalog at this phase of the analysis. We accomplish this by requiring that the mean value of the weight map in a 9 × 9 pixel area centered on the candidate source has a value of at least 20. For reference, all HOPS 70 $\mu$m scan maps have weight map values greater than 60 over most of the map areas.

The resulting preliminary source catalog includes all sources in the 70 $\mu$m images, i.e., previously identified Spitzer sources, new candidate protostars, nebulosity, and other undesirable features and artifacts in the images. We then cross-correlate this PACS 70 $\mu$m preliminary catalog with the existing Spitzer catalog to eliminate all previously identified protostars in each field that are brighter than the previously adopted 24 $\mu$m cutoff of 7 mag (Megeath et al. 2012). Therefore, our sample includes by definition only sources that are faint or undetected in the previous Spitzer catalog.

To identify previous source detections, we require that a source be matched to within a positional offset of 8″ when cross-correlated with the Spitzer catalog. This threshold is conservatively large compared to the Spitzer astrometry and is meant to encompass two main sources of astrometric error. First, it is possible that the absolute coordinates of a source may shift as a function of wavelength (although this effect is expected to be
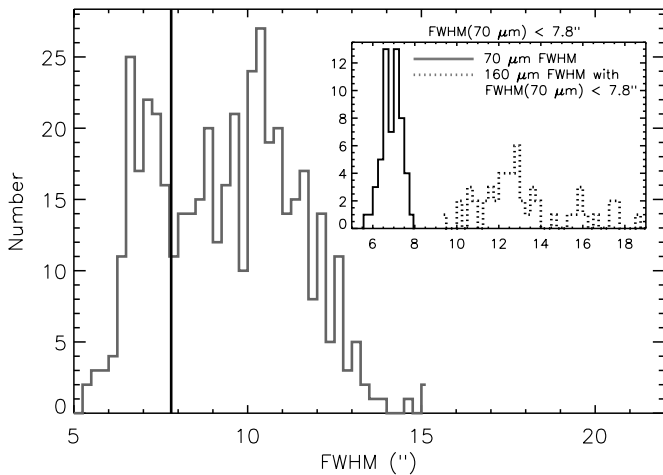
**Figure 1.** Frequency of 70 $\mu$m FWHM values for all sources detected in our HOPS images that have not been previously identified in the *Spitzer* catalog. The black line shows our adopted 7″.8 FWHM threshold, above which we reject all sources. Inset: the same as above for the subset of sources with both FWHM(70 $\mu$m) < 7″.8 and 160 $\mu$m detections (see Section 3). The dotted histogram indicates the 160 $\mu$m FWHM distribution.

relatively small) since different wavelengths may trace different material near the protostars. Second, the *Herschel* pointing accuracy, which is of order $\sim 2''$ ($1\sigma$), dominates the positional uncertainty for most sources when comparing the *Spitzer* catalog source coordinates to the *Herschel* 70 $\mu$m coordinates. To match coordinates robustly, we therefore adopt a conservatively large $8''$ threshold. We find that inspection of the matched sources by eye shows that this threshold works well and provides a low rate of mismatched or duplicate sources.

Our final goal is to obtain a sample of previously unidentified and uncharacterized *Herschel* protostar candidates. These sources should be characterized by a point-like appearance at 70 $\mu$m. Therefore, after rejecting all *Spitzer* protostars as described above, we next apply a simple FWHM (or apparent size) filter to the remaining 70 $\mu$m sources. The distribution of 70 $\mu$m azimuthally averaged FWHM values is shown in Figure 1 as the solid black histogram. We find a clear peak in the distribution at low FWHM values, indicating a population of point-like sources. Based on this distribution, we adopt an FWHM threshold of 7″.8, meant to select 70 $\mu$m point sources. We find 127 sources that fulfill the criteria listed here: 85 of these have 24 $\mu$m detections while 42 do not.

In a further step, we then require that all 70 $\mu$m sources also have a 160 $\mu$m detection and not upper limits. The 70 $\mu$m FWHM distribution of this subset of sources is shown in the inset of Figure 1 along with the corresponding 160 $\mu$m FWHM distribution. Our final sample consists of 55 candidate *Herschel* protostars with both 70 $\mu$m and 160 $\mu$m detections. Of these, 34 have *Spitzer* 24 $\mu$m detections fainter than 7.0 mag and 21 do not have any 24 $\mu$m detection.

### 3.1. Spitzer Non-detections

A search for newly detected protostars using *Herschel* requires us to determine upper limits at 24 $\mu$m for those sources that are not detected by *Spitzer*. To determine these limits, we adopt the method developed by Megeath et al. to assess the spatially varying completeness of the *Spitzer* Orion Survey data. The completeness of the 24 $\mu$m data depends strongly on the presence of nebulosity and point-source crowding. To account for these factors, we measure the fluctuations of the 24 $\mu$m signal in an annulus centered on the position of the *Herschel* point source using the root median square deviation, or RMEDSQ (see Equation (1) of Megeath et al. 2012). We then use the results from the artificial star tests (see the Appendix of Megeath et al. 2012) to determine the magnitude at which 90% of the point sources would be detected for the observed level of fluctuations. We convert this magnitude into a flux density to obtain 24 $\mu$m upper limits.

Several of the identified protostars show IRAC emission but are not included in the Megeath et al. point-source catalog because they are spatially extended. To obtain homogeneously extracted IRAC fluxes for the entire sample of sources, we measure fluxes using an aperture of 2 pixels, with a sky annulus of 2–6 pixels, corresponding to radii of 2″.44, 2″.44, and 7″.33, respectively, with a pixel scale of 1″.22 pixel$^{-1}$. We use the PACS 70 $\mu$m source coordinates as starting guesses, and attempt to recenter at each IRAC wavelength. If the re-centering fails, as for sources with no IRAC detections, we take the integrated flux in that aperture at the original PACS 70 $\mu$m source coordinate to be the upper limit. The aperture corrections and photometric zero points are those given by Kryukova et al.

### 3.2. Contamination in the Sample

Galaxies often exhibit infrared colors similar to those of young stellar objects (YSOs) due to the presence of dust and hydrocarbons in the galaxies (Stern et al. 2005). Extensive work has been done toward characterizing the extragalactic "contamination" in *Spitzer* surveys of star-forming regions and mitigating it through photometric criteria designed to separate galaxies from bona fide YSOs (Gutermuth et al. 2009, 2008; Harvey et al. 2007). These authors show that star-forming galaxies can be distinguished from YSOs by the galaxies' stellar-like emission in the IRAC 3.6 $\mu$m and 4.5 $\mu$m bands and their bright polycyclic aromatic hydrocarbon (PAH) emission in the IRAC 5.8 $\mu$m and 8.0 $\mu$m bands (Gutermuth et al. 2009, 2008; Winston et al. 2007; Stern et al. 2005). However, we note that some active galactic nuclei (AGNs) dominated galaxies may not exhibit PAH emission; therefore, an analysis based only on the IRAC colors may not capture all possible sources of contamination (Robitaille et al. 2008).

To analyze the IRAC colors of our sample, we define $\alpha = d\log(\lambda F_\lambda)/d\log(\lambda)$. In Figure 2, we plot $\alpha_{5.8-8}$ versus $\alpha_{3.6-4.5}$ for the sample of new *Herschel* sources with coverage in all four of the *Spitzer*/IRAC bands and detections in at least one band, compared to the HOPS protostar sample. This color index is relatively insensitive to reddening since the extinction in the 5.8 $\mu$m and 8 $\mu$m bands of IRAC are very similar (e.g., Flaherty et al. 2007; Gutermuth et al. 2008). Figure 2 shows a cluster of sources with high values of $\alpha_{5.8-8}$ (i.e., $\alpha_{5.8-8} \geqslant 3$; solid horizontal line) yet $\alpha_{3.6-4.5}$ values of an SED that is declining or flat with increasing wavelength. These sources show the characteristics of star-forming galaxies with bright PAH emission (resulting in high values of $\alpha_{5.8-8}$) but values of $\alpha_{3.6-4.5}$ that are dominated by starlight. In our adopted scheme, $\alpha_{5.8-8} \geqslant 3$ corresponds to a color of $[5.8] - [8] \geqslant 2.17$; this threshold is higher than the $[5.8] - [8] \geqslant 1$ threshold used by Gutermuth et al. (2008) to isolate galaxies and thus ensures that most protostellar candidates will be less likely to be misidentified extragalactic sources (Allen et al. 2004; Megeath et al. 2004). We identify the cluster of sources with $\alpha_{5.8-8} \geqslant 3$ and $\alpha_{3.6-4.5} \leqslant 0.5$ as likely extragalactic contamination. We note that nebular contamination of the photometry can cause PAH-like $\alpha_{5.8-8}$ values, and thus may
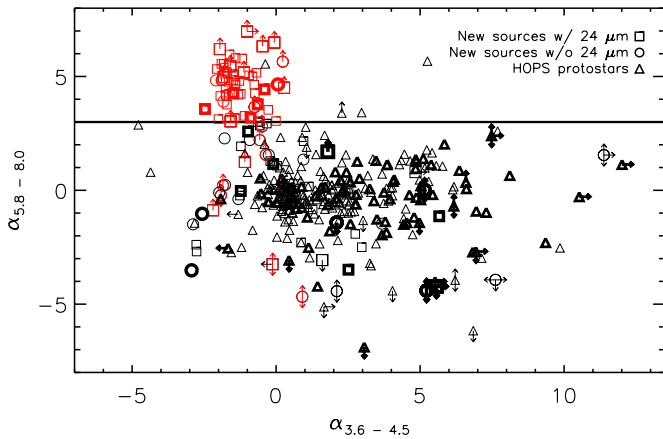
**Figure 2.** IRAC color indices $\alpha_{3.6-4.5}$ and $\alpha_{5.8-8.0}$ for sources detected in at least one IRAC band. The *Herschel* protostar candidate sample is shown as squares (sources with 24 $\mu$m detections) and circles (sources without 24 $\mu$m detections), while the HOPS protostar sample is shown as triangles. Thick bold points are sources with robust 870 $\mu$m detections. Candidate protostars with $\alpha_{5.8-8.0} > 3.0$ or upper limits consistent with this threshold are flagged as possible extragalactic contamination and highlighted in red. Note that some candidate protostars have both $\alpha_{5.8-8.0} > 3.0$ and a robust 870 $\mu$m detection; these sources are not considered extragalactic contamination.

(A color version of this figure is available in the online journal.)



**Figure 3.** IRAC and PACS 160 $\mu$m color indices $\alpha_{3.6-4.5}$ and $\alpha_{3.6-160}$ for the candidate protostar sample. Sources previously characterized as extragalactic based on their $\alpha_{5.8-8.0} > 3$ index (or limit) are indicated in red with a "G." Sources with $\alpha_{5.8-8.0} < 3$ are indicated in orange. The orange lines indicate the lower limits of $\alpha_{3.6-160}$ for sources with no IRAC detections. Sources with $\alpha_{3.6-160} > 1.2$ are considered highly probable protostars, while other sources are flagged as described in the text.

(A color version of this figure is available in the online journal.)

cause us to overestimate the extragalactic contamination. Of the 55 sources identified here as protostellar candidates, we flag 23 as possible extragalactic contamination based on this criterion. However, other sources of contamination, such as AGNs lacking PAH emission, may remain in our sample.

Inspection of the SEDs of the remaining 32 sources shows a range of SED slopes and shapes. It is possible that such sources may also be extragalactic contamination by AGN, for example. To address this, we further refine the analysis presented above by analyzing the 3.6 $\mu$m to 160 $\mu$m SED shapes with the spectral index $\alpha_{3.6-160}$. As illustrated in Figure 3, the sources flagged as extragalactic based on the $\alpha_{5.8-8}$ index (red points) generally have $\alpha_{3.6-160} \lesssim 1.2$. We therefore calibrate the $\alpha_{3.6-160}$ relative to the reliable extragalactic candidates with robust IRAC detections and expect that extragalactic sources will have $\alpha_{3.6-160} \lesssim 1.2$. Using this criterion, we refine our source classification as follows. All sources with $\alpha_{3.6-160} > 1.2$ (and $\alpha_{5.8-8} < 3$ when IRAC detections exist) are flagged as high probability protostars (flag = 1 in Table 3). Sources having values of $0.5 \lesssim \alpha_{3.6-160} \lesssim 1.2$ but that were originally classified as candidate protostars based on a low value of $\alpha_{5.8-8}$ are flagged as less likely to be of a protostellar nature (flag = 2 in Table 3). Furthermore, by definition, sources originally classified as extragalactic based on their PAH signature at 8 $\mu$m remain classified as such (flag = 3 in Table 3). Sources with $\alpha_{3.6-160} < 0.3$ and $\alpha_{3.6-4.5} \sim -3$ are flagged as "other" (flag = 4 in Table 3) since their SEDs are consistent with a stellar photosphere at shorter wavelengths. Finally, one source has no IRAC coverage and therefore is flagged with a value of 5. In Figure 4, we show example SEDs of each category.

Only one source (313006) originally flagged as extragalactic based on its $\alpha_{5.8-8}$ limit (non-detection at 5.8 $\mu$m and 8 $\mu$m) was revised to a highly probable protostar (see Figure 3 and the top left panel of Figure 4). In addition, as we note above, we find three sources with SEDs that we label "other" (flag value = 4) which are inconsistent with the categories described above. Source 069001 (see Figure 4, top right panel) was previously characterized by Fang et al. (2009) as a K7 star with a debris disk,
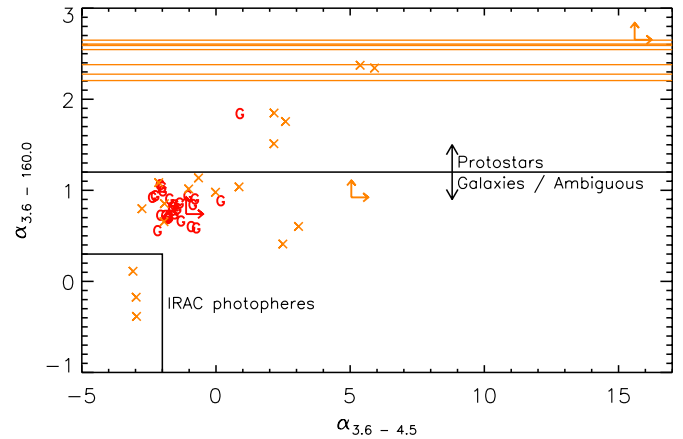
with a very poorly constrained age of $\sim$0.06$^{+4.66}_{-0.03}$ Myr. These authors only include data up to 24 $\mu$m. The SED we observe with *Herschel* may be consistent with a transition disk but not a debris disk. The remaining two sources in this category have similar SEDs as that of 069001; while a transition disk explanation for all three sources may appear likely depending on the age of the sources, we cannot currently rule out other possibilities. Nevertheless, all of these sources have SEDs consistent with a stellar photosphere in the IRAC bands, and hence these are likely to be fully formed stars surrounded by circumstellar dust.

Interestingly, we find that the most reliable SED classification criterion by far is that of sources that have neither IRAC nor MIPS 24 $\mu$m detections. Of these, we find that all six sources have strong sub-millimeter detections and reside in dense and filamentary environments. This finding points to the critical importance of obtaining high-resolution sub-millimeter data to constrain the properties of such sources. In the following text, we include all 55 *Herschel*-detected sources in our analysis and figures.

## 4. *HERSCHEL* PROTOSTAR CANDIDATES

We present the *Herschel* protostar candidate catalog in Table 3. Here we include the PACS 70 $\mu$m coordinates and flux measurements at 24 $\mu$m, 70 $\mu$m, and 160 $\mu$m. We indicate which sources are flagged as reliable protostellar candidates and which are likely contamination, based on the results from the previous section. We also indicate if the sources have a robust 870 $\mu$m detection. Furthermore, we present the values of $L_{\rm bol}$ and $T_{\rm bol}$ and their corresponding estimated statistical errors (see discussion in Section 5.1). In Figure 5, we show the 70 $\mu$m flux distributions for the sample compared to the distribution of HOPS protostars. The majority of the new candidate protostars have 70 $\mu$m fluxes that are lower than the previously identified *Spitzer* HOPS sample; this is not surprising since the new candidate protostar sample is selected to be faint or undetected at 24 $\mu$m. Furthermore, the peak at low 70 $\mu$m flux values is dominated by extragalactic contamination, as discussed above.

In Figure 6, we show the MIPS 24 $\mu$m, PACS 70 $\mu$m, and PACS 160 $\mu$m colors of the new *Herschel* sources compared to

**Table 3**
*Herschel* Protostar Candidate Coordinates and Photometry

| Source | Group Name | R.A.[a] (h:m:s) | Decl.[a] (°:′:″) | Field | 24 $\mu$m (mJy) | 70 $\mu$m (mJy) | 160 $\mu$m (mJy) | Flag[b] | 870 $\mu$m Detection[c] | $T_{bol}$ (K) | $L_{bol}$ ($L_\odot$) |
|---|---|---|---|---|---|---|---|---|---|---|---|
| **061012** | 061 | 05:42:48.87 | −08:16:10.70 | L1641 | ⩽1.14 | 703 ± 35 | 5634 ± 845 | 1 | ... | 32.1 ± 0.9 | 0.75 ± 0.06 |
| **119019** | 119 | 05:40:58.47 | −08:05:36.10 | L1641 | 1.46 ± 0.2 | 1604 ± 80. | 10745 ± 1612 | 1 | Yes | 34.4 ± 0.8 | 1.56 ± 0.14 |
| 026011 | 026 | 05:39:17.00 | −07:24:26.64 | L1641 | ⩽1.30 | 78.4 ± 3.9 | 2516 ± 377 | 1 | Yes | 23.0 ± 1.0 | 0.34 ± 0.03 |
| 313006 | 313 | 05:39:30.75 | −07:23:59.40 | L1641 | ⩽1.25 | 138 ± 7. | 2198 ± 330 | 1 | Yes | 27.8 ± 1.0 | 0.28 ± 0.03 |
| 029003 | 029 | 05:39:13.15 | −07:13:11.69 | L1641 | 1.19 ± 0.2 | 29.5 ± 1.5 | 365 ± 55 | 1 | ... | 42.0 ± 1.5 | 0.06 ± 0.01 |
| **019003** | 019 | 05:35:23.92 | −05:07:53.46 | ONC | ⩽16.2 | 2506 ± 127 | 31577 ± 4737 | 1 | Yes | 33.6 ± 1.1 | 3.16 ± 0.31 |
| **082005** | 082 | 05:41:29.40 | −02:21:17.06 | NGC 2024 | ⩽3.13 | 506 ± 25 | 9308 ± 140 | 1 | Yes | 29.3 ± 0.8 | 1.02 ± 0.11 |
| **082012** | 082 | 05:41:24.94 | −02:18:08.54 | NGC 2024 | 6.51 ± 0.4 | 4571 ± 229 | 51254 ± 7688 | 1 | Yes | 32.2 ± 0.9 | 6.27 ± 0.65 |
| **090003** | 090 | 05:42:45.23 | −01:16:14.18 | NGC 2024 | 4.74 ± 0.3 | 3286 ± 164 | 16937 ± 2541 | 1 | Yes | 36.0 ± 0.8 | 2.71 ± 0.24 |
| **091015** | 091 | 05:46:07.65 | −00:12:20.73 | NGC 2068 | ⩽1.29 | 648 ± 32 | 6615 ± 992 | 1 | Yes | 30.9 ± 0.8 | 0.81 ± 0.07 |
| **091016** | 091 | 05:46:09.97 | −00:12:16.85 | NGC 2068 | ⩽1.14 | 431 ± 22 | 5108 ± 766 | 1 | Yes | 29.1 ± 0.9 | 0.65 ± 0.06 |
| **093005** | 093 | 05:46:27.75 | −00:00:53.81 | NGC 2068 | ⩽1.14 | 1427 ± 71. | 12131 ± 1820 | 1 | Yes | 30.8 ± 0.9 | 1.71 ± 0.15 |
| **302002** | 302 | 05:46:28.24 | 00:19:27.00 | NGC 2068 | ⩽1.14 | 302 ± 15 | 7187 ± 108 | 1 | Yes | 28.6 ± 0.9 | 0.84 ± 0.09 |
| **097002** | 097 | 05:48:07.76 | 00:33:50.79 | NGC 2068 | ⩽1.14 | 1049 ± 52. | 7993 ± 120 | 1 | Yes | 33.4 ± 0.9 | 1.14 ± 0.11 |
| 300001 | 300 | 05:47:43.36 | 00:38:22.43 | NGC 2068 | ⩽7.19 | 478 ± 24 | 5042 ± 756 | 1 | Yes | 29.6 ± 0.9 | 0.65 ± 0.06 |
| 068006 | 068 | 05:41:11.79 | −07:53:35.09 | L1641 | 9.19 ± 0.2 | 44.8 ± 2.2 | 146 ± 22 | 2 | ... | 149.7 ± 5.06 | 0.05 ± 0.01 |
| 038002 | 038 | 05:36:11.11 | −06:49:11.29 | L1641 | ⩽1.25 | 36.4 ± 1.8 | 537 ± 81 | 2 | ... | 40.4 ± 1.0 | 0.10 ± 0.01 |
| 037003 | 037 | 05:37:00.35 | −06:37:10.95 | L1641 | 8.85 ± 0.2 | 725 ± 36 | 3798 ± 570 | 2 | ... | 53.1 ± 1.7 | 0.43 ± 0.03 |
| 037008 | 037 | 05:37:34.31 | −06:35:20.33 | L1641 | ⩽1.39 | 27.7 ± 1.4 | 321 ± 48 | 2 | ... | 45.5 ± 1.9 | 0.04 ± 0.01 |
| 092011 | 092 | 05:46:26.17 | −00:04:45.31 | NGC 2068 | 2.31 ± 0.2 | 77.8 ± 3.9 | 363 ± 54 | 2 | ... | 104.1 ± 5.63 | 0.05 ± 0.01 |
| 093001 | 093 | 05:46:56.32 | −00:03:14.73 | NGC 2068 | ⩽1.14 | 21.8 ± 1.1 | 217 ± 33 | 2 | Yes | 47.9 ± 0.7 | 0.05 ± 0.01 |
| 302004 | 302 | 05:46:16.55 | 00:21:35.09 | NGC 2068 | 2.87 ± 0.2 | 108 ± 5. | 283 ± 42 | 2 | ... | 54.8 ± 1.8 | 0.07 ± 0.01 |
| 096023 | 096 | 05:46:53.23 | 00:22:10.05 | NGC 2068 | ⩽2.13 | 147 ± 7. | 1691 ± 254 | 2 | ... | 39.6 ± 1.4 | 0.18 ± 0.02 |
| 301003 | 301 | 05:46:02.15 | 00:23:29.86 | NGC 2068 | 8.08 ± 0.2 | 42.6 ± 2.1 | 231 ± 35 | 2 | ... | 92.1 ± 3.8 | 0.05 ± 0.01 |
| 000011 | 000 | 05:54:32.10 | 01:42:54.92 | L1622 | ⩽1.25 | 28.5 ± 1.4 | 147 ± 22 | 2 | ... | 50.1 ± 0.5 | 0.06 ± 0.01 |
| 053002 | 053 | 05:43:24.07 | −08:49:03.75 | $\kappa$Ori | ⩽1.38 | 33.5 ± 1.7 | 190 ± 28 | 3 | ... | 43.2 ± 0.3 | 0.06 ± 0.01 |
| 117004 | 117 | 05:41:40.40 | −08:41:40.60 | L1641 | 1.17 ± 0.2 | 25.3 ± 1.3 | 234 ± 35 | 3 | ... | 56.4 ± 2.2 | 0.04 ± 0.01 |
| 117014 | 117 | 05:41:29.28 | −08:36:14.60 | L1641 | 1.20 ± 0.2 | 31.0 ± 1.6 | 237 ± 36 | 3 | ... | 32.2 ± 2.4 | 0.11 ± 0.01 |
| 119016 | 119 | 05:40:40.54 | −08:05:55.00 | L1641 | 1.97 ± 0.2 | 42.7 ± 2.1 | 148 ± 22 | 3 | ... | 62.7 ± 1.7 | 0.05 ± 0.01 |
| 121011 | 121 | 05:41:37.90 | −07:55:44.35 | L1641 | 1.46 ± 0.2 | 74.1 ± 3.7 | 193 ± 29 | 3 | ... | 51.6 ± 1.5 | 0.04 ± 0.01 |
| 025044 | 025 | 05:39:56.80 | −07:19:21.40 | L1641 | ⩽1.18 | 23.1 ± 1.2 | 150 ± 22 | 3 | ... | 42.2 ± 0.2 | 0.08 ± 0.01 |
| 030013 | 030 | 05:38:59.58 | −07:10:31.92 | L1641 | 1.43 ± 0.2 | 25.9 ± 1.3 | 153 ± 23 | 3 | ... | 48.0 ± 1.0 | 0.05 ± 0.01 |
| 031003 | 031 | 05:38:55.35 | −07:05:29.17 | L1641 | 2.96 ± 0.2 | 49.9 ± 2.5 | 175 ± 26 | 3 | ... | 67.7 ± 1.8 | 0.06 ± 0.01 |
| 034010 | 034 | 05:37:54.76 | −06:56:59.65 | L1641 | ⩽1.14 | 61.3 ± 3.1 | 249 ± 37 | 3 | ... | 43.5 ± 0.7 | 0.15 ± 0.01 |
| 031037 | 031 | 05:38:28.20 | −06:56:40.16 | L1641 | ⩽1.14 | 64.3 ± 3.2 | 396 ± 59 | 3 | ... | 51.9 ± 2.4 | 0.06 ± 0.01 |
| 034014 | 034 | 05:38:14.92 | −06:53:03.56 | L1641 | 1.89 ± 0.2 | 47.4 ± 2.4 | 235 ± 35 | 3 | ... | 65.5 ± 3.5 | 0.03 ± 0.01 |
| 036003 | 036 | 05:38:05.97 | −06:50:58.91 | L1641 | 1.74 ± 0.2 | 67.4 ± 3.4 | 291 ± 44 | 3 | ... | 74.6 ± 3.1 | 0.04 ± 0.01 |
| 036006 | 036 | 05:37:45.07 | −06:50:02.39 | L1641 | 2.83 ± 0.2 | 34.8 ± 1.7 | 143 ± 22 | 3 | ... | 60.1 ± 1.8 | 0.04 ± 0.01 |
| 036011 | 036 | 05:37:42.72 | −06:47:08.31 | L1641 | 2.68 ± 0.2 | 41.8 ± 2.1 | 159 ± 24 | 3 | Yes | 65.9 ± 1.9 | 0.05 ± 0.01 |
| 037011 | 037 | 05:37:37.80 | −06:34:43.35 | L1641 | 2.42 ± 0.2 | 58.0 ± 2.9 | 409 ± 61 | 3 | ... | 69.6 ± 3.0 | 0.04 ± 0.01 |
| 050006 | 050 | 05:34:23.01 | −06:32:58.00 | L1641 | 2.82 ± 0.2 | 45.5 ± 2.3 | 313 ± 47 | 3 | ... | 60.3 ± 2.3 | 0.06 ± 0.01 |
| 037013 | 037 | 05:37:22.00 | −06:32:56.48 | L1641 | 2.93 ± 0.2 | 52.0 ± 2.6 | 180 ± 27 | 3 | ... | 62.7 ± 1.8 | 0.05 ± 0.01 |
| 041001 | 041 | 05:36:28.68 | −06:30:42.13 | L1641 | 2.72 ± 0.2 | 47.5 ± 2.4 | 262 ± 39 | 3 | ... | 90.7 ± 4.8 | 0.03 ± 0.01 |
| 009001 | 009 | 05:33:32.55 | −05:53:34.25 | ONC | 4.83 ± 0.3 | 74.9 ± 3.8 | 245 ± 37 | 3 | ... | 95.4 ± 2.6 | 0.05 ± 0.01 |
| 021010 | 021 | 05:34:19.63 | −04:53:23.54 | ONC | 11.3 ± 0.5 | 316 ± 16 | 678 ± 10 | 3 | ... | 63.8 ± 2.2 | 0.18 ± 0.01 |
| 303017 | 303 | 05:47:49.01 | 00:20:26.47 | NGC 2068 | 4.64 ± 0.2 | 107 ± 5. | 634 ± 95 | 3 | ... | 70.2 ± 3.8 | 0.10 ± 0.01 |
| 303023 | 303 | 05:47:45.58 | 00:21:14.68 | NGC 2068 | 4.36 ± 0.2 | 65.9 ± 3.3 | 234 ± 35 | 3 | ... | 104.1 ± 4.81 | 0.04 ± 0.01 |
| 098001 | 098 | 05:47:25.77 | 00:33:37.43 | NGC 2068 | 1.73 ± 0.2 | 9.79 ± 0.5 | 231 ± 35 | 3 | ... | 43.5 ± 2.1 | 0.03 ± 0.01 |
| 097003 | 097 | 05:47:45.88 | 00:34:12.71 | NGC 2068 | 1.37 ± 0.2 | 13.0 ± 0.7 | 137 ± 21 | 3 | ... | 78.1 ± 4.4 | 0.02 ± 0.01 |
| 000003 | 000 | 05:54:17.28 | 01:40:18.68 | L1622 | 8.63 ± 0.4 | 165 ± 8. | 386 ± 58 | 3 | ... | 82.5 ± 3.3 | 0.10 ± 0.01 |
| 000010 | 000 | 05:54:37.27 | 01:42:52.39 | L1622 | 5.10 ± 0.3 | 64.7 ± 3.2 | 215 ± 32 | 3 | ... | 89.2 ± 3.9 | 0.04 ± 0.01 |
| 069001 | 069 | 05:40:46.20 | −08:04:35.12 | L1641 | 5.13 ± 0.2 | 325 ± 16 | 722 ± 11 | 4 | ... | 336.1 ± 14.7 | 0.29 ± 0.01 |
| 026001 | 026 | 05:39:18.49 | −07:27:52.37 | L1641 | 4.71 ± 0.2 | 223 ± 11 | 598 ± 90 | 4 | ... | 224.4 ± 11.2 | 0.17 ± 0.01 |
| 306004 | 306 | 05:35:24.66 | −04:49:43.53 | ONC | ⩽124 | 435 ± 22 | 637 ± 96 | 4 | ... | 119.1 ± 3.56 | 0.33 ± 0.01 |
| 006006 | 006 | 05:35:11.47 | −05:57:05.09 | L1641 | 5.06 ± 0.2 | 126 ± 6. | 4027 ± 604 | 5 | Yes | 27.7 ± 0.6 | 0.31 ± 0.04 |

**Notes.** Sources indicated in bold are those with log($\lambda F_\lambda 70/\lambda F_\lambda 24$) > 1.65. The ONC field contains the extended Orion Nebula region, the NGC 1977 region, and OMC2/3; the NGC 2024 field contains the NGC 2024 H II region and the NGC 2023 reflection nebula. The NGC 2068 field includes the NGC 2068 and NGC 2071 reflection nebulae as well as LBS23 region.
[a] PACS 70 $\mu$m source coordinates.
[b] This column indicates if a source is flagged as a reliable protostar (value = 1), if the source is considered less likely to be a protostar (value = 2), if the source is flagged as extragalactic contamination (value = 3), and if the SED shape is with IRAC photospheric emission (value = 4). Finally, one source has no IRAC coverage (value = 5).
[c] This column indicates if the source has a strong 870 $\mu$m detection; sources with no data are either assigned upper limits or have no coverage.
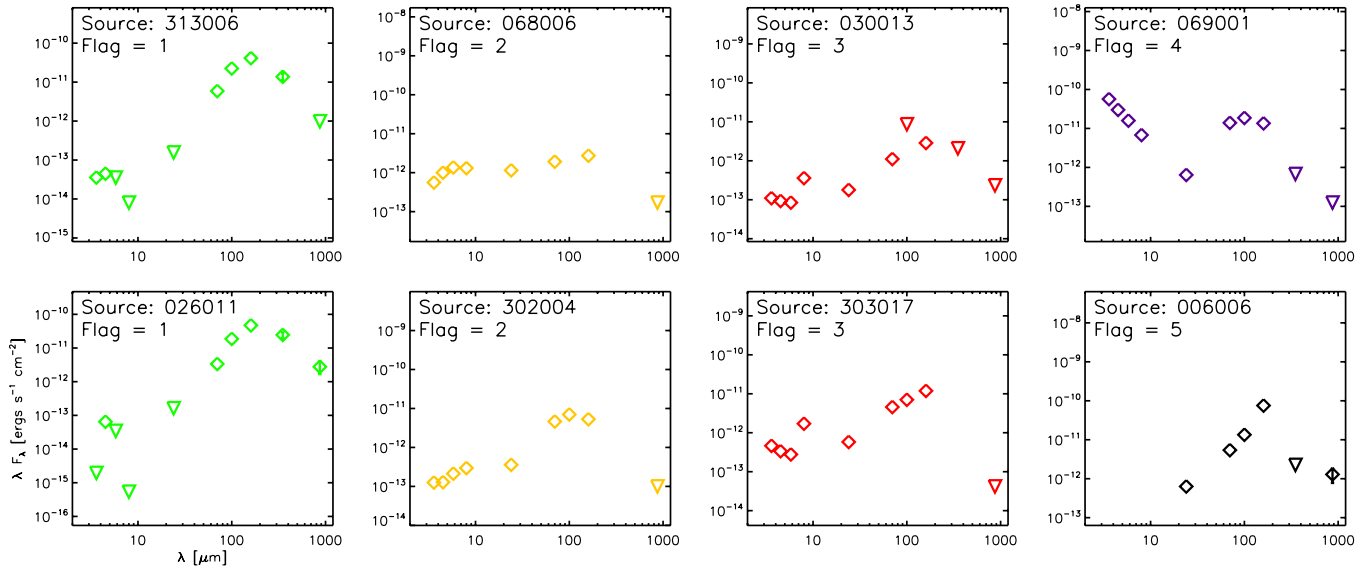
**Figure 4.** Example SEDs for each of the five categories described in Section 3.2: green SEDs (flag = 1) are considered to be reliable protostar candidates, yellow SEDs (flag = 2) are less likely to be protostellar, red SEDs (flag = 3) are considered extragalactic contamination based on the 8 $\mu$m PAH feature, the purple SED (flag = 4) is an example of one of the three sources that may be explained as transition disks, and, finally, the black SED (flag = 5) is unclassifiable due to the lack of IRAC coverage. Errors are smaller than the size of the points, except for the 350 $\mu$m and 870 $\mu$m points; upper limits are indicated with triangles.

(A color version of this figure is available in the online journal.)
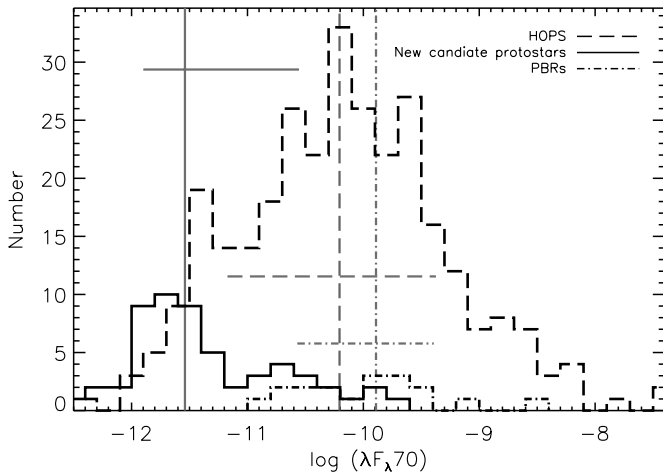


**Figure 5.** Distributions of 70 $\mu$m fluxes for the HOPS protostars (dashed histogram), new candidate protostars (solid histogram), and the 18 reddest sources drawn from both combined samples (dot-dashed histogram). The corresponding gray lines indicate the median flux values (vertical lines) and the 68% interval (horizontal lines).

the HOPS sample of 70 $\mu$m detected protostars. The top panel shows the 70 $\mu$m flux versus the log ($\lambda F_\lambda 70/\lambda F_\lambda 24$) color (henceforth 70/24 color), while the bottom panel shows the log ($\lambda F_\lambda 160/\lambda F_\lambda 70$) color (henceforth 160/70 color) versus the 70/24 color, for our sample of new protostar candidates compared to the colors of the *Spitzer*-identified HOPS sample. The *Spitzer* 24 $\mu$m 7 mag limit, imposed on the HOPS sample for a reliable protostellar identification, is apparent in the top panel as the diagonal line approximately separating the new protostellar candidates at fainter 70 $\mu$m fluxes and redder 70/24 colors from the population of *Spitzer*-identified HOPS sources.

For comparison, in the top panel of Figure 6, we also show the fluxes and colors of presumably typical and well-studied Class 0 sources: VLA1632-243 (J. Green and DIGIT team 2012, private

communication and J. Green et al., in preparation), IRAS16293 (Evans et al. 2009), B335 (Stutz et al. 2008; Launhardt et al. 2013), CB68 (Launhardt et al. 2013), and CB244 (Stutz et al. 2010; Launhardt et al. 2013). Furthermore, we also show the colors of various VeLLOs: L673-7 (Dunham et al. 2008), IRAM04191 (Dunham et al. 2006), and CB130 (Launhardt et al. 2013). We find that the observed colors of our sample of candidate protostars appear consistent with the colors of more nearby Class 0 and VeLLO sources but not with FHSC candidate colors proposed in the literature (e.g., Commerçon et al. 2012). We find that the majority of these previously known Class 0 and VeLLO sources do not appear as red in their 70/24 colors as the reddest sources in our sample. The only exceptions to this trend are IRAS16293 and VLA1632-243, perhaps representing an extremum in the 70/24 color distribution that may be driven by their comparatively large envelope densities.

We also show in Figure 6 the colors of two FHSC candidates in Perseus: Per-Bolo 58 (Enoch et al. 2010) and B1-bS (Pezzuto et al. 2012). In this diagram, the 70/24 color of Per-Bolo 58 appears generally consistent with that of a VeLLO, as Enoch et al. (2010) point out. As such, this source may be an extremely low-mass protostar. On the other hand, the 70/24 color of B1-bS is comparable to the very reddest sources we find in Orion while the 70 $\mu$m flux is consistent with VeLLOs and fainter than the reddest sources in Orion by more than one order of magnitude. The faint but robust detection of a 70 $\mu$m point source by Pezzuto et al. (2012) may indeed point to the possible Class 0 or VeLLO nature of B1-bS. We do however note that Pezzuto et al. also detect a source with no 70 $\mu$m counterpart, B1-bN, which may therefore represent a more robust FHSC candidate. Regardless of the elusive nature of FHSC candidates, when comparing our new candidate protostar colors to FHSC models by Commerçon et al. (2012), we find that our sources do not appear to be consistent with predicted or expected FHSC colors, with the caveat that distinguishing FHSCs from VeLLOs with continuum observations alone is likely difficult.
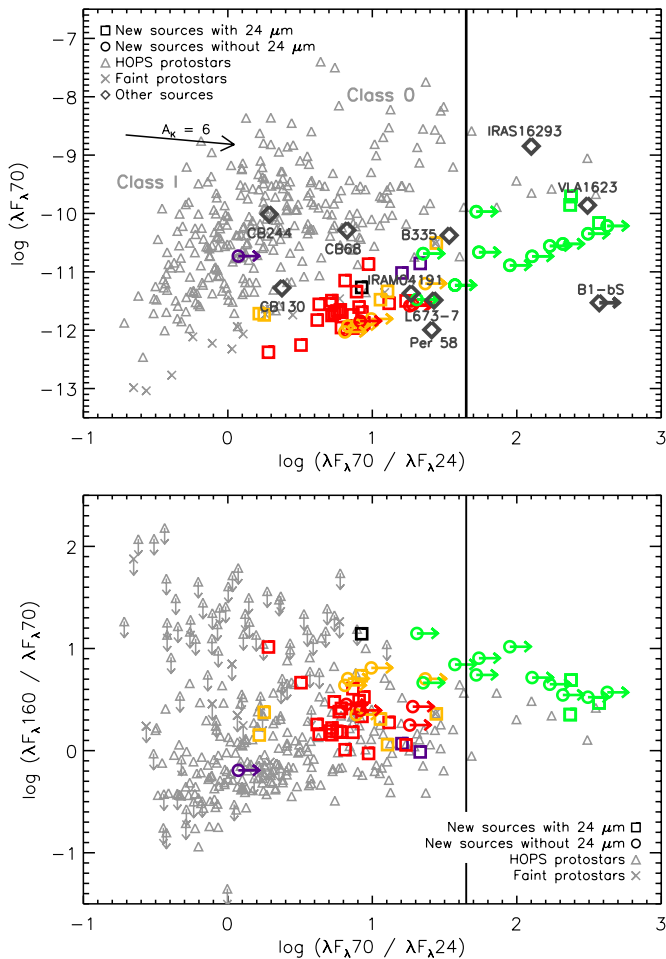
**Figure 6.** Top: 70 $\mu$m flux vs. 70 $\mu$m to 24 $\mu$m flux ratio for HOPS-detected Orion protostars. Open squares and open circles indicate the new candidate protostars with and without MIPS 24 $\mu$m detections, respectively. The color of the symbols indicates the flag values shown in Table 3 and discussed in Section 3.2: here, green indicates sources that are reliable protostar candidates (flag = 1), orange indicates less reliable sources (flag = 2), red indicates extragalactic contamination (flag = 3), purple indicates other sources (flag = 4), and black indicates the single source without IRAC coverage. The solid vertical line indicates a 70 $\mu$m to 24 $\mu$m flux ratio of 1.65, our PBRs selection criterion (see Section 5). Triangles and $\times$ symbols indicate previously detected and characterized *Spitzer* protostars and faint protostellar candidates from Megeath et al. (2012), respectively. The arrow indicates the extinction vector for a value of $A_K = 6$. For comparison, we also indicate as large diamonds the scaled observed measurements for some well-known Class 0 sources, VeLLOs, and two FHSC candidates (Per 58 and B1-bS; see Section 4). Bottom: 160 $\mu$m to 70 $\mu$m flux ratio vs. 70 $\mu$m to 24 $\mu$m flux ratio for HOPS-detected Orion protostars. The symbol and color type is the same as in the top panel. The reddest sources are distinguished from the bulk of *Spitzer*-identified HOPS sources (triangles) both by brighter 160 $\mu$m fluxes and redder 70 $\mu$m to 24 $\mu$m flux ratios.

(A color version of this figure is available in the online journal.)

## 5. PACS BRIGHT RED SOURCES

Up to this point, we have discussed two distinct and well-defined samples of sources in Orion: (1) the sample of candidate protostars identified with *Herschel* that have PACS 70 $\mu$m and 160 $\mu$m detections but MIPS 24 $\mu$m magnitudes greater than 7.0 mag and (2) the sample of protostars that were reliably identified with *Spitzer* (24 $\mu$m magnitudes $\leqslant$7.0 mag; Megeath et al. 2012; Kryukova et al. 2012). The protostar catalog target list used for the HOPS program consists mostly of the *Spitzer* identified protostars, but also contains some of the previously

known protostars with $m(24) > 7.0$ mag (W. J. Fischer et al., in preparation).

In what follows, we focus our analysis on the Orion protostars that have $70/24 > 1.65$. Of the 18 known protostars that satisfy this limit, 11 are identified with *Herschel*; hence this color regime is dominated by our newly identified protostars. Accordingly, *Herschel* has provided us for the first time with a far more complete sample of these red sources within the field of the HOPS survey. Given their red colors and their brightness in the PACS wavelength bands, we refer to this sample of protostars as PBRs. The coordinates, *Spitzer* photometry, and *Herschel* photometry of the sample are listed in Table 4, while the APEX 350 $\mu$m and 870 $\mu$m photometry are presented in Table 5. Since the APEX photometry are non-trivial to extract due in large part to contamination by cold surrounding material and, at 870 $\mu$m specifically, by the large beam size, we present three measures of the source flux, as described above.

### 5.1. Observed Properties of PBRs

As discussed above, we select 18 PBRs in Orion with observed 70/24 colors greater than 1.65. We show 4.5 $\mu$m to 870 $\mu$m images of five example PBRs in Figures 7 and 8 (see Appendix B for the full sample images). Furthermore, in Figure 9 we show the full set of 18 PBRs' observed SEDs from 24 $\mu$m to 870 $\mu$m. Inspection of the observed SEDs confirms that the PBRs sample is composed of cold, envelope-dominated sources with peak emission always located at $\lambda > 70$ $\mu$m. In addition, the peak of the SEDs, and thus the temperatures, are well constrained for all PBRs because we have obtained APEX sub-millimeter coverage for all sources.

In Table 6, we present some basic properties of the PBRs. In particular, we find that 12/18 sources exhibit *Spitzer* 4.5 $\mu$m emission indicative of outflow activity. We also include some references to previous detections (see Appendix A). Furthermore, 4/18 sources have significant levels of 4.5 $\mu$m emission that are indeed consistent with a high inclination. The majority of sources, however, do not give clear indications of their inclinations at any observed wavelength, and therefore we cannot make any statements about their possible orientations based on their appearance in the images. We find indications from the 4.5 $\mu$m image morphology that two sources (HOPS341 and HOPS354) are binaries, while seven sources have a nearby source within 30″. Two reside in more crowded regions, and seven sources appear truly isolated. We find that a significant fraction (13/18) of sources appear to reside in filamentary regions, i.e., the extended 870 $\mu$m emission appears significantly elongated.

The four sources with significant indications of a high inclination orientation are HOPS169, 302002, HOPS341, and HOPS354 (see Appendix B for Figures 17, 21, 23, and 25). Inspection of their 4.5 $\mu$m images reveals that their outflows appear well collimated and relatively narrow. Indeed, we might expect that sources that have denser envelopes, and are therefore presumably younger, may have narrower cavity opening angles (e.g., Arce & Sargent 2006). As an additional check on our density analysis (see Section 6), we use this inclination information for an independent check of the envelope densities of these four sources. Despite the relatively sparsely sampled SEDs, we fix the inclination to 87° and fit the source SEDs. We find that even when we fix the model inclination to $\theta = 87°$, we still obtain envelope densities significantly above the $\rho_1$ value found in Section 6.

**Table 4**
*Spitzer* and *Herschel* Photometric Properties of PACS Bright Red Sources

| Source | HOPS Group Name | R.A.[a] (h:m:s) | Decl.[a] (°:′:″) | Field | 24 μm (mJy) | 70 μm (mJy) | 100 μm (mJy) | 160 μm (mJy) | log 70/24[b] |
|---|---|---|---|---|---|---|---|---|---|
| 061012 | 061 | 05:42:48.8 | −08:16:10.70 | L1641 | ⩽1.14 | 703 ± 35 | 2018 ± 517 | 5634 ± 845 | ⩾2.31 |
| 119019 | 119 | 05:40:58.4 | −08:05:36.10 | L1641 | 1.46 ± 0.2 | 1604 ± 80. | 5789 ± 148 | 10745 ± 1612 | 2.56 |
| HOPS169 | 040 | 05:36:36.0 | −06:38:54.02 | L1641 | 4.80 ± 0.5 | 5001 ± 250 | 15753 ± 4033 | 29975 ± 4496 | 2.54 |
| 019003 | 019 | 05:35:23.9 | −05:07:53.46 | ONC | ⩽16.2 | 2506 ± 127 | 4711 ± 121 | 31577 ± 4737 | ⩾1.71 |
| 082005 | 082 | 05:41:29.4 | −02:21:17.06 | NGC 2024 | ⩽3.13 | 506 ± 25 | 3003 ± 769 | 9308 ± 140 | ⩾1.73 |
| HOPS372 | 082 | 05:41:26.3 | −02:18:21.08 | NGC 2024 | 12.0 ± 1.2 | 6178 ± 309 | 16217 ± 4151 | 31090 ± 4664 | 2.24 |
| 082012 | 082 | 05:41:24.9 | −02:18:08.54 | NGC 2024 | 6.51 ± 0.4 | 4571 ± 229 | 20357 ± 5211 | 51254 ± 7688 | 2.37 |
| 090003 | 090 | 05:42:45.2 | −01:16:14.18 | NGC 2024 | 4.74 ± 0.3 | 3286 ± 164 | 10914 ± 2794 | 16937 ± 2541 | 2.36 |
| HOPS358 | 091 | 05:46:07.2 | −00:13:30.86 | NGC 2068 | 422 ± 42 | 60681 ± 3041 | 104322 ± 26706 | 123207 ± 18481 | 1.68 |
| 091015 | 091 | 05:46:07.6 | −00:12:20.73 | NGC 2068 | ⩽1.29 | 648 ± 32 | 2543 ± 651 | 6615 ± 992 | ⩾2.22 |
| 091016 | 091 | 05:46:09.9 | −00:12:16.85 | NGC 2068 | ⩽1.14 | 431 ± 22 | 1977 ± 506 | 5108 ± 766 | ⩾2.10 |
| HOPS373 | 093 | 05:46:30.7 | −00:02:36.80 | NGC 2068 | 14.1 ± 1.4 | 5258 ± 263 | 20188 ± 5168 | 36724 ± 5509 | 2.10 |
| 093005 | 093 | 05:46:27.7 | −00:00:53.81 | NGC 2068 | ⩽1.14 | 1427 ± 71. | 5373 ± 138 | 12131 ± 1820 | ⩾2.62 |
| 302002 | 302 | 05:46:28.2 | 00:19:27.00 | NGC 2068 | ⩽1.14 | 302 ± 15 | 3101 ± 794 | 7187 ± 108 | ⩾1.95 |
| HOPS359 | 303 | 05:47:24.8 | 00:20:58.24 | NGC 2068 | 22.8 ± 2.3 | 20758 ± 1039 | 43592 ± 1116 | 60409 ± 9061 | 2.48 |
| HOPS341 | 128 | 05:47:00.9 | 00:26:20.76 | NGC 2068 | 14.0 ± 1.4 | 3001 ± 301 | 15138 ± 3875 | 25213 ± 3782 | 1.86 |
| 097002 | 097 | 05:48:07.7 | 00:33:50.79 | NGC 2068 | ⩽1.14 | 1049 ± 52. | 4163 ± 107 | 7993 ± 120 | ⩾2.49 |
| HOPS354 | 000 | 05:54:24.1 | 01:44:20.15 | L1622 | 28.9 ± 2.9 | 8492 ± 426 | 37423 ± 9580 | 39258 ± 5889 | 1.99 |

**Notes.** The ONC field contains the extended Orion Nebula region, the NGC 1977 region, and OMC2/3; the NGC 2024 field contains the NGC 2024 H II region and the NGC 2023 reflection nebula. The NGC 2068 field includes the NGC 2068 and NGC 2071 reflection nebulae as well as LBS23 region.
[a] Object coordinates are derived from the PACS 70 μm images.
[b] $\log \lambda F_\lambda 70 / \lambda F_\lambda 24$.

**Table 5**
APEX 350 and 870 μm Photometry of PACS Bright Red Sources

| Source | 350 μm (Jy beam⁻¹) | 350 μm[a] (Jy) | 350 μm[b] (Jy) | 870 μm (Jy beam⁻¹) | 870 μm[a] (Jy) | 870 μm[b] (Jy) |
|---|---|---|---|---|---|---|
| 061012 | 2.60 | 3.93 | 2.53 | ⩽0.7 | ⩽1.3 | ⩽1.3 |
| 119019 | 3.38 | 5.27 | 3.63 | 0.5 | 0.9 | 0.6 |
| HOPS169 | ... | ... | ... | 1.0 | 1.6 | 1.4 |
| 019003 | 8.29 | 19.6 | 7.18 | 2.5 | 5.0 | 3.0 |
| 082005 | ... | ... | ... | 0.8 | 1.6 | 1.0 |
| HOPS372 | ... | ... | ... | ⩽1.4 | ⩽4.0 | ⩽4.0 |
| 082012 | ... | ... | ... | 2.7 | 4.3 | 3.6 |
| 090003 | 3.63[c] | ... | ... | 1.7 | 2.2 | 1.9 |
| HOPS358 | 13.0 | 22.4 | 17.3 | 1.8 | 3.3 | 2.6 |
| 091015 | 2.14 | 3.15 | 2.26 | 0.6 | 1.3 | 0.5 |
| 091016 | 2.50 | 3.76 | 2.81 | 0.7 | 1.2 | 0.8 |
| HOPS373 | 9.02 | 12.9 | 10.5 | 1.5 | 2.5 | 2.0 |
| 093005 | 6.58 | 10.1 | 6.74 | 1.4 | 2.6 | 1.6 |
| 302002 | ... | ... | ... | 1.1 | 1.7 | 1.5 |
| HOPS359 | ... | ... | ... | 1.8 | 2.9 | 2.2 |
| HOPS341 | ... | ... | ... | 1.0 | 1.5 | 1.3 |
| 097002 | ... | ... | ... | 0.6 | 0.9 | 0.8 |
| HOPS354 | 13.8 | 25.9 | 18.7 | 1.5 | 2.7 | 2.2 |

**Notes.**
[a] Source flux measured in an aperture with radius equal to 1×FWHM, where the FWHM = 7″34 and 19″0 at 350 and 870 μm, respectively.
[b] Source flux measured in the same aperture as in "a" but with local sky subtraction over radii equal to {1.5, 2.0}×FWHM.
[c] 350 μm point from Miettinen et al. (2012).

### 5.2. Observational Evolutionary Diagnostics

We calculate $L_{bol}$, $T_{bol}$ (Myers & Ladd 1993), and $L_{smm}/L_{bol}$ (André et al. 1993, 2000). The errors in $L_{bol}$ and $T_{bol}$ are derived with the same Monte Carlo method as described in Section 6.2 for the modified blackbody parameters. We exclude the IRAC upper limits from this analysis; including these limits has an effect on our $L_{bol}$ and $T_{bol}$ estimates that is smaller than our

estimated errors. We do, however, include the 24 μm upper limits; therefore, the $L_{bol}$ and $T_{bol}$ values should be considered upper limits for sources not detected at this wavelength. Furthermore, we investigate the effect of applying an average foreground reddening correction to all the new *Herschel* candidate protostars. We find that dereddening the observed fluxes with extinction levels of $A_V = 40$ mag has no effect on the derived parameters because the observed SEDs are extremely red and cold.
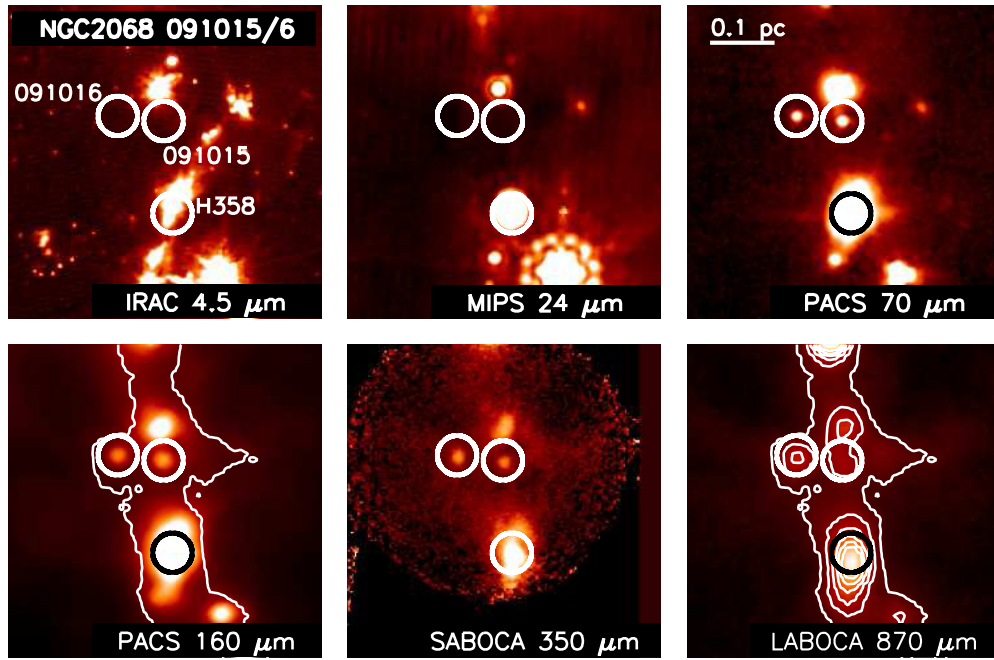
**Figure 7.** $4' \times 4'$ images of three PBR sources, 091015 and 091016 (top), and HOPS358 (bottom), at the indicated wavelengths, shown on a log scale. North is up and east is to the left. The circles indicate the location of the PACS 70 $\mu$m point sources. Contours indicate the 870 $\mu$m emission levels at $\{0.25, 0.5, 0.75, 1.0, 1.25\}$ Jy beam$^{-1}$. The lowest 870 $\mu$m contour is overplotted on the 160 $\mu$m image. No IRAC emission coincident with 091015 or 091016 is detected; however, these sources clearly reside in dense filamentary material traced by the sub-millimeter emission. The HOPS358 photometry is likely blended.

(A color version of this figure is available in the online journal.)
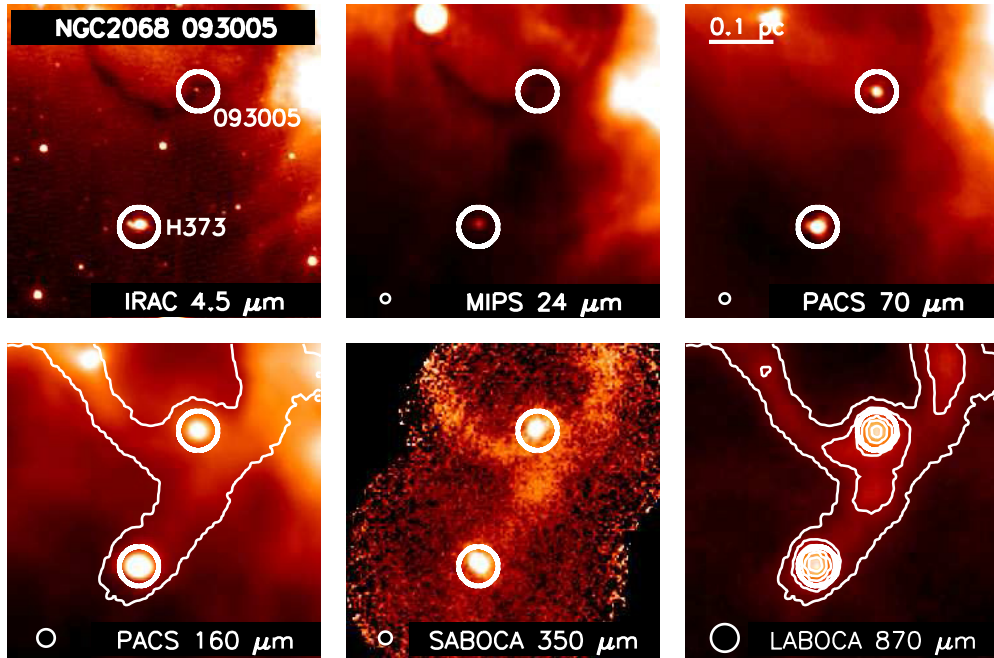


**Figure 8.** Same as Figure 7, showing $4' \times 4'$ images of two PBRs: 093005 (top) and HOPS373 (bottom). Contours indicate the 870 $\mu$m emission levels at $\{0.25, 0.5, 0.75, 1.0, 1.25, 1.5\}$ Jy beam$^{-1}$. Source 093005 is the reddest PBR shown in Figure 6 and lies at the intersection of three filaments traced by an 8 and 24 $\mu$m absorption feature and the 870 $\mu$m emission.

(A color version of this figure is available in the online journal.)

### 5.3. Spatial Distribution of the Three Samples

We show the locations of the *Herschel* protostar candidates compared to the locations of the HOPS sample in Figure 10; these positions are overlaid on the extinction map of Orion. It is immediately apparent that the spatial distribution of the new

candidate protostars and PBRs is non-uniform. To investigate this distribution further, we show the relative fraction of new sources as a function of individual region in Table 7. The overall number of new candidate protostars and PBRs is dominated by the Orion A cloud, and in particular L1641. This is not surprising since the L1641 region is quite large and contains
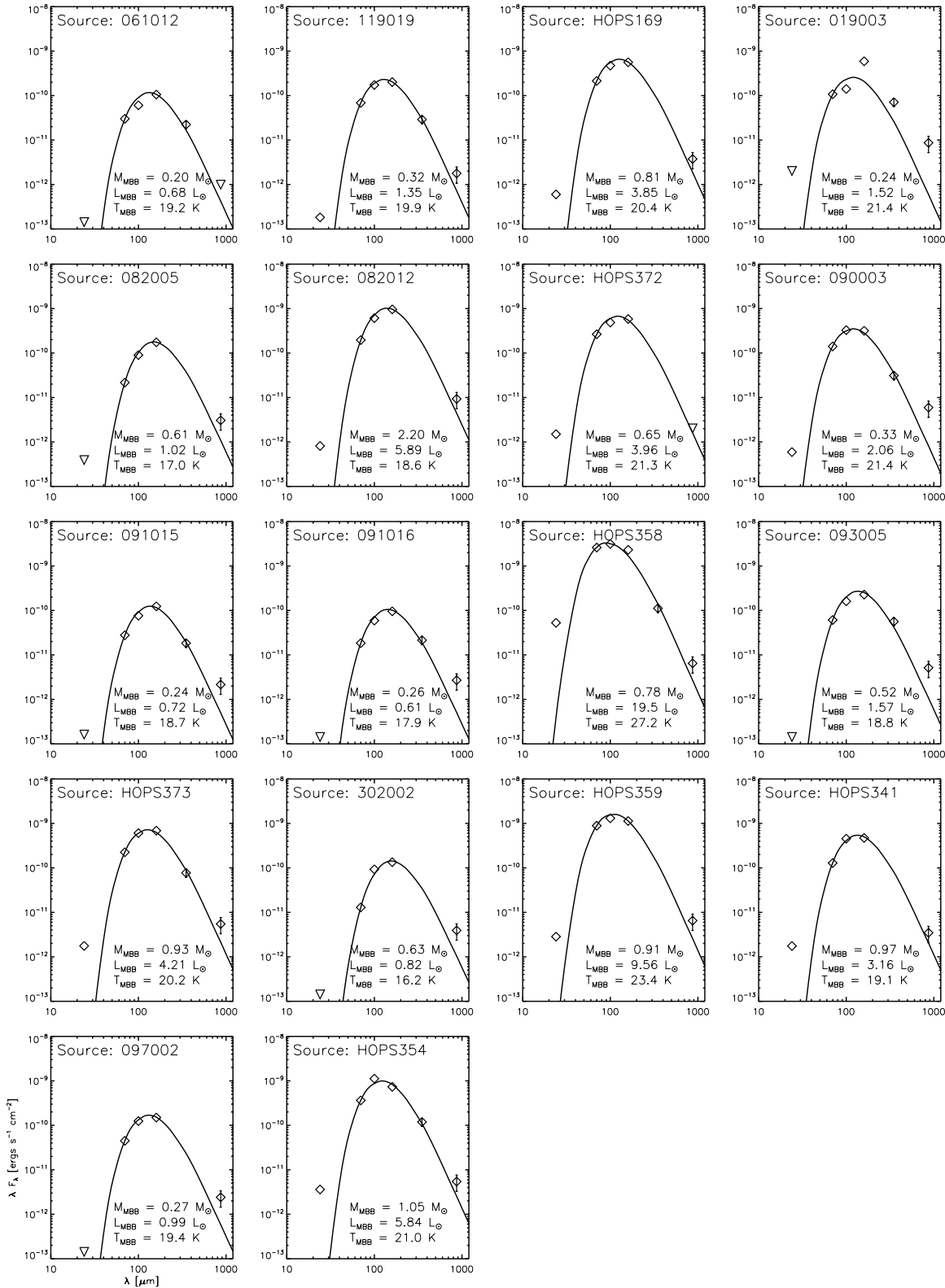
**Figure 9.** SEDs of the 18 PBRs are shown. The errors are smaller than the symbol size except for the 350 and 870 $\mu$m data points. The black curve shows the modified blackbody fit to the observed SED, with the indicated best-fit parameters (see Section 6.2). Note that PBR 019003 (shown in the top right) is located in a complex field where the photometry may be strongly contaminated.

more protostars compared to other Orion regions. The fractions of new candidate protostars and PBRs compared to the total number of HOPS and new candidate protostars is, however, two times larger in Orion B. This result is even more pronounced when we consider only the fractions of PBRs, with fractions that are more than 10 times larger in Orion B. The NGC 2068 (also containing the NGC 2071 nebula) and NGC 2024 (also containing the Horsehead or NGC 2023 nebula) fields in Orion B not only have the largest fraction of new candidate protostars, but also of PBRs. While these numbers and fractions are subject

**Table 6**
Orion PBRs Observed Properties: Detections, Environment, and Previous Detections

| Source | R.A. (h:m:s) | Decl. (°:′:″) | 4.5 $\mu$m Detection | High Incl.[a] | 24 $\mu$m Detection | Note[b] | Selected References |
|---|---|---|---|---|---|---|---|
| 061012 | 05:42:48.8 | −08:16:10.7 | Yes | . . . | No | ns | . . . |
| 119019 | 05:40:58.4 | −08:05:36.1 | Yes | . . . | Yes | f,i | . . . |
| HOPS169 | 05:36:36.0 | −06:38:54.0 | Yes | Yes | Yes | f,i | Le88, Mo91, Za97, Da00, St02, Jo06, Nu07, Ba09, Me12 |
| 019003 | 05:35:24.0 | −05:07:50.1 | Yes | . . . | No | f,c | Me90, Ch97, Ni03, Ts03, Nu07, Me12 |
| 082005 | 05:41:29.4 | −02:21:17.1 | No | . . . | No | f,i | La91, La96, Mo99, Jo06, Nu07 |
| HOPS372 | 05:41:26.3 | −02:18:21.1 | Yes | . . . | Yes | f,ns | La91, La96, Mo99, Jo06, Nu07, Me12 |
| 082012 | 05:41:24.9 | −02:18:08.5 | No | . . . | Yes | f,ns | La91, La96, Mo99, Wu04, Jo06, Nu07 |
| 090003 | 05:42:45.2 | −01:16:14.2 | Yes | . . . | Yes | i | Mi09 |
| HOPS358 | 05:46:07.2 | −00:13:30.9 | Yes | . . . | Yes | f,c | St86, Li99, Re99, Mi01, Wu04, Nu07, Me12 |
| 091015 | 05:46:07.7 | −00:12:19.1 | No | . . . | No | f,ns | Li99, Mi01, Nu07 |
| 091016 | 05:46:10.0 | −00:12:15.4 | No | . . . | No | f,ns | Li99, Mi01, Nu07 |
| HOPS373 | 05:46:30.7 | −00:02:36.8 | Yes | . . . | Yes | f,i | Ha83, La91, Gi00, Mo01, Mi01, Nu07, Me12 |
| 093005 | 05:46:27.7 | −00:00:51.5 | Yes | . . . | No | f,i | La91, Mo01, Mi01, Nu07 |
| 302002 | 05:46:28.2 | +00:19:28.4 | Yes | Yes | No | f,ns | La91, Jo01, Ph01, Mo01, Sa03, Nu07 |
| HOPS359 | 05:47:24.8 | +00:20:58.2 | No | . . . | Yes | f,i | La91, Mo01, Nu07, Me12 |
| HOPS341 | 05:47:00.9 | +00:26:20.8 | Yes | Yes | Yes | b | Jo01, Mo01, Nu07, Sa10, Me12 |
| 097002 | 05:48:07.7 | +00:33:52.7 | No | . . . | No | b/ns | . . . |
| HOPS354 | 05:54:24.2 | +01:44:20.1 | Yes | Yes | Yes | b | Re08, Ba09, Me12 |

**Notes.**

[a] Sources with indications of an observed high inclination orientation from the 4.5 $\mu$m images.

[b] ns = nearby source and indicates that we find a source close ($\lesssim 30''$) to the target; f = filament and indicates that a significant level of elongation or extended emission is seen in the 870 $\mu$m data; i = isolated and indicates that no nearby source is observed; c = crowded, indicating that the source resides in a region possibly with multiple sources, extended emission, or both and whose photometry may be affected by source blending; finally, b = binary, sources that may have an unresolved secondary source and therefore blended photometry.

**References.** (Le88) Levreault 1988; (Mo91) Morgan et al. 1991; (ZA97) Zavagno et al. 1997; (Da00) Davis et al. 2000; (St02) Stanke et al. 2002; (Da02) Davis et al. 2009; (Nu07) Nutter & Ward-Thompson 2007, Di Francesco et al. 2008; (Jo06) Johnstone & Bally 2006; (Ts03) Tsujimoto et al. 2003; (Ch97) Chini et al. 1997; (Ni03) Nielbock et al. 2003; (Me90) Mezger et al. 1990; (Mo99) Mookerjea et al. 2009; (La96) Launhardt et al. 1996; (La91) Lada et al. 1991a; (Wu04) Wu et al. 2004; (Mi09) Miettinen et al. 2009; (Re99) Reipurth et al. 1999; (St86) Strom et al. 1986; (Li99) Lis et al. 1999; (Mi01) Mitchell et al. 2001; (Mo01) Motte et al. 2001; (Gi00) Gibb & Little 2000; (Ha83) Haschick et al. 1983; (Ph01) Phillips et al. 2001; (Sa03) Savva et al. 2003; (Jo01) Johnstone et al. 2001; (Re08) Reipurth et al. 2008; (Ba09) Bally et al. 2009; (Sa10) Sadavoy et al. 2010; (Me12) Megeath et al. 2012.

**Table 7**
Numbers and Fractions of New Sources and Red PBRs Found by Region

| Region | Field | Total Number | New Number | New % | PBRs Number | PBRs % |
|---|---|---|---|---|---|---|
| All | | 355 | 56 | 16% | 18 | 5% |
| Orion A | | 274 | 35 | 13% | 4 | 1% |
| | L1641[a] | 200 | 31 | 16% | 3 | 2% |
| | ONC | 74 | 4 | 5% | 1 | 1% |
| Orion B | | 81 | 21 | 26% | 14 | 17% |
| | NGC 2024 | 17 | 3 | 18% | 4 | 24% |
| | NGC 2068 | 52 | 15 | 29% | 9 | 17% |
| | L1622 | 12 | 3 | 25% | 1 | 8% |

**Note.** [a] $\kappa$Ori sources have been included here.

to counting statistics and other possibly large sources of errors, the differences between Orion A and Orion B appear to be significant.

About 5% of the combined protostars and candidate protostars in Orion are PBRs. If we consider the PBRs as representing a distinct phase in the evolution of a protostar, and we assume a constant rate of star formation, this fraction suggests that the protostars spend 5% of their lifetime in the PBRs phase (approximately 25,000 years with the 0.5 Myr protostellar lifetime of Evans et al. 2009), averaging over all Orion regions. However, due to the spatial variations in the fractions of PBRs, the resulting duration of the PBR phase would vary greatly with location, from 5000 years in the Orion A cloud to 80,000 years

in the Orion B cloud. There are two alternative explanations for the large variations in percentage of PBRs. First, there might be environmental reasons which would favor the formations of PBRs, or perhaps extend the duration of the PBRs phase, in the Orion B cloud. Second, the ages of all the protostars in the Orion B cloud may be systematically younger than those in the Orion A cloud. In this case, the regions containing the PBRs in the Orion B could be undergoing very recent bursts of star formation.

Studies of pre-main-sequence stars in the Orion molecular clouds show little evidence for significant age differences between the Orion A and B clouds. Flaherty & Muzerolle (2008) determined an age of ∼2 Myr for NGC 2068 and NGC 2071, while Reggiani et al. (2011), Hsu et al. (2012), and Da Rio et al. (2012) determine ages for the ONC and L1641 of ∼2–3 Myr. However, most of the protostars associated with the NGC 2068 and NGC 2071 regions are outside the clusters of pre-main-sequence stars and in dense filaments and gas neighboring these clusters (Motte et al. 2001). A number of PBRs are in the LBS23 clump (directly south of NGC 2068) and in the NGC 2023 clump (in the NGC 2024 field); these are two of the five most massive, dense clumps found in Orion (Lada et al. 1991a). Compared to the other massive clumps, both of these regions have 1/10 the numbers of young stars per unit gas mass and hence may be quite young (Lada et al. 1991b; Lada 1992). The southern rim of the NGC 2068 nebula, LBS23, and the northern rim of the NGC 2071 nebula are rich in *Spitzer* identified protostars relative to more evolved pre-main sequence stars (see Megeath et al. 2012), further evidence that the areas rich in PBRs have a younger age.
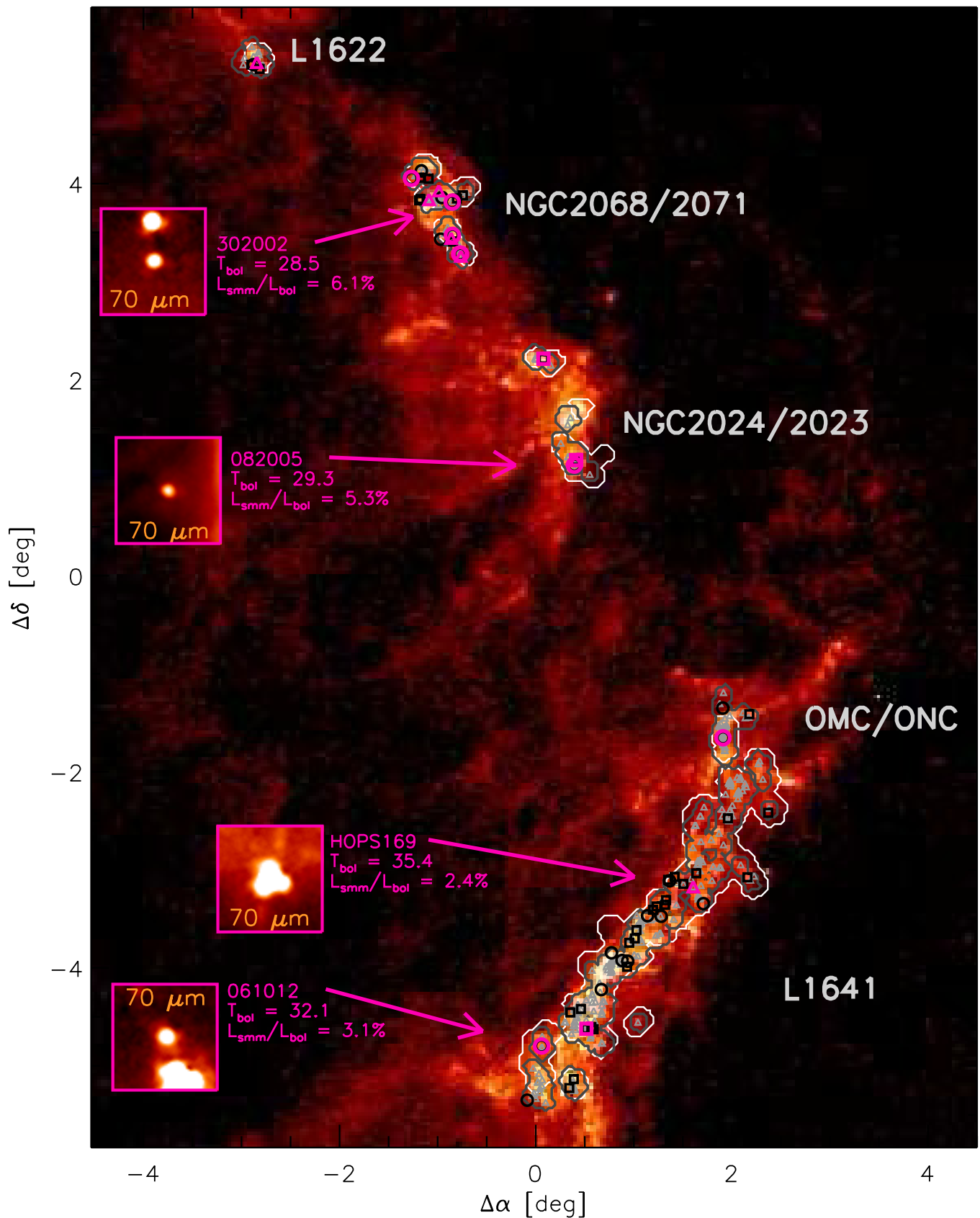
**Figure 10.** Distribution of red protostars overlaid on the extinction map of Orion. The dark gray contour shows the HOPS PACS coverage and the white contour shows the LABOCA 870 $\mu$m coverage. The triangles (light gray) indicate the positions of the HOPS protostars while the black points (squares and circles) indicate the positions of the new candidate protostars. The PBRs are highlighted in fuchsia and the properties of four selected PBRs are shown along with their corresponding $1' \times 1'$ HOPS 70 $\mu$m images. Orion B includes the prominent northern regions while Orion A includes the southern OMC/ONC and L1641 regions; note the large fractions of PBRs in NGC 2068/2071.

(A color version of this figure is available in the online journal.)

Alternatively, the gas in the LBS23 and NGC 2023 clumps have dense gas-filling factors that are much higher than the other massive clumps (Lada et al. 1997); hence, the protostars in these regions may be forming in a very different birth environment. We will investigate the roles of non-coevality and environment in determining the percentage of PBRs in future work.

## 6. DETERMINING THE PHYSICAL PROPERTIES OF PBRs THROUGH MODELS

In this section we describe our analysis of the physical properties of the PBRs as inferred from their colors and SEDs. We first compare the 70/24 colors of the PBRs sample with those derived from a grid of models that adopt the solution for a rotating envelope undergoing collapse (Ulrich 1976; Terebey et al. 1984) with outflow cavities along the rotation axis of the envelope (Whitney et al. 2003b). This analysis puts a constraint on the minimum inner density of the protostellar envelope. Next, we compare the observed SEDs to model SEDs generated using the Hyperion (Robitaille 2011) radiative transfer code. This set of models assumes radial power-law gradients consistent with either a collapsing core with a constant infall rate or a static isothermal core. The models also encompass various combinations of internal and external heating. Given the prohibitively large computational time needed to explore the full range of parameter space using radiative transfer models, and given our inability to distinguish between models purely from five to six photometry points, we do not provide individual model fits to each protostar. Instead, we fit a single-temperature modified blackbody function to the observed SEDs at 70 $\mu$m and longer wavelengths. The modified blackbody fits provide luminosities and an initial characterization of the envelope masses of the PBRs sample.

### 6.1. Axisymmetric Models: Interpreting the 70/24 Color

We begin our analysis by using a simplified version of the Ali et al. (2010) protostellar envelope model grid to predict observed fluxes and colors for comparison with our PBRs. The density distribution of these models is that of the collapse of a spherical cloud in uniform rotation (Ulrich 1976), which is the inner region of the Terebey et al. (1984) model of the collapse of the slowly rotating isothermal sphere. This model is then modified by the inclusion of outflow cavities of various shapes (Whitney et al. 2003a, 2003b). This schematic model envelope captures the dependence of the short wavelength (24 $\mu$m and 70 $\mu$m) fluxes on inclination due to rotation and bipolar cavities.

The model fluxes depend upon the mass infall rate, the angular momentum of the mass currently falling in, the outflow cavity properties, the inclination of the rotation axis to the line of sight (LOS), and the luminosity of the central source, as well as the assumed dust properties. The thermal emission of the dusty envelope does not depend directly on the mass infall rate but instead on the density of the envelope. The model assumes free-fall at a constant rate, which results in a density profile with shape $\rho \propto r^{-3/2}$ (Terebey et al. 1984). The overall scaling of the density is characterized by $\rho_1$, the density at 1 AU in the limit of no rotation:

$$\rho_1 = 7.4 \times 10^{-15} \left( \frac{\dot{M}_{\rm env}}{10^{-6} \, M_\odot \, {\rm yr}^{-1}} \right) \left( \frac{M_*}{0.5 \, M_\odot} \right)^{-1/2} \, {\rm g \, cm}^{-3}.$$

(1)

The envelope mass infall $\dot{M}_{\rm env}$ rate is related to $\rho_1$ via the free-fall velocity, which in turn depends upon the unknown central mass $M_*$. The actual model density structure departs from $r^{-3/2}$ on small scales because of the angular momentum of the infalling material. This enters into the model through the parameter $R_{\rm disk}$, the outer disk radius at which infalling material currently lands (see Ulrich 1976).

The rotation leads to a significant dependence of the SED on the inclination of the rotation axis relative to the LOS (Kenyon et al. 1993). This dependence is significantly enhanced by the inclusion of outflow cavities (Whitney et al. 2003b) which are assumed to be aligned along the rotation axis. Finally, the overall shape of the SED is only weakly affected by the luminosity of the central source ($L_*$; Kenyon et al. 1993) and so this is easily scaled.

To roughly compare observed PBRs' colors with those predicted by our model grid, in Figure 11 we show the effects of varying the model inclination, envelope density, and cavity opening angle on the 70/24 color and 70 $\mu$m flux. As stated above, these model tracks are based on a simplified version of the Ali et al. (2010) model grid; we refer the reader to that publication for details. In brief, the model tracks that we consider here have the same fixed parameters as those listed in Table 1 of Ali et al. (2010), including a fixed central mass of 0.5 $M_\odot$; in addition, we have fixed the cavity shape exponent to a value of $b = 1.5$, and the envelope outer radius to $R_{\rm env,max} = 1 \times 10^4$ AU. We have, however, expanded the envelope infall rate grid relative to the Ali et al. (2010) grid to larger values (up to $\dot{M}_{\rm env} = 10^{-3} \, M_\odot \, {\rm yr}^{-1}$ on a pseudo-logarithmic grid) and included a model with no envelope. As described above, for our model grid we assume that the envelope density falls off as $\rho(r) \propto r^{-3/2}$. Note that although our model grid is parameterized in terms of $\dot{M}_{\rm env}$, with a fixed central mass of $M_* = 0.5 \, M_\odot$, we will refer to $\rho_1$ throughout this section.

We note that the central masses of protostellar sources remain largely unconstrained observationally (however, see Tobin et al. 2012), and therefore may be lower than our assumed value. The effect of a lower central mass would be to lower $\dot{M}_{\rm env}$ for a given value of $\rho_1$. For example, if the central mass were 0.2 $M_\odot$, the infall rates reported for our models would be reduced by a factor of 0.6. The assumed central mass, however, does not change the value of $\rho_1$ corresponding to a given model SED. Furthermore, our small assumed disk radius does not strongly affect the trends shown here.

With this model grid we isolate the effects, albeit in a simplified fashion, of varying the model inclination (viewing angle to the protostar), envelope density ($\rho_1$), and cavity opening angle ($\theta_C$) on the 70 $\mu$m fluxes and 70/24 colors. In Figure 11, we show model tracks through 70 $\mu$m flux versus 70/24 color space for high inclination (87°) viewing angles as a function of both $\theta_C$ and envelope density ($\rho_1$). By analyzing only the high inclination models, we obtain a lower limit on the envelope density required to reproduce the red 70/24 colors.

We assume a fixed disk accretion rate of $\dot{M}_{\rm disk} = 1.0 \times 10^{-8} \, M_\odot \, {\rm yr}^{-1}$, a disk outer radius of $R_{\rm disk,max} = 5$ AU, and a central source luminosity of 1 $L_\odot$. Increasing $\dot{M}_{\rm disk}$ and $R_{\rm disk,max}$ drives the models to both bluer 70/24 colors and brighter 70 $\mu$m fluxes, while decreasing the inclination drives the models to bluer 70/24 colors. Therefore, we find that no model in our grid can explain 70/24 colors with envelope densities less than log $\rho_1/({\rm g \, cm}^{-3}) \sim -13.4$ (or equivalently an envelope infall rate of $\dot{M}_{\rm env} = 5.4 \times 10^{-6} \, M_\odot \, {\rm yr}^{-1}$). While models with larger values of $\rho_1$ and other combinations of parameters can be found for bluer 70/24 colors, this analysis sets an approximate lower limit on the expected envelope densities of sources with 70/24 > 1.65
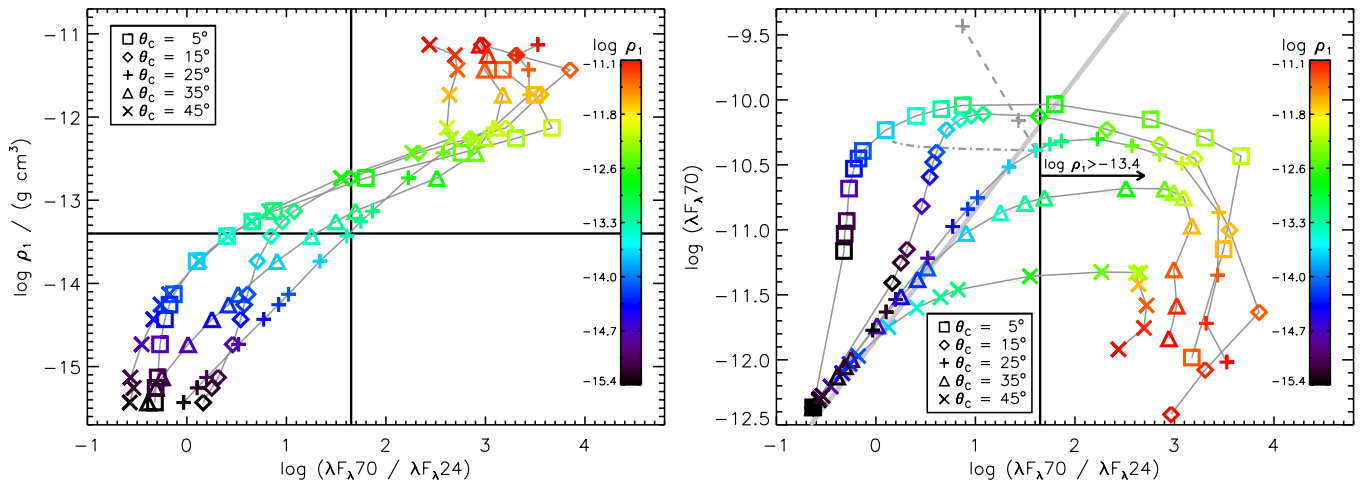
**Figure 11.** Left: dependence of the model 70 $\mu$m to 24 $\mu$m flux ratio for high inclination orientations (87°) on envelope density ($\rho_1$) for the five cavity opening angles in our grid. These model tracks assume an internal luminosity of 1.05 $L_\odot$. The 70/24 color selection is indicated with the vertical black line, while the corresponding log $\rho_1/(\mathrm{g\,cm^{-3}}) \sim -13.4$ (corresponding to an envelope infall rate of $\dot{M}_{env} = 7.5 \times 10^{-6}$) threshold is indicated with a horizontal black line. Right: model 70 $\mu$m flux vs. 70 $\mu$m to 24 $\mu$m flux ratio for high inclination orientations (87°). For the model with a cavity opening angle of $\theta_C = 25°$ (+ symbols) and log $\rho_1/(\mathrm{g\,cm^{-3}}) \sim -13.4$, we show the effect of increasing the internal luminosity by two orders of magnitude with the dashed gray curve, while the effect of decreasing the inclination to 18° is illustrated with the dot-dashed curve. All models with higher assumed values of luminosity and lower inclination will have envelopes that are denser than log $\rho_1/(\mathrm{g\,cm^{-3}}) \sim -13.4$, the median value of $\rho_1$ in our model grid; sources with redder 70 to 24 $\mu$m colors cannot be explained by envelopes that are less dense than this threshold. The thick light gray line corresponds to a 24 $\mu$m limit of 7 mag, the imposed *Spitzer* protostar magnitude limit for identification of protostars. (A color version of this figure is available in the online journal.)

of log $\rho_1/(\mathrm{g\,cm^{-3}}) \gtrsim -13.4$. That is, high source inclinations alone cannot explain the red 70/24 colors of the PBRs, which also require dense envelopes.

We expect that this value of $\rho_1$ should lie well within the Class 0 range; e.g., Furlan et al. (2008) found for a sample of 22 Class I sources in Taurus that log $\rho_1/(\mathrm{g\,cm^{-3}}) \leqslant -13.2$, while over half had $\rho_1$ values that are lower than log $\rho_1/(\mathrm{g\,cm^{-3}}) = -13.4$. Note that the Furlan et al. (2008) data set included far better sampling of the source SEDs and, most critically, *Spitzer* IRS spectroscopy, allowing for a more robust estimate of the parameters of sources in their sample. In contrast, our SEDs generally are envelope dominated with few sources having robust detections shortward of 24 $\mu$m. Therefore, any estimate of the value of the envelope density will be necessarily imprecise and have a back of the envelope character. That said, our comparison with the model grid and previous derived values of the envelope density leads us to conclude that the 70/24 > 1.65 color cut, while not uniformly selecting a unique envelope density threshold, will preferentially select Class 0 sources with log $\rho_1/(\mathrm{g\,cm^{-3}}) \gtrsim -13.4$, irrespective of source inclination.

Having demonstrated that the very red 70/24 colors require large values of $\rho_1$, as expected for SEDs peaking at long wavelengths, we proceed by analyzing the PBRs in the context of more simplified models. In what follows, we carry out two independent analyses of the source SEDs: a qualitative model image comparison using 1D models generated with the Hyperion (Robitaille 2011) radiative transfer code, and modified blackbody fitting to the observed SEDs at 70 $\mu$m and longer wavelengths. We attempt to maintain consistency by using similar envelope dust models throughout the analysis presented here. For the Hyperion model image analysis we use the Ormel et al. (2011) opacities. These opacities are similar to the commonly assumed Ossenkopf & Henning (1994, "OH5"; see below) opacities but include both the scattering and absorption components at short wavelengths, needed for radiative transfer calculations. Specifically, we use the "icsgra2" Ormel et al.

(2011) model opacities, which include icy silicates and bare graphites, with a coagulation time of 0.1 Myr. We assume the dust model from Ossenkopf & Henning (1994) for the long-wavelength-modified blackbody fits, specifically, their "OH5" opacities, corresponding to Column 5 of their Table 1. These opacities reflect grains having thin ice mantles with $10^5$ years of coagulation time at an assumed gas density of $10^6$ cm$^{-3}$.

### 6.2. Spherically Symmetric Models: Comparison to Photometry Derived from Model Images

We use the Hyperion (Robitaille 2011) Monte Carlo radiative transfer code to investigate some basic properties of the PBRs. We run a series of spherically symmetric models under a range of very simple assumptions, and produce simulated images. As stated above, the dust model we assume is that of Ormel et al. (2011, "icsgra2"). To explore which model assumptions might be reasonable for analyzing the properties of the reddest sources in Orion, we investigate a few limiting model scenarios. We therefore disregard the details of the individual source SEDs of the entire red sample and qualitatively compare the SEDs of the two sources with the smallest and largest values of $L_{bol}$ and $T_{bol}$ (sources 091016 and HOPS358, respectively; see Table 8) with photometry derived from model images.

We generate a series of model images that fall into four classes: (1) a starless core at a constant temperature of 10 K (referred to here as the "core" model); (2) a starless core with an isotropic external radiation field ("core+external"); (3) a core with an internal source ("star" model); and finally (4) a core with both an internal source and an isotropic external radiation field ("star+external"). For each of these classes of models, we test a range of density profile shapes and density normalizations. For the density profile shape we assume two values, $\alpha = 1.5, 2.0$, where $\alpha$ is the radial density profile power-law index: $\rho(r) \propto r^{-\alpha}$. For the absolute value of the (gas) density normalization at 1 AU we assume five values, log $(\rho_{1\,AU}/(\mathrm{g\,cm^{-3}})) = -10$ to $-14$, in steps of $\delta$ log $(\rho_{1\,AU}/(\mathrm{g\,cm^{-3}})) = 1.0$. For models

**Table 8**
Orion PBRs and Comparison Class 0 Sources: Observed Properties and Modified Blackbody Fit Parameters

| Source | $T_{\rm bol}$ (K) | $L_{\rm bol}$ ($L_\odot$) | $L_{\rm smm}/L_{\rm bol}$[a] (%) | $T_{\rm MBB}$[b] (K) | $L_{\rm MBB}$[b] ($L_\odot$) | $M_{\rm MBB}$[b, c] ($M_\odot$) | $\lambda_{\rm peak, MBB}$[b] ($\mu$m) |
|---|---|---|---|---|---|---|---|
| 061012[d] | 32.1 ± 0.9 | 0.75 ± 0.06 | 3.1 | 19.2 ± 0.4 | 0.68 ± 0.07 | 0.20 ± 0.04 | 133 |
| 119019 | 34.4 ± 0.9 | 1.56 ± 0.14 | 2.6 | 19.9 ± 0.4 | 1.35 ± 0.11 | 0.32 ± 0.06 | 127 |
| HOPS169 | 35.4 ± 0.9 | 4.50 ± 0.42 | 2.4 | 20.4 ± 0.5 | 3.85 ± 0.41 | 0.81 ± 0.20 | 127 |
| 019003[d] | 33.6 ± 1.1 | 3.16 ± 0.29 | 1.1 | 21.4 ± 0.8 | 1.52 ± 0.30 | 0.24 ± 0.18 | 121 |
| 082005[d] | 29.3 ± 0.8 | 1.02 ± 0.11 | 5.4 | 17.0 ± 0.4 | 1.02 ± 0.13 | 0.61 ± 0.15 | 151 |
| HOPS372 | 36.9 ± 1.0 | 4.90 ± 0.45 | 1.9 | 21.3 ± 0.6 | 3.96 ± 0.43 | 0.65 ± 0.17 | 121 |
| 082012 | 32.2 ± 0.9 | 6.27 ± 0.65 | 3.8 | 18.6 ± 0.4 | 5.89 ± 0.71 | 2.20 ± 0.52 | 139 |
| 090003 | 36.0 ± 0.8 | 2.71 ± 0.24 | 1.8 | 21.4 ± 0.4 | 2.06 ± 0.15 | 0.33 ± 0.06 | 121 |
| HOPS358 | 44.3 ± 0.9 | 30.6 ± 2.21 | 0.6 | 27.2 ± 1.0 | 19.5 ± 1.23 | 0.78 ± 0.14 | 88. |
| 091015[d] | 30.9 ± 0.9 | 0.81 ± 0.07 | 3.3 | 18.7 ± 0.4 | 0.72 ± 0.06 | 0.24 ± 0.04 | 136 |
| 091016[d] | 29.1 ± 0.9 | 0.65 ± 0.06 | 4.1 | 17.9 ± 0.3 | 0.61 ± 0.06 | 0.26 ± 0.05 | 142 |
| HOPS373 | 36.0 ± 0.9 | 5.20 ± 0.48 | 2.3 | 20.2 ± 0.4 | 4.21 ± 0.32 | 0.93 ± 0.16 | 127 |
| 093005[d] | 30.8 ± 0.9 | 1.71 ± 0.15 | 3.4 | 18.8 ± 0.4 | 1.57 ± 0.15 | 0.52 ± 0.10 | 136 |
| 302002[d] | 28.6 ± 0.9 | 0.84 ± 0.10 | 6.1 | 16.2 ± 0.3 | 0.82 ± 0.11 | 0.63 ± 0.15 | 157 |
| HOPS359 | 39.3 ± 0.9 | 12.6 ± 1.00 | 1.3 | 23.4 ± 0.7 | 9.56 ± 0.84 | 0.91 ± 0.23 | 115 |
| HOPS341 | 36.3 ± 1.1 | 3.62 ± 0.37 | 3.1 | 19.1 ± 0.5 | 3.16 ± 0.35 | 0.97 ± 0.24 | 133 |
| 097002[d] | 33.4 ± 0.9 | 1.14 ± 0.11 | 2.8 | 19.4 ± 0.5 | 0.99 ± 0.11 | 0.27 ± 0.07 | 130 |
| HOPS354 | 37.4 ± 0.8 | 7.53 ± 0.74 | 1.9 | 21.0 ± 0.4 | 5.84 ± 0.45 | 1.05 ± 0.19 | 124 |
| B 335[e] | 40.3 ± 1.3 | 0.55 ± 0.04 | 2.6 | 20.0 ± 0.7 | 0.47 ± 0.04 | 0.11 ± 0.02 | 130 |
| CB 130[e] | 55.2 ± 3.3 | 0.22 ± 0.01 | 10.9 | 12.7 ± 0.5 | 0.17 ± 0.01 | 0.55 ± 0.11 | 199 |
| CB 244–SMM1[e] | 63.2 ± 2.6 | 1.72 ± 0.14 | 1.8 | 20.3 ± 0.8 | 1.10 ± 0.11 | 0.24 ± 0.04 | 127 |
| CB 68[e] | 49.2 ± 1.4 | 0.68 ± 0.06 | 1.9 | 19.8 ± 1.1 | 0.42 ± 0.05 | 0.10 ± 0.02 | 130 |
| VLA1623-243[f] | 34.0 ± 1.2 | 2.82 ± 0.32 | 2.4 | 21.3 ± 0.5 | 2.55 ± 0.24 | 0.48 ± 0.09 | 124 |

**Notes.**
[a] Our $L_{\rm smm}/L_{\rm bol}$ may be underestimated as the $L_{\rm smm}$ values are measured from the modified blackbody fits to the SEDs (see the text).
[b] Best-fit modified blackbody parameters; the parameters shown here are derived from fitting the $\lambda \geqslant 70$ $\mu$m SED points. Excluding the 70 $\mu$m point and fitting only the $\lambda \geqslant 100$ $\mu$m points systematically increases the derived masses by 20% on average, decreases the temperature by 5% on average, and decreases the luminosity by 7% on average.
[c] The masses derived here will increase by a factor of ∼4 if we assume an ISM-type dust model (Draine & Lee 1984). Furthermore, we assume a gas-to-dust ratio of 110 (see the text).
[d] The values of $T_{\rm bol}$ and $L_{\rm bol}$ for these sources should be considered upper limits because we include the 24 $\mu$m upper limits in our analysis for these sources.
[e] Additional well-studied isolated Class 0 sources from Launhardt et al. (2013) and Stutz et al. (2010) are shown for comparison; the distances to these sources lie between 100 pc and 250 pc.
[f] SED from J. Green and DIGIT team (2012, private communication) and J. Green et al. (in preparation).

with external heating, the bolometric strength of the interstellar radiation field (ISRF) is set to the value from Mathis et al. (1983) at the solar neighborhood ($4\pi J_\nu = 0.0217$ erg cm$^{-2}$ s$^{-1}$). The spectrum of the radiation field is assumed to be that at the solar neighborhood from Porter & Strong (2005), but reddened by $A_V = 10$ using the Kim et al. (1994) extinction law. The ISRF model includes contributions from the stellar, PAH, and FIR thermal emission. The inner radius of the core is set to the radius at which the dust sublimates, assuming a sublimation temperature of 1600 K, while the outer radius is set to 1 pc. The central source is taken to have 10 $L_\odot$ and a spectrum given by a Planck function at the effective temperature of the Sun (5778 K). The choice of the stellar temperature is arbitrary, and is unimportant for the modeling presented here, since all sources are deeply embedded and all stellar radiation is reprocessed—only the total bolometric luminosity is important (see, e.g., Johnston et al. 2012, for a discussion of the $R_{\rm star}$ and $T_{\rm star}$ degeneracy).

The high levels of spatial filtering caused by our adopted aperture photometry scheme require us to assume such a central source luminosity to roughly match the flux levels in the observed SEDs. Furthermore, while a 1 pc sized envelope is larger than usually assumed, the high levels of spatial filtering inherent in the aperture photometry cause us to be insensitive to structure on scales larger than the assumed aperture sizes.

The model images have a resolution of 1″ pixel$^{-1}$, or 420 AU at our assumed distance. We convolve these images with the azimuthally averaged PSFs provided by Aniano et al. (2011), except in the case of the SABOCA 350 $\mu$m and LABOCA 870 $\mu$m images. These wavelengths are convolved with Gaussian PSFs with FWHMs equal to 7″4 and 19″, respectively, i.e., the nominal beam sizes for our observations. All model image photometry is then performed on the convolved model images using the same aperture and sky annulus parameters as those applied to the data. The use of such photometric aperture parameters can cause substantial spatial filtering due to the small sizes of the apertures relative to the beam sizes and the extent of the core emission (see below).

We show our extracted model SEDs in Figure 12 and a subset of the corresponding model images in Figure 13. In general, we find that models without internal sources are very unlikely to match the observed PBRs properties, on the basis that their SEDs are less luminous and peak at longer wavelengths than the observed SEDs for all density profile shapes that we assume; see Figure 12, top panels. While the "core+external" models (top right panel) suffer from severe spatial filtering, it is unlikely that such models will well represent the data as these SEDs tend to also peak at longer wavelengths. For the two classes of models with internal sources we find better agreement with the data; see lower panels of Figure 12. While steeper envelope profiles
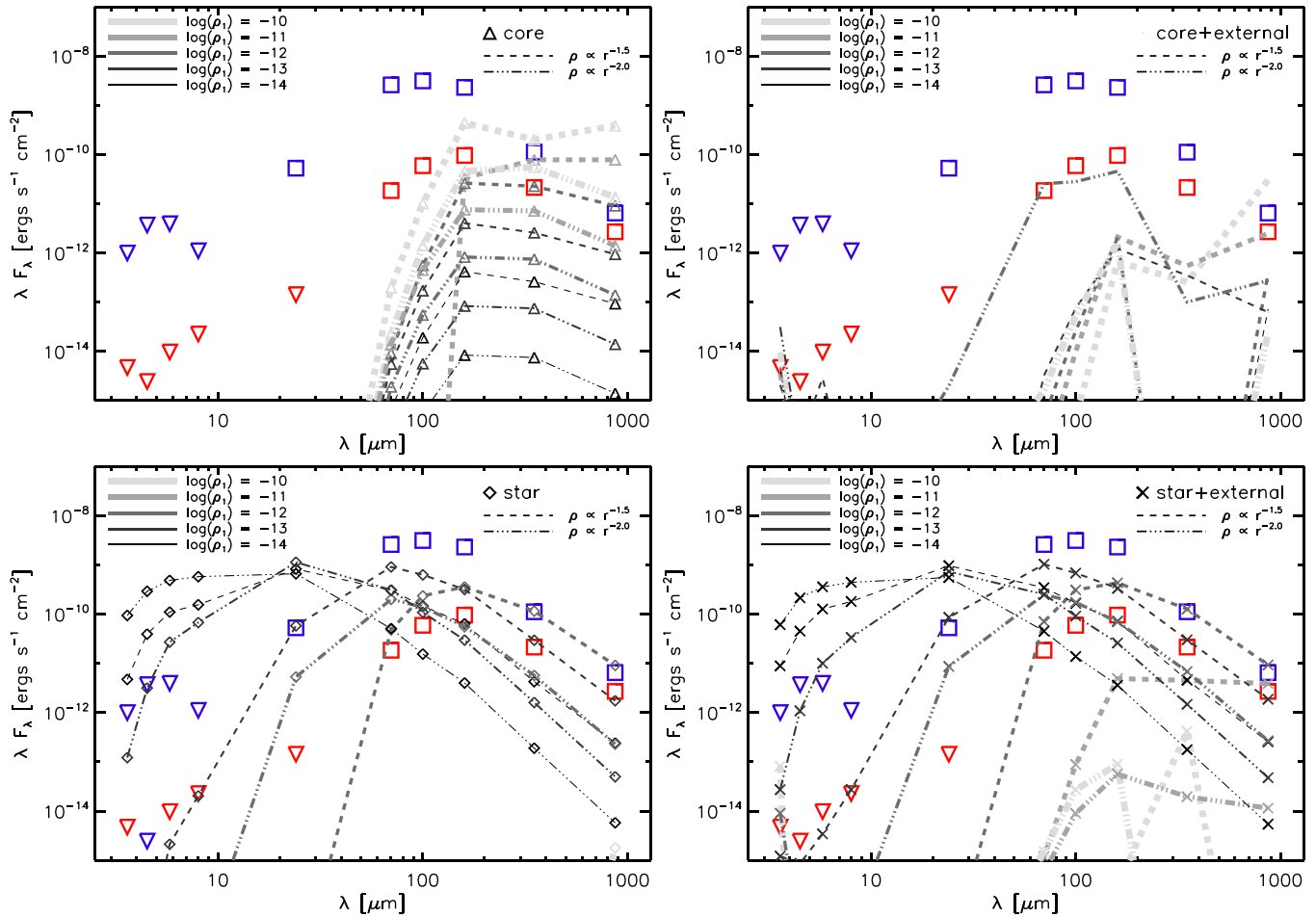
**Figure 12.** All panels show the SEDs of HOPS358 (blue: $L_{bol} = 30.6$ $L_{\odot}$ and $T_{bol} = 44.2$ K) and 091016 (red: $L_{bol} = 0.65$ and $T_{bol} = 29$ K), the extrema of the $L_{bol}$ and $T_{bol}$ distributions for the reddest sources, compared to spherical models. The two line styles indicate the different assumptions for the density profile shape while the shade of gray indicates the different model density $\rho_1$ values. The four panels correspond to the four different models that we test (see the text)—top left: the "core" model, a starless core; top right: the "core+external" model, a starless core with external heating; bottom left: the "star" model, a core with an internal source; and finally, bottom right: the "star+external" model, consisting of a core with an internal source that is irradiated by an external radiation field. Severe spatial filtering due to our aperture photometry on the model images can be seen most notably in the two externally heated models (left column).

(A color version of this figure is available in the online journal.)
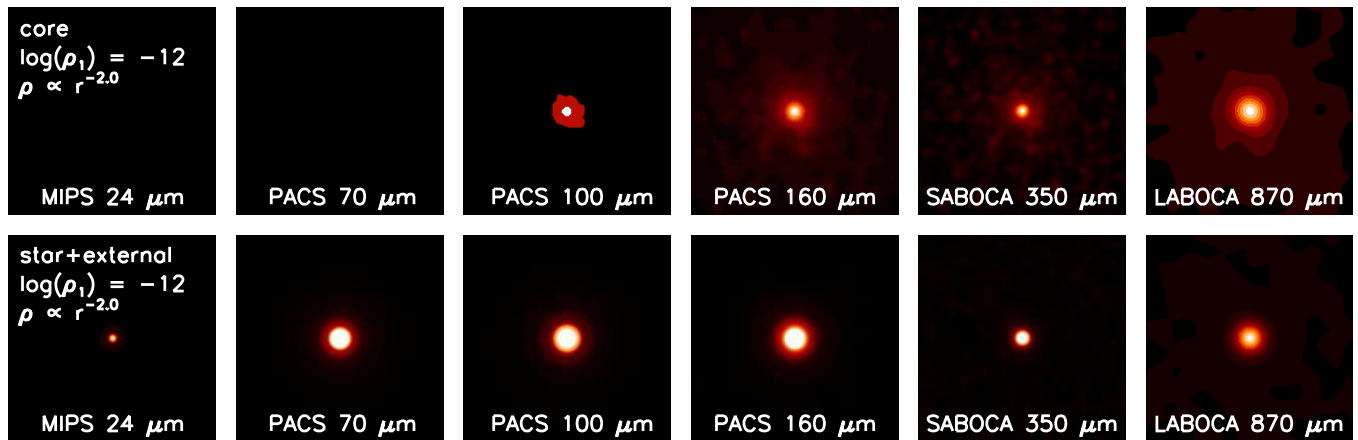


**Figure 13.** Convolved model images at the indicated wavelengths, shown on a log scale with the same minimum and maximum flux levels for all panels to illustrate the shape of the model SEDs. Each image is $200''$ (or 84,000 AU) on a side. The top row shows the "core" model images, with $\log(\rho_1) = -12$ and a density profile shape of $\rho \propto r^{-2.0}$, corresponding to the top left panel in Figure 12. The bottom row shows the "star+external" model, with the same density parameters as the top row, corresponding to the bottom right panel in Figure 12.

(A color version of this figure is available in the online journal.)

20

may imply somewhat higher envelope densities, the range in plausible densities for $\alpha = 1.5$ is $\log \rho_1 \sim -12$ to $-13$, while for $\alpha = 2.0$ values of $\log \rho_1 \sim -12$ roughly agree with the shapes of the observed SEDs. We note that we find very little difference between the "star+external" and the "star" model in the $\lambda \lesssim 160\ \mu$m regime, possibly indicating that our assumed ISRF strength relative to the assumed internal source luminosity may be underestimated compared to what we might expect to find regions like Orion.

### 6.3. Modified Blackbody Fits to the PBRs

An individual detailed fit to each protostar is beyond the scope of this work considering the vast amount of parameter space needed to model protostellar SEDs (i.e., source luminosity, envelope density, envelope rotation, outflow cavity geometry, external heating, outer envelope structure). Furthermore, unlike most of the HOPS protostars, whose properties can be constrained from a combination of far-IR photometry, 5 $\mu$m to 40 $\mu$m *Spitzer*/IRS spectra, and Hubble near-IR imaging (Fischer et al. 2010, 2012), the properties of the SEDs must currently be derived from five to six photometry points at long wavelengths. While the above modeling and analysis shows that the internal source is important, the longer wavelength fluxes are probing the bulk of the envelope mass, expected to mostly be at a single temperature. Furthermore, for density profiles in the range of $\rho(r) \propto r^{-3/2}$ or $r^{-2}$, as assumed above, we expect that most of the envelope will be located at large radii. We therefore perform modified blackbody fits to the $\lambda \geqslant 70\ \mu$m SEDs listed in Tables 4 and 5. For this analysis, we use the beam flux measurements for the sub-millimeter 350 $\mu$m and 870 $\mu$m portion of the SED. The results of the analysis are presented in Table 8 and the model SEDs are plotted with the data in Figure 9.

Before fitting the long-wavelength SEDs of the sources, we apply color corrections to the *Herschel* 70 $\mu$m, 100 $\mu$m, and 160 $\mu$m fluxes. Following Launhardt et al. (2013), these photometric color corrections have been derived iteratively from the slopes of the PACS SEDs, using polynomial fits to the values in Table 2 of the PACS calibration release note "PACS Photometer Passbands and Colour Correction Factors for Various Source SEDs" from 2011 April 12. The color corrections for the APEX data are assumed to be negligible.

The form of the modified blackbody function is given by

$$S_\nu = \Omega\, B_\nu(\nu, T_{\rm d})\,(1 - e^{-\tau(\nu)}), \qquad (2)$$

where $\Omega$ is the solid angle of the emitting element, $B_\nu(T_{\rm d})$ is the Planck function at a dust temperature $T_{\rm d}$, and $\tau(\nu)$ is the optical depth at frequency $\nu$. Here, the optical depth is given by $\tau(\nu) = N_{\rm H}\, m_{\rm H}\, R_{\rm gd}^{-1}\, \kappa(\nu)$, where $N_{\rm H} = 2 \times N({\rm H_2}) + N({\rm H})$ is the total hydrogen column density, $m_{\rm H}$ in the proton mass, $\kappa_\nu$ is the assumed dust opacity law from Ossenkopf & Henning (1994), and $R_{\rm gd}$ is the gas-to-dust ratio, assumed to be 110 (Sodroski et al. 1997). The best-fit total masses $M_{\rm tot}$ reported in Table 8 have been multiplied by an additional factor of 1.36 to account for helium and metals. Furthermore, in Table 8 we also report the peak wavelength of the best-fit modified blackbody model. Finally, we estimate $L_{\rm smm}$ from the model SED, where $L_{\rm smm}$ is integrated over $\lambda \geqslant 350\ \mu$m.

If a given source SED has coverage over fewer than four long-wavelength points, we do not fit a model to the SED. While all the PBRs' sources satisfy this criterion, all the new candidate protostars and HOPS sources do not (see Section 5.2) and are

therefore not fitted. The errors on $T_{\rm d}$, $M_{\rm tot}$, and the thermal component of the luminosity ($L_{\rm MBB}$) are estimated through a straightforward Monte Carlo method.[14] For each source we generate 2000 synthetic SEDs drawn from a normal density with mean and standard deviation equal to those of the measured SED at each wavelength. We then fit each synthetic SED. The reported error is equal to the standard deviation of the resulting distribution of each parameter. These errors do not include systematics introduced by, e.g., our dust model assumption or variation in the gas-to-dust ratio.

We show the modified blackbody fit results, along with the SEDs of the PBRs, in Figure 9. The resulting best-fit mass, luminosity, and temperature is also indicated for each source. The model fits the data surprising well considering that significant temperature gradients in the envelope are expected. Furthermore, in all cases, the 24 $\mu$m point, when detected, has a much higher flux level than the modified blackbody model. We interpret this discrepancy as strong evidence for internal heating by a protostar.

Excluding the 70 $\mu$m point and fitting only the $\lambda \geqslant 100\ \mu$m SED has a minor effect on the resulting parameter values. Without 70 $\mu$m, the masses systematically increase by 40%, the temperatures decrease by 5%, and the luminosities decrease by 7%. This small effect may be understood by the fact that the 100 $\mu$m fluxes are well correlated with the 70 $\mu$m fluxes for this sample, tracing similar material near the protostars. The dust temperatures probed at 100 $\mu$m and 70 $\mu$m are not dramatically different since the $\tau = 2/3$ surfaces are not extremely different between the two wavelengths. From Hartmann (2009), the radius of the $\tau = 2/3$ surface can be roughly approximated as $r_\lambda \propto \kappa_\lambda^2$; this relation implies that the radii of the $\tau = 2/3$ surfaces for the two wavelengths is $r_{70}/r_{100} \sim 2.5$.

Our best-fit modified blackbody model always underestimates the observed 870 $\mu$m flux of all sources. The model sub-millimeter SEDs are always bluer than the observed SEDs. We find that the discrepancy is at the $0.83 \pm 0.26$ Jy level (or a factor of $\sim 3$ excess), where the error bar represents the standard deviation in the residual distribution. It is likely that this discrepancy is dominated by the larger beam size of the 870 $\mu$m observations which has the effect of mixing the source flux with that of the surrounding cold and possibly high-column environment. Contamination to the 870 $\mu$m flux by disk emission may also increase this discrepancy. Jørgensen et al. (2009) find average disk masses of $\sim 0.13\ M_\odot$ (with a large scatter) across their sample of Class 0 sources. The sources in their sample that are comparable to our PBRs, however, are those with the lowest values of $T_{\rm bol}$. For reference, they found that IRAS4A1, with a $T_{\rm bol} = 43$ K, has the largest disk mass of $0.46\ M_\odot$ in their sample; on the other hand, L1157, with a similar $T_{\rm bol} = 42$ K, has a disk mass about a factor of four smaller. We estimate that a 30 K disk of $0.5\ M_\odot$ would contribute $\sim 0.6$ Jy to the beam flux at 870 $\mu$m (assuming Ossenkopf & Henning 1994 dust opacities, as above). Therefore, disk emission could indeed contribute to the observed 870 $\mu$m flux but further detailed observations at high resolution are needed to disentangle the envelope component from the possible disk emission. However, we do not find an 870 $\mu$m discrepancy in the analysis of model images presented in the previous section. This indicates that large disk masses may not be necessary to explain the sub-millimeter fluxes. We

---

[14] "Offered the choice between mastery of a five-foot shelf of analytical statistics books and middling ability at performing statistical Monte Carlo simulations, we would surely choose to have the latter skill." Press et al. (1992, Numerical Recipes, p. 686).

therefore emphasize that the disk masses inferred here from the 870 $\mu$m excess should be regarded only as upper limits; further detailed investigation into the disk properties of our sources is deferred to future work.

Independent of these issues, it is clear that a more accurate treatment of the data would require all images to be convolved to a matched resolution; however, this approach would have the effect of causing non-detections for a majority of sources at the shorter wavelengths due to the relatively large limiting beam size of our data set ($\sim$19″ at 870 $\mu$m). Homogeneously extracted SEDs are therefore not feasible for this data set as a whole. Nevertheless, we test the effects of convolving the data before extracting the SEDs. We choose PBR 119019 as a test source because it is isolated and has approximately median values for the best-fit modified blackbody temperature, luminosity, and mass. Ignoring the 870 $\mu$m data, this source is clearly detected at 70 $\mu$m, 100 $\mu$m, 160 $\mu$m, and 350 $\mu$m. For these four wavelengths, the largest beam size of $\sim$12″ corresponds to the 160 $\mu$m data. We therefore convolve the 70 $\mu$m, 100 $\mu$m, and 350 $\mu$m data to a resolution matching the 160 $\mu$m observations and extract a beam-smoothed SED. We then fit this SED in the same way as described above. Compared to the non-convolved SED modified blackbody fitting results, we find that the temperature decreases by $\sim$4%, the luminosity increases by $\sim$10%, and the mass in the thermal component increases by $\sim$30%. These systematic shifts are similar to but somewhat larger than the errors quoted in Table 8 ($\sim$2% on the temperature, $\sim$10% on the luminosity, and $\sim$30% on the mass). We note, however, that the errors quoted in Table 8 are purely random and do not include any systematic component. We therefore conclude that extracting SEDs from images matched to a resolution of $\sim$12″ would not greatly affect our results.

Modified blackbody fits provide a somewhat limited means of analysis of our sources since the model assumes a single temperature and density along the LOS for the emitting material. We expect that the assumption of a single LOS temperature will cause an underestimate of the source masses (e.g., Niel-bock et al. 2012; Launhardt et al. 2013). However, radiative transfer models have large ambiguities in the assumed source temperature and density structure, leading to mass estimates that are strongly model-dependent. Furthermore, the dust law that is assumed will introduce significant uncertainties into the derived masses, irrespective of the analysis method that is implemented. For example, the masses listed in Table 8 increase by a factor of $\sim$4 on average when we assume Draine & Lee (1984) $R_V = 3.1$ interstellar medium (ISM) like dust. These issues indicate that the masses derived here represent lower limits to the true envelope masses. Nevertheless, we consider the modified blackbody fits to the measured photometry to provide the most robust estimates of the mass that we currently have.

We note that with only five SED flux points at best, fitting a multiple component (modified) blackbody model cannot be justified. Since most of the mass is located at relatively large scales and expected to have cold temperatures, excluding the warmer shorter wavelength data arising from inner material will not significantly increase the masses we derive. The modified blackbody fits thus provide an approximate measurement of the optical-depth-averaged gross properties of the envelopes being investigated. These issues point to the need for a more sophisticated modeling approach that will be carried out in future work.

# 7. DISCUSSION

As seen in Figure 11, the observed 70/24 colors of a protostar can be driven toward redder values through various strongly degenerate parameters. For example, the total column of material along the LOS toward a given protostar can have multiple contributions: the attenuation of the mid-IR emission by dense foreground material, the density of the envelope, the amount of envelope flattening, the opening angle of the outflow cavity, and the source inclination. Furthermore, the assumed model central protostar mass remains largely unconstrained by observations to date and can affect the interpretation of the 70/24 colors.

Foreground extinction can have various contributions, such as intervening dust between the observer and the cloud and dense material associated with the cloud itself, such as filamentary material. Of these two components, the first is expected to be relatively small, while the latter can be expected to vary from source to source by relatively large amounts, with a corresponding effect on the observed colors. For example, some PBRs are located in filamentary regions (e.g., Figures 7 and 8), while others appear more isolated (e.g., see Appendix B for Figure 20). We have estimated the effects of foreground extinction levels up to a level of $A_V = 40$ mag, and find that the values of $L_{bol}$, $L_{smm}$, and $T_{bol}$ are not significantly affected.

On the other hand, the effects of source inclination are not as straightforward to assess. When considering the presence of flattened rotating envelopes, disks, and outflow cavities, the source inclination will have a large effect on the observed source SED, as illustrated by the model tracks shown in Figure 11 (see also, e.g., Whitney et al. 2003b; De Buizer et al. 2005; Offner et al. 2012).

Therefore, it appears that the very red PBRs can be explained by multiple effects that all result in increasingly red observed 70/24 colors. These very red colors may be driven by elevated envelope densities (or equivalently, $\dot{M}_{env}$), high source inclinations, or elevated levels of extinction associated with structures larger than the envelope–protostar system. The current data and SED coverage do not allow us to break these degeneracies conclusively. Furthermore, we consider it likely that the red observed colors are not driven by any single cause, but instead are the result of several causes.

We have, however, designed our PBR selection to find the densest envelopes in Orion (cf. Figure 11). Furthermore, the effect of external foreground extinction is not expected to be large at these long wavelengths, even with elevated levels of material along the LOS (see above). Indeed, we have also shown that the PBRs require a central heating source, indicating that the detection of a 70 $\mu$m point source drives the interpretation of the sample as Class 0 sources, irrespective of source inclination. However, we note that if the central masses are significantly different than the assumed value of 0.5 $M_\odot$, then for a fixed reference envelope density the inferred envelope infall rates need to be scaled accordingly (see Equation (1)).

To further investigate the evolutionary state of the PBRs, in Figure 14 we show the values of $L_{bol}$, $T_{bol}$, and $L_{smm}/L_{bol}$ for the entire sample of new candidate protostars and the previously identified *Spitzer* HOPS sample (W. J. Fischer et al., in preparation). In the left panel, we show $L_{bol}$ versus $T_{bol}$ for the entire sample of new protostar candidates, including those flagged as possible extragalactic contamination. We also show the four reference Class 0 sources presented in Table 8. The PBRs' sample, in particular, and the entire sample of new
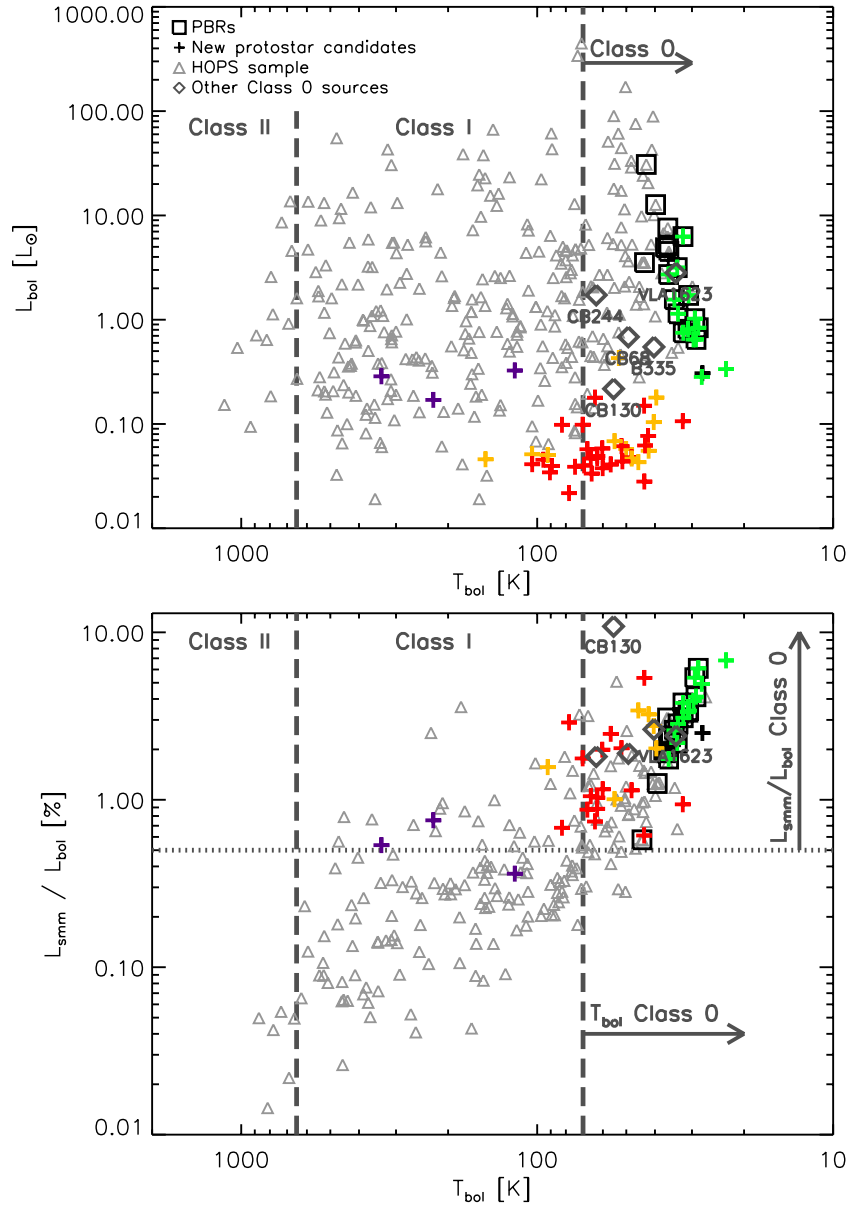
**Figure 14.** Top: bolometric luminosity vs. bolometric temperature for the new candidate protostars (+ symbols) and the HOPS protostars (light gray triangles). The color of the + symbols indicates the flag values shown in Table 3 and discussed in Section 3.2. The squares indicate the PBRs sample, drawn from both the new candidate protostar sample and the HOPS protostar sample. The dashed lines indicate the canonical $T_{\rm bol}$ divisions between protostellar classes. Bottom: $L_{\rm smm}/L_{\rm bol}$ vs. bolometric temperature for the subset of sources shown in the top panel for which we have sufficient sub-millimeter coverage to estimate $L_{\rm smm}$ (see the text). The horizontal dotted line indicates the André et al. (2000) proposed $L_{\rm smm}/L_{\rm bol} > 0.5\%$ Class 0 threshold.

(A color version of this figure is available in the online journal.)

candidate protostars are generally clustered around low $T_{\rm bol}$ values. Ignoring inclination degeneracies and other considerations, these low $T_{\rm bol}$ values indicate that the PBR sample is indeed composed of young Class 0 sources. In the right panel, we show $T_{\rm bol}$ versus $L_{\rm smm}/L_{\rm bol}$ for the sources with sufficient coverage to estimate $L_{\rm smm}$ (see Section 6.2). The PBRs, as expected if the sample can be explained as Class 0 sources, cluster around larger values of $L_{\rm smm}/L_{\rm bol}$ compared to the rest of the sample. André et al. (2000) proposed the $L_{\rm smm}/L_{\rm bol} > 0.5\%$ threshold for Class 0 sources, and all but one of the new candidate protostars for which we can estimate $L_{\rm smm}$ fall into this category. Irrespective of the evolutionary indicator that is chosen ($T_{\rm bol}$ or $L_{\rm smm}/L_{\rm bol}$), all of the new candidate protostars in both the reliable and lower probability categories

(green and yellow points, respectively), would be considered to be of Class 0 status. Finally, while the PBRs 70/24 > 1.65 color criterion causes some sources with very low values of $T_{\rm bol}$ and very high values of $L_{\rm smm}/L_{\rm bol}$ to be missed, the color selection is able to capture the vast majority of the most extreme Class 0 sources at the extrema of the $L_{\rm smm}/L_{\rm bol}$ and $T_{\rm bol}$ distributions.

This evidence strongly supports the interpretation of the PBRs (and indeed all the sources classified as reliable protostellar candidates) as very dense Class 0 protostars, irrespective of the source inclination. On the other hand, the new candidate protostar sample, taken as a whole, may be explained by a combination of the effects described above: high inclination, high densities, and extreme values of foreground extinction, along with elevated levels of extragalactic contamination. Of

particular interest is the possibility that some of the sources classified as low probability protostars at low $L_{bol}$ values may be confirmed as bona fide protostars with future observations (see Offner & McKee 2011 for a detailed discussion of the significance of such sources); this will be investigated in future work (A. M. Stutz et al., in preparation).

To definitely measure the inclinations of our sample of sources and to therefore determine envelope densities more accurately we require millimeter line emission maps at high resolution from, e.g., ALMA, along with single dish observations of high density tracers. A vigorous follow-up campaign is therefore underway to more firmly place these protostars within the context of star formation in the Orion clouds. We are observing ammonia spectra toward the full sample of protostar candidates to verify the presence of dense molecular gas and determine kinetic temperatures. A *Herschel* PACS range spectroscopy program toward eight PBRs will characterize the energetics of outflows and UV heating on small scales. The outflows (CO), dust continuum, and surrounding dense molecular gas ($N_2H^+$) are being observed in the millimeter to determine the source inclinations, outflow opening angles, inner envelope properties, and the kinematics of the larger scale dense gas.

## 8. CONCLUSIONS

We have discovered a sample of 55 new candidate protostars in Orion with *Herschel*, as part of the HOPS OTKP scan-map observations at 70 $\mu$m and 160 $\mu$m. We conclude the following.

1. The new candidate protostars are either very faint or undetected at *Spitzer* wavelengths. We find 34 sources with 24 $\mu$m magnitudes that are greater than 7.0 and 21 sources that are undetected in the MIPS 24 $\mu$m band.

2. We analyze the IRAC colors and the broad shape of the SEDs between 3.6 $\mu$m and 160 $\mu$m. Based on this analysis, we classify the sample as follows: 27% (15 sources) are considered reliable protostars, 18% (10 sources) are considered lower probability protostars, 47% (26 sources) are classified as extragalactic contamination, including AGNs, 3 sources have IRAC colors consistent with stellar photospheres but *Herschel* and APEX SEDs consistent with cold dust emission, and 1 source does not have IRAC coverage. We find that the subset of sources without 24 $\mu$m detections dominates the number of sources categorized as most reliable protostellar candidates by a factor of ∼3, suggesting that sources with no short-wavelength detections and only PACS 70 $\mu$m and longer wavelength detections are much less likely to be of extragalactic origin.

3. We combine the new protostar candidate sample with the previously identified *Spitzer* HOPS sample and find that 18 sources have 70/24 colors greater than 1.65. These are the reddest protostars known in Orion, 11 of which are newly identified *Herschel* sources in the reliable protostar category listed above. We name these sources PBRs. Compared to the other protostars in the HOPS fields, the PBRs populate the extrema in the distributions of standard evolutionary diagnostics, having both the largest $L_{smm}/L_{bol}$ ratios and lowest $T_{bol}$ values. The PBR source SEDs and peak SED wavelengths are consistent with the hypothesis that the PBRs do indeed represent a population composed of Class 0 sources with the densest envelopes in Orion.

4. A comparison to radiative transfer models of rotating, collapsing protostellar envelopes with outflow cavities

show that the 70/24 > 1.65 color limit selects sources with envelope densities with log $\rho_1/(\mathrm{g\,cm^{-3}}) \gtrsim -13.4$, irrespective of inclination effects. While the 70/24 > 1.65 color selects sources with dense envelopes, this color criterion does not find all dense sources above the threshold of $\rho_1/(\mathrm{g\,cm^{-3}}) = -13.4$. Therefore this selection should be used in conjunction with other evolutionary indicators, namely millimeter and sub-millimeter measurements, to determine the nature of the observed sources.

5. Our modeling of the PBRs' SEDs reveals that these sources are not consistent with being externally heated starless cores; the presence of a 70 $\mu$m point source requires that the sample be interpreted as dense envelopes containing embedded protostars.

6. The fraction of known protostars that are PBRs varies from 1% in the Orion A cloud to 17% in the Orion B cloud, with an average fraction over the Orion complex of 5%. These numbers suggest that if the PBRs represent a distinct phase in protostellar evolution, protostars spend on average 5% of their lifetime in the PBRs phase. Most of the PBRs in the Orion B cloud are concentrated in dense gas near the NGC 2068, NGC 2071, and NGC 2023 nebulae. These regions of dense gas are also known for a lack of more evolved pre-main-sequence stars. The high percentage of PBRs in Orion B suggests either that the regions containing the PBRs may currently be undergoing more vigorous star formation than other regions of Orion, or that the PBRs lifetime is longer in these regions.

7. The sources with 70/24 < 1.65 colors and faint 70 $\mu$m fluxes must be confirmed as either protostellar or contamination sources before their significance can be assessed. If confirmed as the former, however, this sample would constitute an important population of very low luminosity, cold protostars previously unobserved, most interesting from the point of view of constraining the faint end of the luminosity function of protostars.

8. We expect that a comparable number of very red protostars will be found with *Herschel* in more nearby star-forming regions. We caution that a careful treatment of possible extragalactic contamination must be implemented to understand the broader significance of such sources.

## APPENDIX A

## PREVIOUS PBRs DETECTIONS

We searched the SIMBAD and VizieR (Ochsenbein et al. 2000) services for previous identifications of the PBRs. We restricted our search to a radius of $20''$ from the 70 $\mu$m source coordinates. The results are summarized in Table 6. This list is likely incomplete and is intended to provide a resource and rough guide to some of the previous detections of these sources.

*061012, 119019, and 097002*. None found.

*HOPS169*. Known protostar and outflow bipolar outflow V380 Ori NE (e.g., Davis et al. 2000). Stanke et al. (2002) detected source 59 in their 2.12 $\mu$m catalog of Orion A, offset by $6''$ from our source coordinates. Davis et al. (2009) also detected an outflow about $2''$ away from our coordinates. Nutter & Ward-Thompson (2007) classified this source as hosting a YSO and measured an 850 $\mu$m flux-derived mass of 2.8 $M_\odot$ (assuming a temperature of 20 K and a distance of 400 pc).

*019003*. Since this source is located in the very crowded and complex ONC filament, it is often not clear which previous identifications may be associated with it in particular. Tsujimoto et al. (2003) listed a near-IR source located $3\!''\!.35$ away from our coordinates. Nutter & Ward-Thompson (2007) detected a source offset by $8\!''\!.4$; they classified it as hosting a YSO and measure a mass of 6.2 $M_\odot$. While it is not clear if the detection is associated with the PBRs, we consider it probable. Chini et al. (1997) and Nielbock et al. (2003) likely detected this source in their 1.3 mm maps near FIR1a in OMC-2, although their beam sizes were too large to identify the source unambiguously.

*082005*. This source was previously classified as a starless core (e.g., Johnstone & Bally 2006; Nutter & Ward-Thompson

2007; Mookerjea et al. 2009). The Nutter & Ward-Thompson (2007) location of the source is about $8''$ away from our source with an associated mass of 3.3 $M_\odot$. Mookerjea et al. (2009) measured a mass of 4.3 $M_\odot$ for this source.

*HOPS372 and 082012*. These sources have coordinates that are significantly offset from the Nutter & Ward-Thompson (2007) coordinates; the two sources are unresolved and lie about $13''$ away from their catalog entry, with a mass of 12.7 $M_\odot$. The Mookerjea et al. (2009) analysis derived a mass of 1 $M_\odot$ for 082012 (MM1) and 7.4 $M_\odot$ for HOPS372 (MM2), from modified blackbody fits to long-wavelength SEDs.

*090003*. Miettinen et al. (2009) detected this source (SMM3) in their 850 $\mu$m map, and concluded that it is a promising Class 0 candidate based on the shape of the SED. They calculated a mass of about 7.5 $M_\odot$ for this source. Miettinen et al. (2010, 2012) also observed this source in various molecular line transitions and with SABOCA at 350 $\mu$m; their measured flux for this source is $S_{350}^{\mathrm{peak}} = 3.63$ Jy beam$^{-1}$. We include their flux measurement and the 350 $\mu$m map in our analysis.

*HOPS358*. Strom et al. (1976, 1986), and (Reipurth et al. 1999) detected the Herbig–Haro complex HH24–26, with HH25 located about $10''$ away from HOPS358. This source is also included in the Wu et al. (2004) high velocity outflow catalog. Nutter & Ward-Thompson (2007) classified a nearby source ($11''$ away) as a starless core with a mass of 6.3 $M_\odot$.

*091015 and 091016*. These sources were detected by, e.g., Lis et al. (1999) at 1.3 mm and 350 $\mu$m (as sources 5 and 6). The reported masses are $\sim$2 $M_\odot$ for each source. Both sources are classified as starless by Nutter & Ward-Thompson (2007), with catalog masses of 0.8 $M_\odot$ (091015) and 1.3 $M_\odot$ (091016).

*HOPS373 and 093005*. Both sources were classified as starless by Nutter & Ward-Thompson (2007), with reported masses of 4.2 $M_\odot$ (HOPS373) and 3.9 $M_\odot$ (093005). Motte et al. (2001) observed this region at 450 and 850 $\mu$m and also classified 093005 as a starless core, based on the lack of evidence for an embedded source. Source HOPS373, on the other hand, is known to be driving a CO outflow (Gibb & Little 2000), and therefore has been classified as a candidate Class 0 source. Furthermore, Haschick et al. (1983) identified a water maser near the HOPS373 location.

*302002*. Nutter & Ward-Thompson (2007) reported a mass of 2.7 $M_\odot$ and classified this source as protostellar. Phillips et al. (2001) classify this source (LBS18S) as pre-protostellar, however.

*HOPS359*. Nutter & Ward-Thompson (2007) classified this source as protostellar and measure a mass of 2.7 $M_\odot$.

*HOPS341*. This source is strongly blended with HOPS340. We have listed some detections of the combined system in Table 6.

*HOPS354*. Reipurth et al. (2008) described this source in the context of the L1622 cloud. Bally et al. (2009) also detected this source in their analysis of *Spitzer* IRAC images but did not analyze it in detail.

## APPENDIX B

## GALLERY OF IMAGES OF PACS BRIGHT RED SOURCES

Here we present the gallery of images of the remaining PBRs, shown in Figures 15–25.
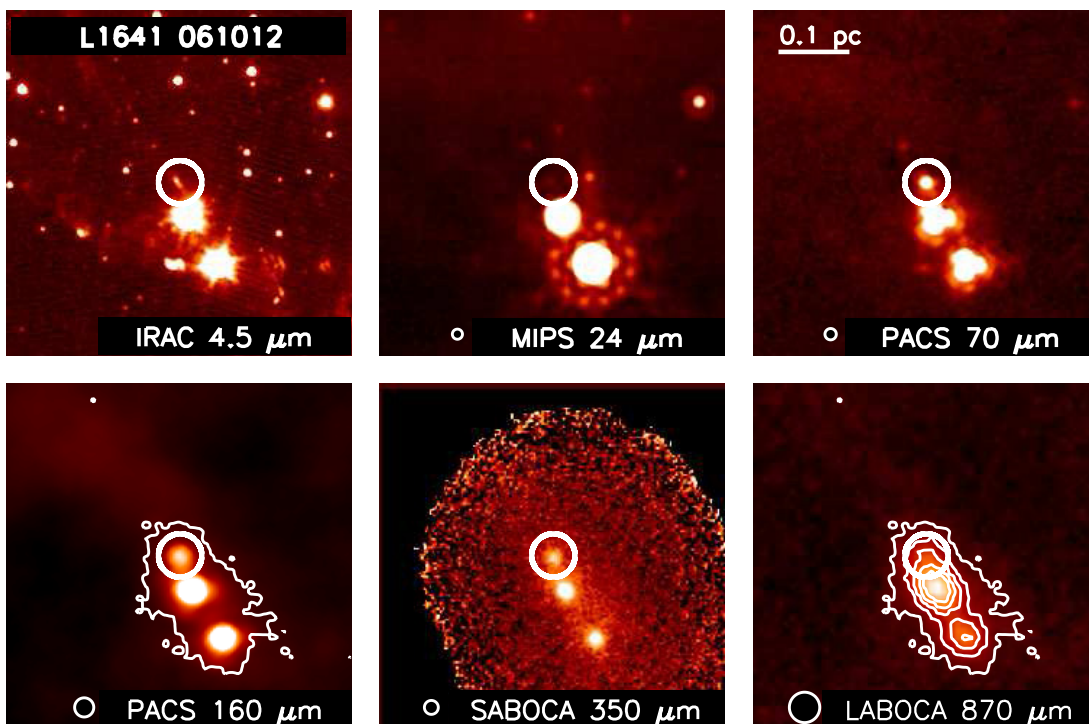
**Figure 15.** Same as Figure 7, showing $4' \times 4'$ images of PBR 061012. The IRAC-band emission associated with the source is clearly visible at 4.5 $\mu$m. Contours indicate the 870 $\mu$m emission levels at $\{0.1, 0.25, 0.4, 0.55, 0.7\}$ Jy beam$^{-1}$; the long wavelength sub-millimeter data trace the cold envelope material associated with the source. The 160 $\mu$m panel is shown with the lowest 870 $\mu$m emission contour.

(A color version of this figure is available in the online journal.)
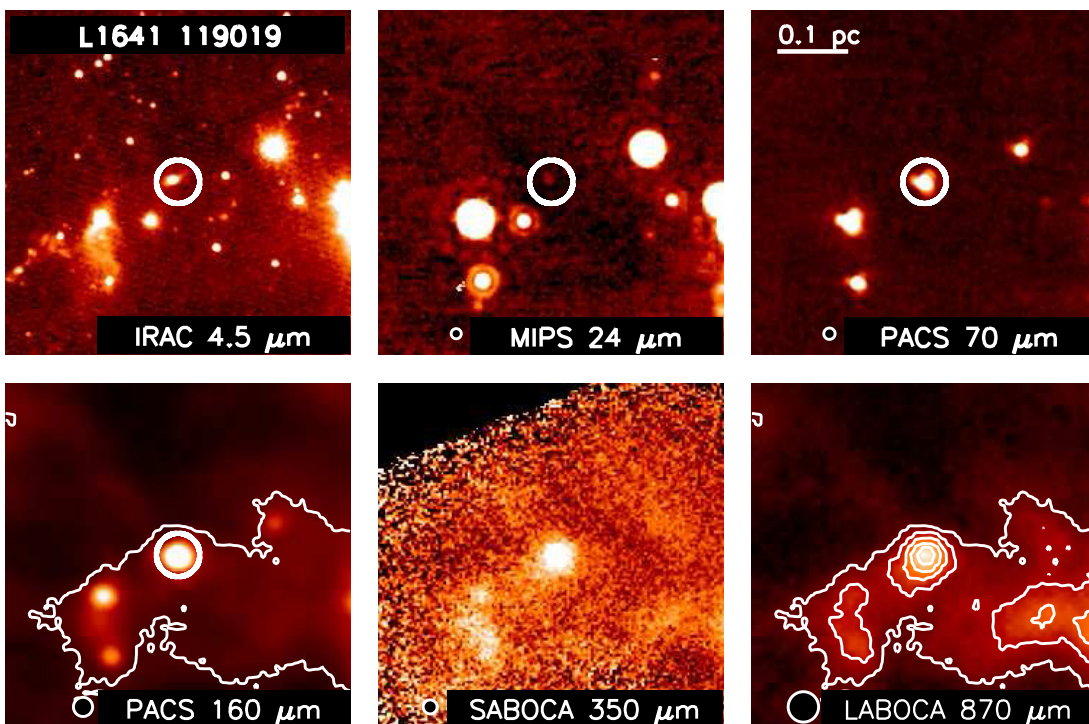


**Figure 16.** Same as Figure 7, showing $4' \times 4'$ images and SED of PBR 119019. Contours indicate the 870 $\mu$m emission levels at $\{0.1, 0.2, 0.3, 0.4, 0.5\}$ Jy beam$^{-1}$. This source has prominent IRAC emission and is located in an IRAC 8 $\mu$m and MIPS 24 $\mu$m shadow.

(A color version of this figure is available in the online journal.)

26
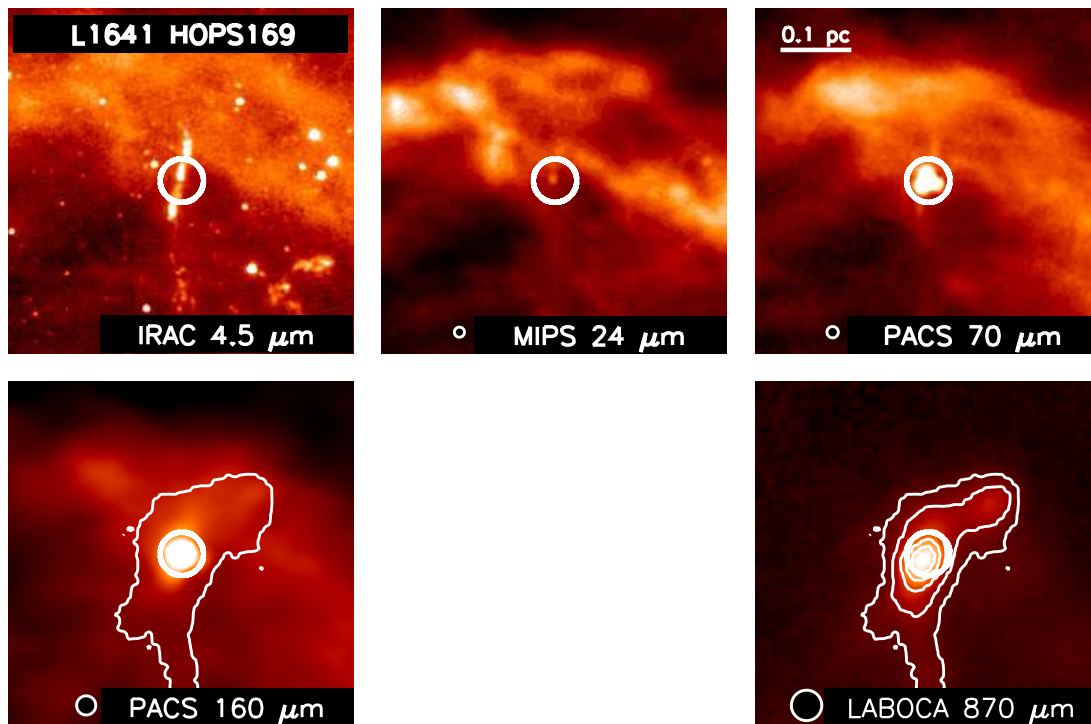
**Figure 17.** Same as Figure 7, showing $4' \times 4'$ images and SED of HOPS169. Contours indicate the 870 $\mu$m emission levels at {0.1, 0.2, 0.4, 0.6, 0.8} Jy beam$^{-1}$. This source has clear outflow activity, traced by the IRAC emission, and appears to be at high inclination.

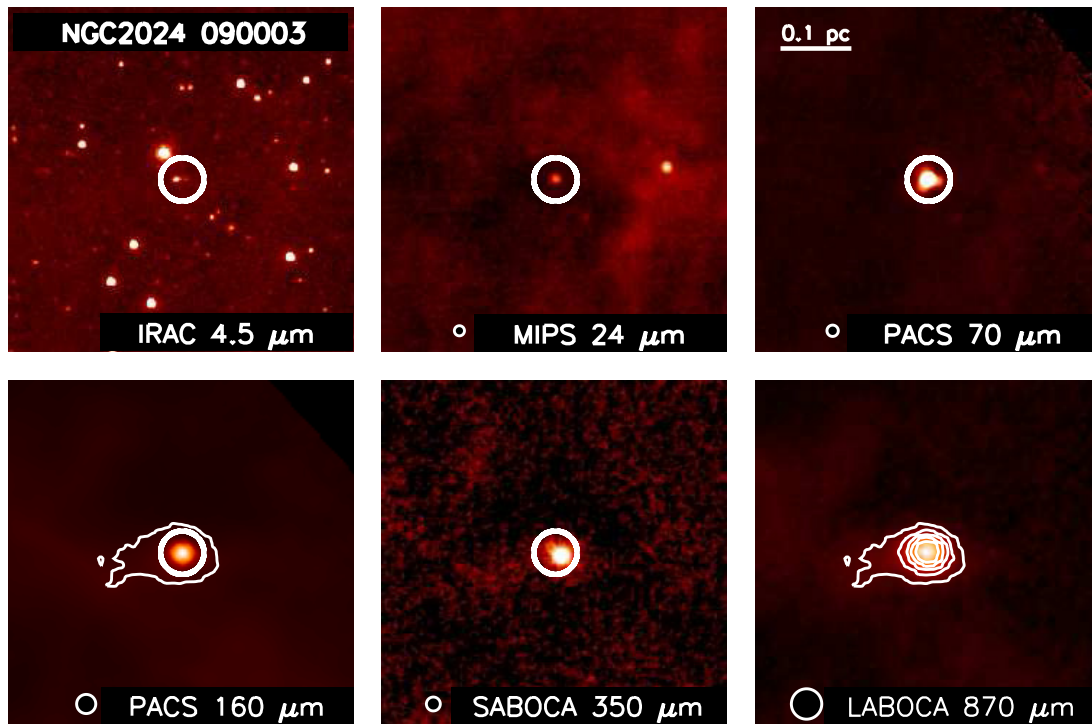(A color version of this figure is available in the online journal.)
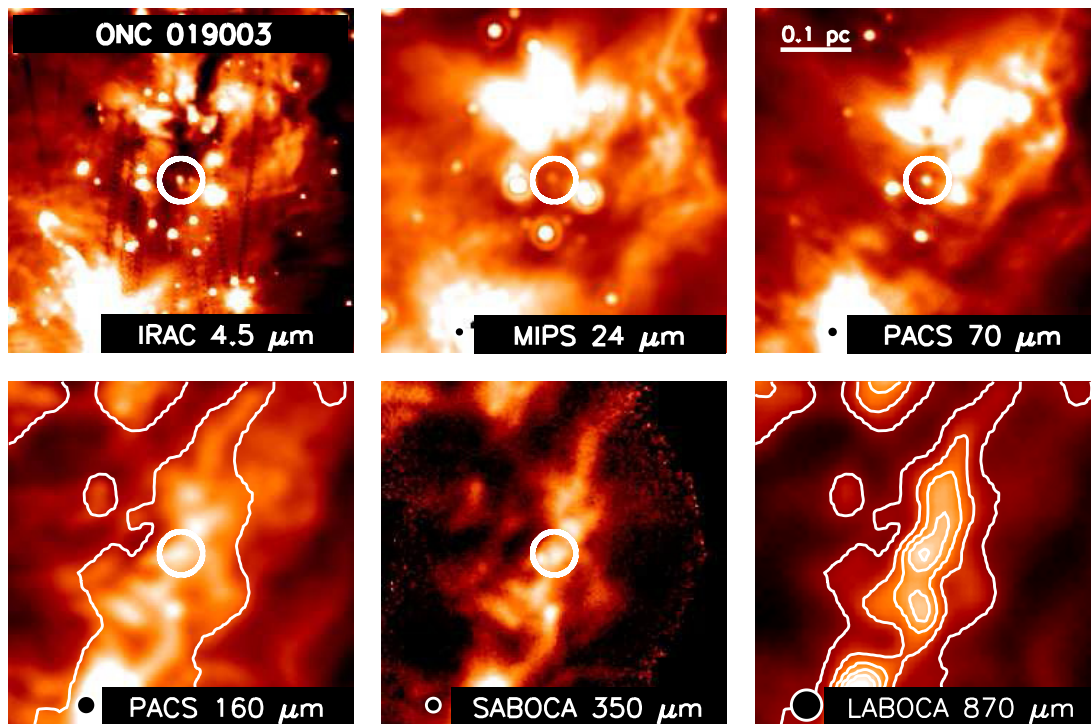


**Figure 18.** Same as Figure 7, showing $4' \times 4'$ images and SED of PBR source 019003. Contours indicate the 870 $\mu$m emission levels at {0.5, 1.0, 1.5, 2.0, 2.5} Jy beam$^{-1}$. This source has indications of outflow activity, as traced by the IRAC emission. The *Herschel* photometry may be strongly affected by blending due to the source location in a very dense filament.

(A color version of this figure is available in the online journal.)
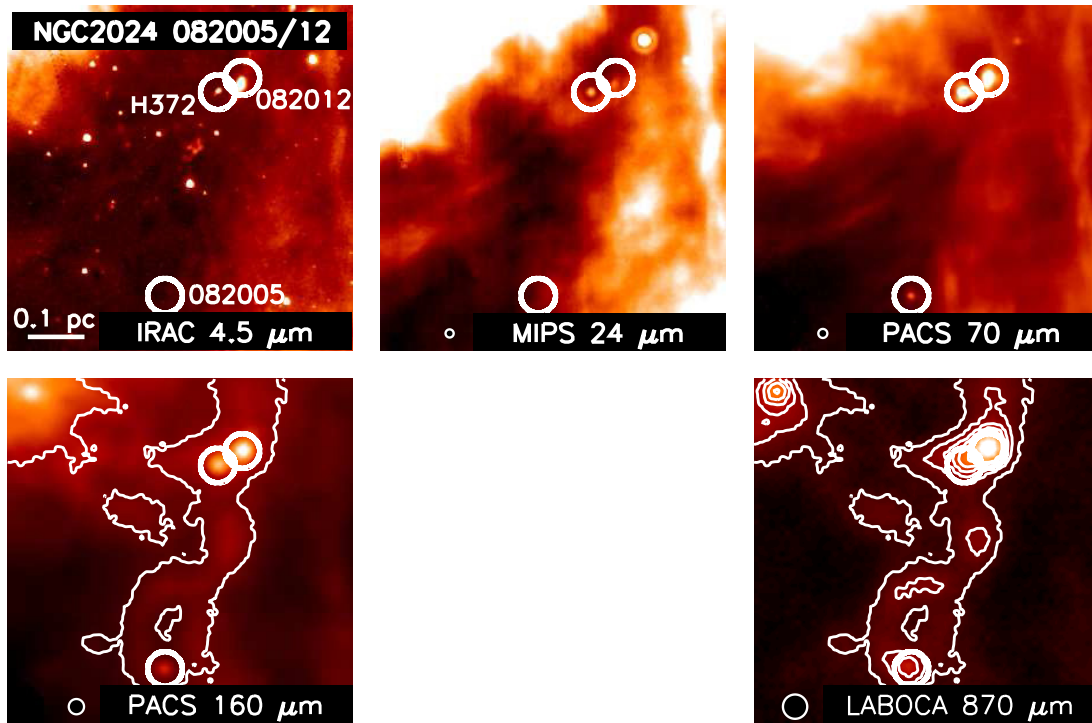
**Figure 19.** Top: same as Figure 7, showing $5' \times 5'$ images of three red sources: HOPS372 and 082012 (top) and 082005 (bottom). Contours indicate the 870 $\mu$m emission levels at $\{0.25, 0.5, 0.75, 1.0, 1.25, 1.5\}$ Jy beam$^{-1}$. No IRAC emission is detected for 082005; however, this source is located in dense filamentary material traced by the sub-millimeter emission and an 8 $\mu$m absorption feature.

(A color version of this figure is available in the online journal.)



**Figure 20.** Same as Figure 7, showing $4' \times 4'$ images and SED of PBR 090003. Contours indicate the 870 $\mu$m emission levels at $\{0.25, 0.5, 0.75, 1.0, 1.25, 1.5\}$ Jy beam$^{-1}$. The IRAC data show faint indications of extended emission, possibly associated with an outflow activity or a second source. The 350 $\mu$m image and SED point are from Miettinen et al. (2012).

(A color version of this figure is available in the online journal.)
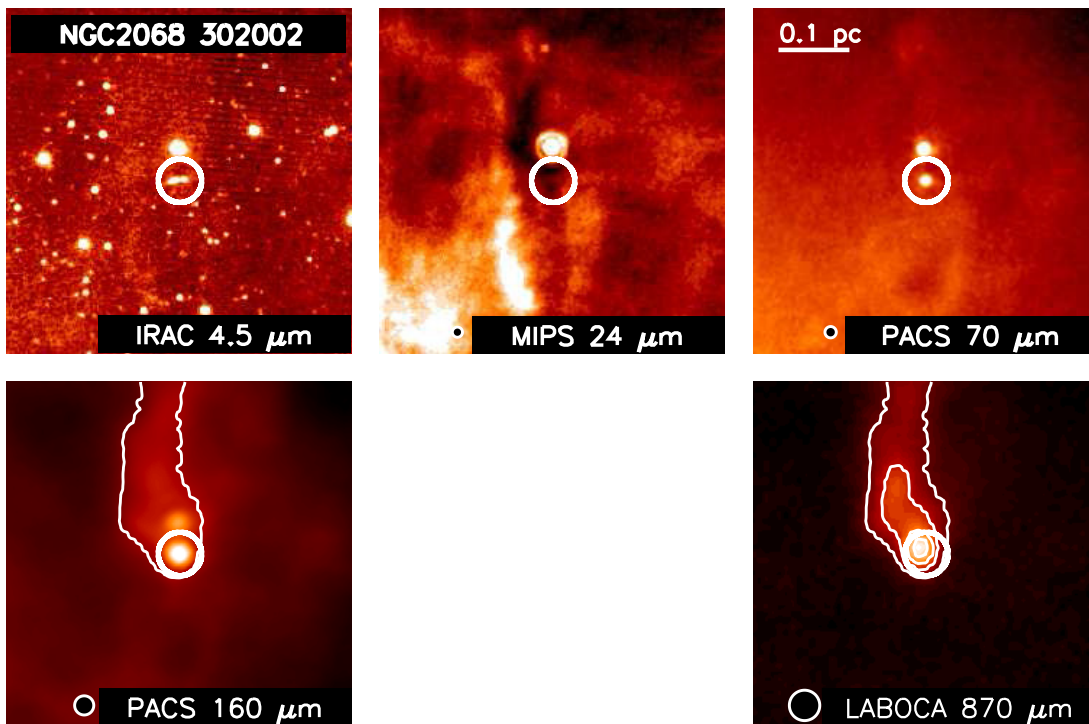
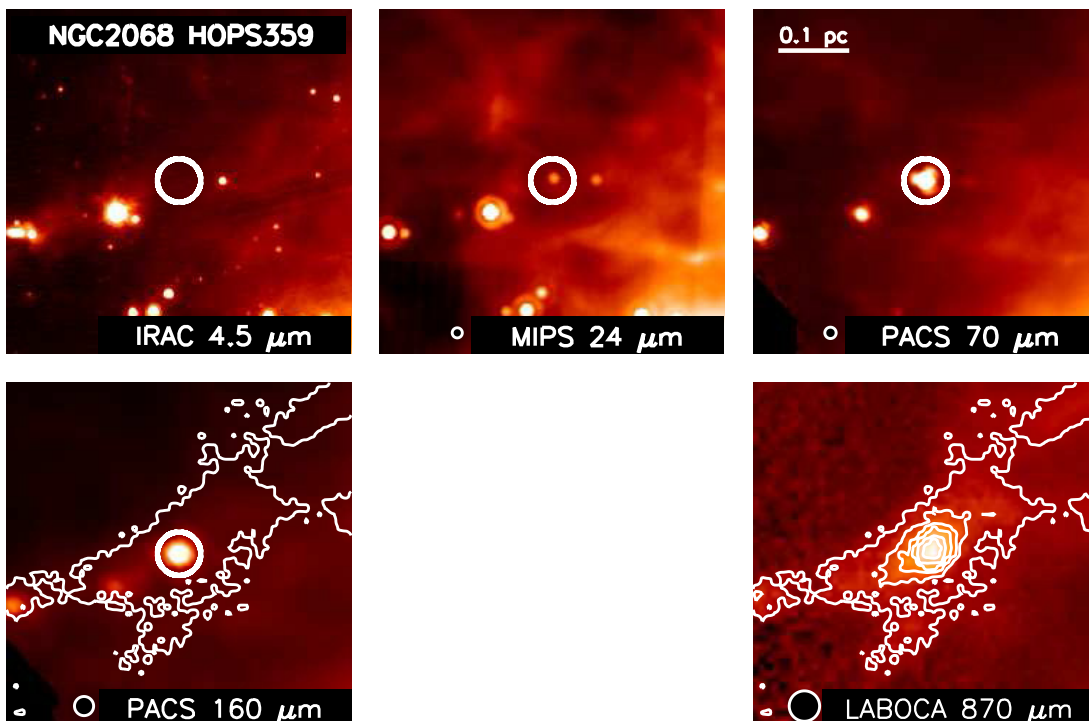**Figure 21.** Same as Figure 7; $4' \times 4'$ images of PBR 302002. Contours indicate the 870 $\mu$m emission levels at {0.25, 0.5, 0.75, 1.0, 1.25, 1.5} Jy beam$^{-1}$, tracing the cometary-globule-shaped region. The IRAC data show indications of emission associated with outflow activity; furthermore, the 4.5 $\mu$m data show evidence that this source is observed at high inclination. This source is the second most massive source in our sample, with a best-fit $M_{env} = 1.7\ M_\odot$.

(A color version of this figure is available in the online journal.)



**Figure 22.** Same as Figure 7; $4' \times 4'$ images of HOPS359. Contours indicate the 870 $\mu$m emission levels at {0.25, 0.5, 0.75, 1.0, 1.25, 1.5} Jy beam$^{-1}$.
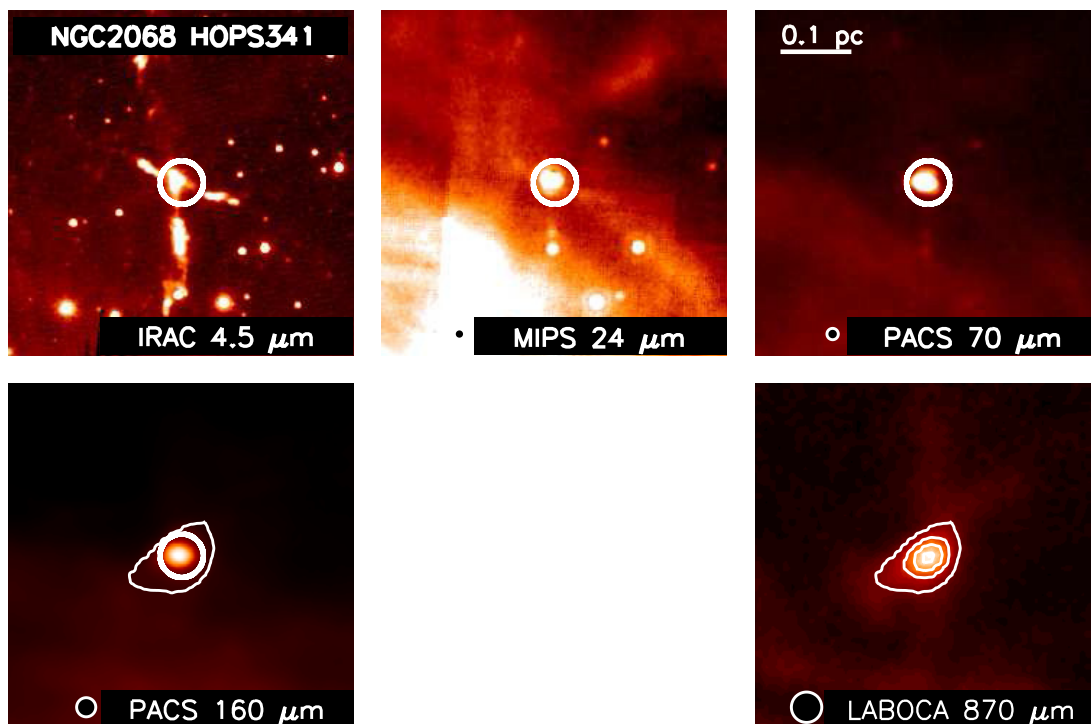(A color version of this figure is available in the online journal.)

**Figure 23.** Same as Figure 7; $4' \times 4'$ images of HOPS341. Contours indicate the 870 $\mu$m emission levels at $\{0.25, 0.5, 0.75, 1.0\}$ Jy beam$^{-1}$. The $\times$-shaped morphology of this source in the IRAC bands indicated that it is a binary. Indeed, the photometry of this source is strongly blended with HOPS340; nevertheless, we include this source in our sample for completeness.

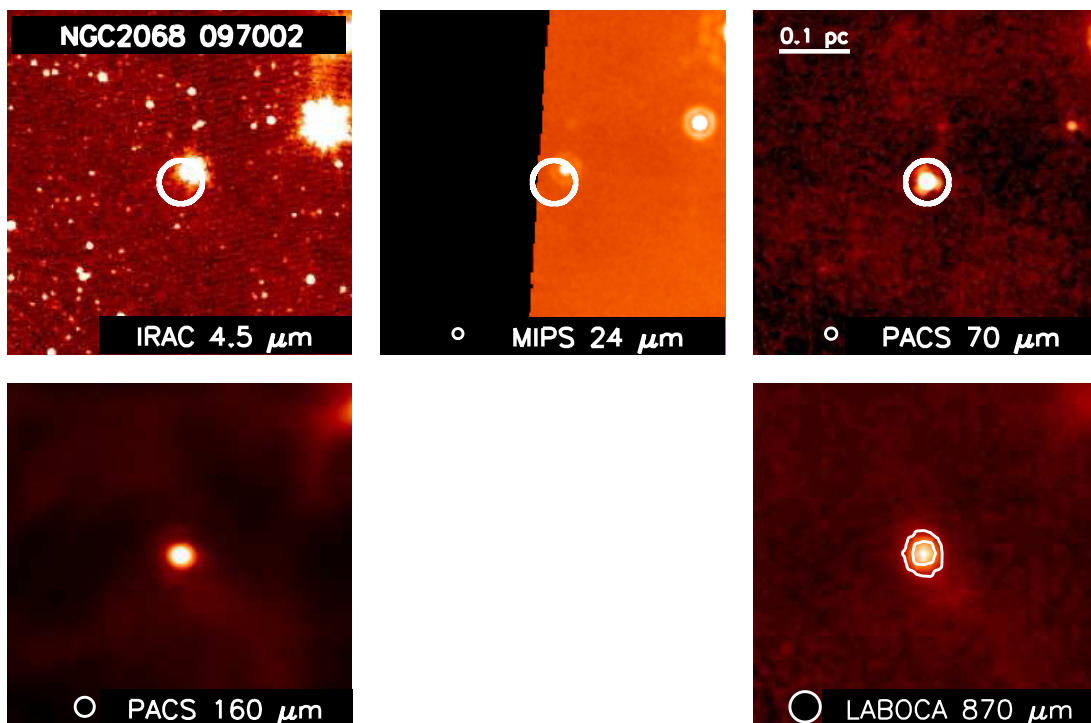(A color version of this figure is available in the online journal.)



**Figure 24.** Same as Figure 7; $4' \times 4'$ images of PBR 097002. Contours indicate the 870 $\mu$m emission levels at $\{0.25, 0.5\}$ Jy beam$^{-1}$.

(A color version of this figure is available in the online journal.)

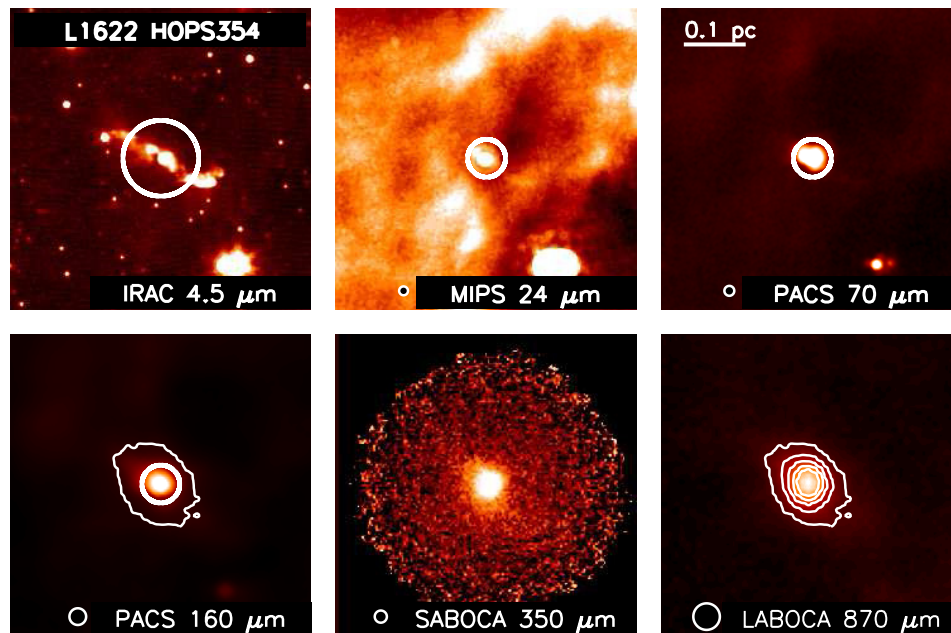**Figure 25.** Same as Figure 7; $4' \times 4'$ images of HOPS354. Contours indicate the 870 $\mu$m emission levels at {0.25, 0.5, 0.75, 1.0, 1.25} Jy beam$^{-1}$. The IRAC images display clear indications of outflow activity; furthermore, the source appears highly inclined.

(A color version of this figure is available in the online journal.)

## REFERENCES

Ali, B., Tobin, J. J., Fischer, W. J., et al. 2010, A&A, 518, L119
Allen, L. E., Calvet, N., D'Alessio, P., et al. 2004, ApJS, 154, 363
André, P., Men'shchikov, A., Bontemps, S., et al. 2010, A&A, 518, L102
André, P., Ward-Thompson, D., & Barsony, M. 1993, ApJ, 406, 122
André, P., Ward-Thompson, D., & Barsony, M. 2000, in Protostars and Planets IV, ed. V. Mannings, A. P. Boss, & S. S. Russell (Tucson, AZ: Univ. Arizona Press), 59
Aniano, G., Draine, B. T., Gordon, K. D., & Sandstrom, K. 2011, PASP, 123, 1218
Arce, H. G., & Sargent, A. I. 2006, ApJ, 646, 1070
Bally, J., Walawender, J., Reipurth, B., & Megeath, S. T. 2009, AJ, 137, 3843
Bourke, T. L., Myers, P. C., Evans, N. J., II, et al. 2006, ApJL, 649, L37
Cassen, P., & Moosman, A. 1981, Icar, 48, 353
Chen, X., Arce, H. G., Zhang, Q., et al. 2010, ApJ, 715, 1344
Chini, R., Reipurth, B., Ward-Thompson, D., et al. 1997, ApJL, 474, L135
Commerçon, B., Launhardt, R., Dullemond, C., & Henning, T. 2012, A&A, 545, A98
Da Rio, N., Robberto, M., Hillenbrand, L. A., Henning, T., & Stassun, K. G. 2012, ApJ, 748, 14
Davis, C. J., Dent, W. R. F., Matthews, H. E., Coulson, I. M., & McCaughrean, M. J. 2000, MNRAS, 318, 952
Davis, C. J., Froebrich, D., Stanke, T., et al. 2009, A&A, 496, 153
De Buizer, J. M., Osorio, M., & Calvet, N. 2005, ApJ, 635, 452
Di Francesco, J., Johnstone, D., Kirk, H., MacKenzie, T., & Ledwosinska, E. 2008, ApJS, 175, 277
Draine, B. T., & Lee, H. M. 1984, ApJ, 285, 89
Dunham, M. M., Crapsi, A., Evans, N. J., II, et al. 2008, ApJS, 179, 249
Dunham, M. M., Evans, N. J., II, Bourke, T. L., et al. 2006, ApJ, 651, 945
Dunham, M. M., Evans, N. J., II, Terebey, S., Dullemond, C. P., & Young, C. H. 2010, ApJ, 710, 470
Enoch, M. L., Evans, N. J., II, Sargent, A. I., & Glenn, J. 2009, ApJ, 692, 973
Enoch, M. L., Lee, J.-E., Harvey, P., Dunham, M. M., & Schnee, S. 2010, ApJL, 722, L33
Evans, N. J., II, Dunham, M. M., Jørgensen, J. K., et al. 2009, ApJS, 181, 321
Fang, M., van Boekel, R., Wang, W., et al. 2009, A&A, 504, 461
Fischer, W. J., Megeath, S. T., Ali, B., et al. 2010, A&A, 518, L122
Fischer, W. J., Megeath, S. T., Tobin, J. J., et al. 2012, ApJ, 756, 99
Flaherty, K. M., & Muzerolle, J. 2008, AJ, 135, 966
Flaherty, K. M., Pipher, J. L., Megeath, S. T., et al. 2007, ApJ, 663, 1069
Furlan, E., McClure, M., Calvet, N., et al. 2008, ApJS, 176, 184
Gibb, A. G., & Little, L. T. 2000, MNRAS, 313, 663
Gordon, K. D., Rieke, G. H., Engelbracht, C. W., et al. 2005, PASP, 117, 503
Gutermuth, R. A., Megeath, S. T., Myers, P. C., et al. 2009, ApJS, 184, 18

Gutermuth, R. A., Myers, P. C., Megeath, S. T., et al. 2008, ApJ, 674, 336
Hartmann, L. 2009, Accretion Processes in Star Formation (2nd ed.; Cambridge: Cambridge Univ. Press)
Harvey, P., Merín, B., Huard, T. L., et al. 2007, ApJ, 663, 1149
Haschick, A. D., Moran, J. M., Rodriguez, L. F., & Ho, P. T. P. 1983, ApJ, 265, 281
Hatchell, J., Fuller, G. A., Richer, J. S., Harries, T. J., & Ladd, E. F. 2007, A&A, 468, 1009
Hirota, T., Bushimata, T., Choi, Y. K., et al. 2007, PASJ, 59, 897
Hsu, W.-H., Hartmann, L., Allen, L., et al. 2012, ApJ, 752, 59
Johnston, K. G., Shepherd, D. S., Robitaille, T. P., & Wood, K. 2012, A&A, 551, A43
Johnstone, D., & Bally, J. 2006, ApJ, 653, 383
Johnstone, D., Fich, M., Mitchell, G. F., & Moriarty-Schieven, G. 2001, ApJ, 559, 307
Jørgensen, J. K., Johnstone, D., Kirk, H., & Myers, P. C. 2007, ApJ, 656, 293
Jørgensen, J. K., van Dishoeck, E. F., Visser, R., et al. 2009, A&A, 507, 861
Kenyon, S. J., & Hartmann, L. W. 1990, ApJ, 349, 197
Kenyon, S. J., Whitney, B. A., Gomez, M., & Hartmann, L. 1993, ApJ, 414, 773
Kim, S.-H., Martin, P. G., & Hendry, P. D. 1994, ApJ, 422, 164
Könyves, V., André, P., Men'shchikov, A., et al. 2010, A&A, 518, L106
Kryukova, E., Megeath, S. T., Gutermuth, R. A., et al. 2012, AJ, 144, 31
Lada, C. J. 1987, in IAU Symp. 115, Star Forming Regions, ed. M. Peimbert & J. Jugaku (Cambridge: Cambridge Univ. Press), 1
Lada, E. A. 1992, ApJL, 393, L25
Lada, E. A., Bally, J., & Stark, A. A. 1991a, ApJ, 368, 432
Lada, E. A., Depoy, D. L., Evans, N. J., II, & Gatley, I. 1991b, ApJ, 368, 432
Lada, E. A., Evans, N. J., II, & Falgarone, E. 1997, ApJ, 488, 286
Larson, R. B. 1969, MNRAS, 145, 271
Launhardt, R., Mezger, P. G., Haslam, C. G. T., et al. 1996, A&A, 312, 569
Launhardt, R., Nutter, D., Ward-Thompson, D., et al. 2010, ApJS, 188, 139
Launhardt, R., Stutz, A., Schmiedeke, A., et al. 2013, A&A, in press
Levreault, R. M. 1988, ApJS, 67, 283
Lis, D. C., Menten, K. M., & Zylka, R. 1999, ApJ, 527, 856
Manoj, P., Watson, D. M., Neufeld, D. A., et al. 2013, ApJ, 763, 83
Mathis, J. S., Mezger, P. G., & Panagia, N. 1983, A&A, 128, 212
Megeath, S. T., Allen, L. E., Gutermuth, R. A., et al. 2004, ApJS, 154, 367
Megeath, S. T., et al. 2012, ApJ, in press
Men'shchikov, A., André, P., Didelon, P., et al. 2010, A&A, 518, L103
Menten, K. M., Reid, M. J., Forbrich, J., & Brunthaler, A. 2007, A&A, 474, 515
Mezger, P. G., Zylka, R., & Wink, J. E. 1990, A&A, 228, 95
Miettinen, O., Harju, J., Haikala, L. K., & Juvela, M. 2010, A&A, 524, A91
Miettinen, O., Harju, J., Haikala, L. K., & Juvela, M. 2012, A&A, 538, A137
Miettinen, O., Harju, J., Haikala, L. K., Kainulainen, J., & Johansson, L. E. B. 2009, A&A, 500, 845

Mitchell, G. F., Johnstone, D., Moriarty-Schieven, G., Fich, M., & Tothill, N. F. H. 2001, ApJ, 556, 215
Mookerjea, B., Sandell, G., Jarrett, T. H., & McMullin, J. P. 2009, A&A, 507, 1485
Morgan, J. A., Schloerb, F. P., Snell, R. L., & Bally, J. 1991, ApJ, 376, 618
Motte, F., André, P., Ward-Thompson, D., & Bontemps, S. 2001, A&A, 372, L41
Myers, P. C., Adams, F. C., Chen, H., & Schaff, E. 1998, ApJ, 492, 703
Myers, P. C., & Ladd, E. F. 1993, ApJL, 413, L47
Nielbock, M., Chini, R., & Müller, S. A. H. 2003, A&A, 408, 245
Nielbock, M., Launhardt, R., Steinacker, J., et al. 2012, A&A, 547, A11
Noriega-Crespo, A., Moro-Martin, A., Carey, S., et al. 2004, ApJS, 154, 402
Nutter, D., & Ward-Thompson, D. 2007, MNRAS, 374, 1413
Ochsenbein, F., Bauer, P., & Marcout, J. 2000, A&AS, 143, 23
Offner, S. S. R., & McKee, C. F. 2011, ApJ, 736, 53
Offner, S. S. R., Robitaille, T. P., Hansen, C. E., McKee, C. F., & Klein, R. I. 2012, ApJ, 753, 98
Ormel, C. W., Min, M., Tielens, A. G. G. M., Dominik, C., & Paszun, D. 2011, A&A, 532, A43
Ossenkopf, V., & Henning, T. 1994, A&A, 291, 943
Padgett, D. L., Brandner, W., Stapelfeldt, K. R., et al. 1999, AJ, 117, 1490
Pezzuto, S., Elia, D., Schisano, E., et al. 2012, A&A, 547, A54
Phillips, R. R., Gibb, A. G., & Little, L. T. 2001, MNRAS, 326, 927
Pilbratt, G. L., Riedinger, J. R., Passvogel, T., et al. 2010, A&A, 518, L1
Pineda, J. E., Arce, H. G., Schnee, S., et al. 2011, ApJ, 743, 201
Poglitsch, A., Waelkens, C., Geis, N., et al. 2010, A&A, 518, L2
Porter, T. A., & Strong, A. W. 2005, in Proc. 29th ICRC (Pune), 4, 77
Press, W. H., Teukolsky, S. A., Vetterling, W. T., & Flanney, B. P. 1992, Numerical Recipes in FORTRAN (Cambridge: Cambridge Univ. Press)
Price, D. J., Tricco, T. S., & Bate, M. R. 2012, MNRAS, 423, L45
Ragan, S., Henning, T., Krause, O., et al. 2012, A&A, 547, A49
Reggiani, M., Robberto, M., Da Rio, N., et al. 2011, A&A, 534, A83
Reipurth, B., Megeath, S. T., Bally, J., & Walawender, J. 2008, in Handbook of Star Forming Regions, Vol. I: The Northern Sky, ed. B. Reipurth (ASP Monograph Publications, Vol. 4; San Francisco, CA: ASP), 782

Reipurth, B., Rodríguez, L. F., & Chini, R. 1999, AJ, 118, 983
Robitaille, T. P. 2011, A&A, 536, A79
Robitaille, T. P., Meade, M. R., Babler, B. L., et al. 2008, AJ, 136, 2413
Roussel, H. 2012, PASP, submitted (arXiv:1205.2576)
Sadavoy, S. I., Di Francesco, J., Bontemps, S., et al. 2010, ApJ, 710, 1247
Sandstrom, K. M., Peek, J. E. G., Bower, G. C., Bolatto, A. D., & Plambeck, R. L. 2007, ApJ, 667, 1161
Savva, D., Little, L. T., Phillips, R. R., & Gibb, A. G. 2003, MNRAS, 343, 259
Siringo, G., Kreysa, E., De Breuck, C., et al. 2010, Msngr, 139, 20
Siringo, G., Kreysa, E., Kovács, A., et al. 2009, A&A, 497, 945
Sodroski, T. J., Odegard, N., Arendt, R. G., et al. 1997, ApJ, 480, 173
Stanke, T., McCaughrean, M. J., & Zinnecker, H. 2002, A&A, 392, 239
Stanke, T., Stutz, A. M., Tobin, J. J., et al. 2010, A&A, 518, L94
Stern, D., Eisenhardt, P., Gorjian, V., et al. 2005, ApJ, 631, 163
Strom, K. M., Strom, S. E., & Vrba, F. J. 1976, AJ, 81, 308
Strom, K. M., Strom, S. E., Wolff, S. C., Morgan, J., & Wenz, M. 1986, ApJS, 62, 39
Stutz, A., Launhardt, R., Linz, H., et al. 2010, A&A, 518, L87
Stutz, A. M., Rubin, M., Werner, M. W., et al. 2008, ApJ, 687, 389
Terebey, S., Shu, F. H., & Cassen, P. 1984, ApJ, 286, 529
Tobin, J. J., Hartmann, L., Chiang, H.-F., et al. 2012, Natur, 492, 83
Tobin, J. J., Looney, L. W., Mundy, L. G., Kwon, W., & Hamidouche, M. 2007, ApJ, 659, 1404
Tsujimoto, M., Koyama, K., Kobayashi, N., et al. 2003, AJ, 125, 1537
Ulrich, R. K. 1976, ApJ, 210, 377
Whitney, B. A., Wood, K., Bjorkman, J. E., & Cohen, M. 2003a, ApJ, 598, 1079
Whitney, B. A., Wood, K., Bjorkman, J. E., & Wolff, M. J. 2003b, ApJ, 591, 1049
Williams, J. P., & Cieza, L. A. 2011, ARA&A, 49, 67
Winston, E., Megeath, S. T., Wolk, S. J., et al. 2007, ApJ, 669, 493
Wu, Y., Wei, Y., Zhao, M., et al. 2004, A&A, 426, 503
Young, C. H., & Evans, N. J., II. 2005, ApJ, 627, 293
Zavagno, A., Molinari, S., Tommasi, E., Saraceno, P., & Griffin, M. 1997, A&A, 325, 685